Electrochemical Performance and Compatibility of $La_2NiO_{4+\delta}$ Electrode Material with $La_{0.8}Sr_{0.2}Ga_{0.8}Mg_{0.2}O_{3-\delta}$ Electrolyte for Solid Oxide Electrolysis

Lydia Fawcett

Imperial College London, Department of Materials

Submitted for examination for the degree of Doctor of Philosophy

I declare that any work presented in this thesis which is not my own has been clearly referenced.

Lydia Fawcett

Abstract

$La_{0.8}Sr_{0.2}Ga_{0.8}Mg_{0.2}O_{3-\delta}$ (LSGM) is an oxygen ion conducting electrolyte material widely used in solid oxide fuel cells (SOFC). $La_2NiO_{4+\delta}$ (LNO) is a mixed ionic-electronic conducting layered perovskite with K_2NiF_4 type structure which conducts oxygen ions via oxygen interstitials. LNO has shown promising results as an SOFC electrode in the literature. In this work the compatibility and performance of LNO electrodes on the LSGM electrolyte material for solid oxide electrolysis cell (SOEC) is investigated.

The materials were characterised as SOEC/SOFC cells by symmetrical and three electrode electrochemical measurements using Electrochemical Impedance Spectroscopy (EIS). Conductivity and ASR values were obtained in the temperature range 300 – 800^{o}C with varying atmospheres of pH_2O and pO_2. The cells were also subjected to varied potential bias, mimicking fuel cell or electrolysis use. Enhancement of LNO performance was observed with the application of potential bias in both anodic and cathodic mode of operation in all atmospheres with the exception of cathodic bias in pO_2 = 6.5x10^{-3} atm. In ambient air at 800^{o}C LNO ASRs were 2.82Ω.cm^2, 1.83Ω.cm^2 and 1.37Ω.cm^2 in OCV, +1000mV bias and -1000mV bias respectively. In low pO_2 at 800^{o}C LNO ASRs were 9.17Ω.cm^2, 1.74Ω.cm^2 and 456.9Ω.cm^2 in OCV, +1000mV bias and -1000mV bias respectively. The increase in ASR with negative potential bias in low pO_2 is believed to be caused by an increase in mass transport and charge transfer impedance responses.

Material stability was confirmed using X-Ray Diffraction (XRD), in-situ high temperature pH_2O and pO_2 XRD. In-situ XRD displayed single phase materials with no observable reactivity in the conditions tested. Scanning Electron Microscopy images of cells tested by EIS in all atmospheres displayed no microstructure degradation except for those cells tested in a humid atmosphere which display a regular pattern of degradation on the LNO surface attributed to reaction with the Pt mesh current collector.

Acknowledgements

Firstly I would like to thank my supervisor Stephen Skinner for all his guidance, support and understanding throughout my PhD. I would also like to thank my secondary supervisor John Kilner for his encouragement and advice.

There are a number of people who kindly imparted knowledge and technical help who deserve many thanks, namely Richard Sweeny and Ryan Bayliss for their help with XRD at Imperial College and Rose Noelle Vannier for the in-situ atmospheric XRD; Jing Jing Liu, Ning Xu and Miguel Laguna-Bereco for impedance knowledge; Florent Tonus for XRD fitting advice; Mahmoud Ardankani for his training on the SEM and Ainara Aguadero for analysis advice and overall friendship.

My time at Imperial College has been extremely positive, not least because of the incredibly friendly members of the Materials Department Fuel Cells Group and the greater network of the Materials Department. I would therefore like to thank everyone in the department who has made life inside and outside of the lab even more enjoyable.

Away from university life I owe a great deal to those friends and family who have offered immeasurable support just by being themselves, in particular my parents, Edd and of course Jessica, who always was a little too proud of me, in the way only a big sister can be. This is for her.

Contents

List of Figures

List of Tables

Chapter 1 – Introduction and Background

In this chapter the context of this work is presented. The current and predicted role of fuel cell technologies is discussed in regard to climate change and energy policy. In this chapter it is determined that methods of producing fuel for fuel cells without emitting greenhouse gasses are required and a selection of possible methods are listed and briefly discussed. As this thesis will focus on the performance of a novel solid oxide electrolysis cell (SOEC), SOEC technology is presented in this chapter. Thermodynamic considerations are discussed and efficiency and common factors that reduce efficiency in SOECs are given. An overview of material requirements for SOECs is presented.

1.1 Energy Demand and Climate Change

Due to national and global population growth it is recognised that alternate forms of energy generation are required to support and eventually replace the burning of fossil fuels. Reliance on fossil fuels is politically unstable, environmentally damaging and ultimately finite. In order to drastically lessen our dependence on oil, gas and coal it is recognised that a wide and varied portfolio of green technologies must be developed. For this reason a wide range of sustainable energy technologies are entering the market or receiving research funding. In 2011 the UK coalition government pledged to halve greenhouse gas emissions compared to 1990 levels by the mid-2020s. In order to achieve this goal The Carbon Plan [1] states that at the beginning of the 2020's carbon saving or sequestering technologies, that are currently being demonstrated or deployed on a small scale, must become mass deployed. It is predicted that a move towards electric and hydrogen fuel cell vehicles will reduce road transport emissions by the required 50% or more. [1]

1.2 Fuel Cells

A fuel cell converts chemical energy from a fuel into electricity via a reaction with oxygen. If the fuel is hydrogen then the products are water and heat with no carbon emissions. Hydrocarbons such as natural gas or methanol can also be used as fuel, making fuel cells a good bridging technology until a hydrogen economy is adopted. An overview of hydrogen production methods is presented below.

There are a number of different types of fuel cell design dependent on electrolyte characteristics and power output requirements. Further discussion of the types of fuel cell, their operation and subsequent merits and disadvantages can be found in the following references: [2-4].

1.3 Hydrogen Production Methods

Hydrogen is the most abundant element in the universe, but on Earth it can only be found bonded in molecules. Hydrogen must be produced from hydrogen containing substances such as conventional fossil fuels, alcohols or water before it can be utilised in technologies such as fuel cells. Hydrogen is therefore known as an energy carrier, or energy vector. A range of techniques are available to convert fuel to hydrogen, some of the more developed methods are discussed below followed by a more detailed description of solid oxide electrolysis cells (SOEC).

The most common methods for producing hydrogen use hydrocarbon fuel such as natural gas and liquefied petroleum gas. These methods are widely adopted for economic reasons but produce greenhouse emissions such as CO_2, NO_x and SO_x.

1.3.1 Hydrocarbons

Steam Reforming

Steam reforming is the industry favoured method for producing hydrogen with efficiencies of 83% reported [5]; about 95% of all hydrogen produced in the USA for industrial use is done so by steam reformation of natural gas. [6] In this process steam at temperatures of 700°C – 1000°C reacts with a hydrocarbon in the presence of a catalyst and under pressures of 3 – 25 bar to form hydrogen and carbon monoxide as shown in Equation 1:

$C_mH_n + mH_2O \rightarrow mCO + (m + ½\ n)H_2$ Equation 1
(Endothermic)

Partial Oxidation

Hydrogen can also be produced from hydrocarbons using partial oxidation. With efficiencies of the order of 70 -80%, [5] this method requires the reaction of the hydrocarbon with oxygen, ensuring that there is not enough oxygen present to allow complete oxidation of the hydrocarbon to carbon dioxide and water; hydrogen and carbon monoxide is produced instead, as shown in Equation 2:

$C_mH_n + ½\ mO_2 \rightarrow mCO + ½\ nH_2$ Equation 2
(Exothermic)

Autothermal Reforming

Autothermal reforming combines steam reforming with the partial oxidation method as shown in Equation 3 and has reported efficiencies of 71 – 74% [5], however pure oxygen is required for the oxidation otherwise nitrogen from an air mix contaminates the hydrogen product.

$C_mH_n + ½\ mH_2O + ¼\ mO_2 \rightarrow mCO + (½m + ½n)H_2$ Equation 3
(Thermally neutral)

Water Gas Shift

The three methods above all produce H_2/CO outlet products and so a water-gas shift reaction can be employed in order to produce more hydrogen. The carbon monoxide is further reacted with steam using a catalyst via Equation 4.

$CO + H_2O \rightarrow CO_2 + H_2$ Equation 4
(Exothermic)

Steam reforming and the partial oxidation method can be applied to oil and to coal or biomass with a prior gasification step. Hydrogen can also be produced from methanol (CH_3OH) using these processes. In order to avoid the release of CO_2 into the atmosphere, the CO_2 must be captured and stored in spent oil and gas fields or saline aquifers. However the longevity of such stores is debated. Therefore methods of hydrogen production which result in fewer emissions are of interest. Hydrogen production methods that theoretically do not emit greenhouse gasses are briefly discussed below.

1.3.2 Low Emission Hydrogen Production

Photolysis

Photolysis harnesses green algae's photosynthesis process, which use sun light and CO_2 to form carbohydrates and oxygen. When too much solar energy is captured by the organism it releases excess hydrogen. Much work is still needed to engineer algae with high and efficient hydrogen yields. As of 2013 light to hydrogen efficiency was about 15%%. [7]

Photo-electrolysis

Photo-electrolysis also relies on solar energy but uses semiconductor materials similar to photovoltaics, rather than biological technologies. One type of photo-electrolysis cell comprises of a photoanode, an n-type material with an excess of electrons immersed in an aqueous electrolyte. A photon with energy greater than that of the bandgap of the material hits the anode, releasing an electron to flow to the electronically connected cathode and

leaving a hole which decomposes water into H^+ and O_2(g). The hydrogen ions pass through the electrolyte to combine with the electrons at the cathode forming hydrogen. [8] This method displays efficiencies of 10 -14%. [5]

Thermochemical water splitting

Water decomposes at 2500^{o}C, however finding materials that can resist degradation at this temperature is problematic. Chemical reagents are available that reduce the decomposition temperature but generally operate at higher pressures. [8] The combination of high temperature, high pressure and often corrosive materials means that this process still requires materials resistant to degradation.

1.3.3 Electrolysis

Electrolysis is the splitting of water using an external electric current. The forms of electrolysis are briefly described below.

Alkaline electrolysis

This system consists of an alkaline electrolyte, KOH or NaOH, a platinum coated nickel cathode and a metal oxide coated nickel anode. Water is supplied to the cathode where it dissociates into H_2 and OH^-, the OH^- is conducted through the electrolyte to the anode where O_2 is formed. This method is the most mature and cheapest in terms of capital cost of the electrolysis systems.

Proton exchange membrane electrolysis (PEM)

PEM cells are made of two electrodes separated by a solid proton conducting Nafion membrane. Water is supplied to the anode where it dissociates into H^+ and O_2, the protons

are conducted through the membrane to the cathode where they join with electrons to form hydrogen gas. The solid membrane is safer than using liquid alkaline electrolytes and ensures the formation and separation of pure H_2. However this technology is still being developed and currently costs more than alkaline systems.

Solid oxide electrolysis cell (SOEC)

This system acts in the same direction as alkaline electrolysis, conducting oxygen species through the electrolyte which in this case is a solid oxygen conducting ceramic. SOECs are operated at high temperatures in order to reduce the external electricity demand. Heat may be supplied by geothermal or solar sources, or waste heat from conventional power sources such as nuclear power plants. SOECs are currently the most efficient electrolysis system with efficiencies of 45 – 65% reported,[9] but face issues related to thermo-mechanical stress as well as seal and interconnect stability and cell degradation.

For further details and other, less developed, methods of hydrogen production the following references are recommended: [8] and [10]

The focus of this thesis is hydrogen production using solid oxide electrolysis cells (SOECs). The theory and operation of solid oxide electrolysis cells is discussed in further detail below.

1.4 Solid Oxide Electrolysis

In solid oxide electrolysis an external electrical input converts water steam into oxygen and hydrogen, which when re-combined using a Solid Oxide Fuel Cell (SOFC) produces water and electricity. If the electrical input is from a nuclear or renewable source then little to zero CO_2 is emitted. Along with being a bridging technology for a hydrogen economy, electrolysis and fuel cells act as energy storage, storing the energy from intermittent renewable sources in the form of hydrogen until a time when it is needed.

The basic operation of an SOEC system is shown in Figure 1.

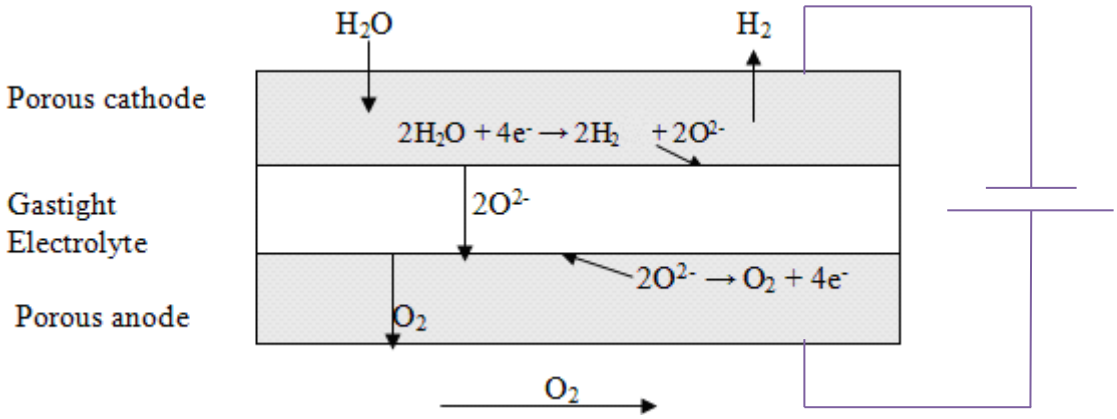

Figure 1. The combination of cathode, electrolyte and anode and the chemical reactions taking place at each for a SOEC.

Water is supplied to the porous, electronically conducting, negative cathode where it migrates to the electrolyte surface and is dissociated into hydrogen and oxygen by an external supply of electrons. The hydrogen then travels back to the cathode surface whilst the oxygen ions are transported through the solid, oxygen ion conducting, electrolyte membrane to the anode. At the anode the oxygen ions are oxidised to form oxygen molecules. The general processes are shown in Equations 5 and 6:

Cathode (–): $H_2O(g) + 2e^- \rightarrow H_2(g) + O^{2-}$ Equation 5

Anode (+): $O^{2-} \rightarrow ½\ O_2(g) + 2e^-$ Equation 6

Up to 90% by volume of the exiting gas on the cathode side may be H_2. This gas may then be passed through a condenser or gas separator in order to separate the hydrogen from the steam. [11]

If the cathode is purely electronically conducting Equation 5 occurs at the triple phase boundary (tpb) where the gas phase, electrode phase and electrolyte meet. If the electrode material is a mixed ionic and electronic conductor (MIEC) then the active area at which reactions can take place is greatly enhanced.

If oxygen ions are transported through a MIEC electrode material by oxygen vacancies in the lattice, the processes occurring at the anode and cathode are described by the Kröger-Vink notation in Equations 7 – 9:

Cathode: $H_2O(g) + V_o^{\bullet\bullet} + 2e' \rightarrow H_2(g) + O_o^x$ Equation 7

Anode: $O_o^x \rightarrow 2e' + ½O_2(g) + V_o^{\bullet\bullet}$ Equation 8

Total: $H_2O(g) \rightarrow H_2(g) + ½O_2(g)$ Equation 9

Figure 2 illustrates the reversible nature of SOECs and SOFCs.

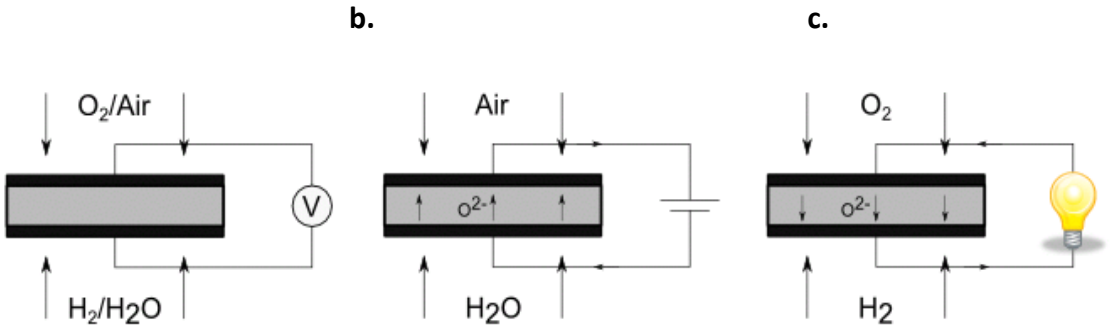

Figure 2. Modes of operation of SOECs. a: Open circuit operation. b: Closed circuit operation SOEC. c: Closed circuit operation SOFC.

Figure 2a depicts open circuit operation of a SOEC. The ionic species can't travel to the lower concentration as the resistance of the voltmeter is too large, as such a potential is set up across the cell and no net current flows. [12] This open circuit voltage (OCV) can be predicted by the Nernst equation which relates the chemical equilibrium, the potential and the energy that is causing the charge to flow (in this case none): [13]

$E = E_o - (RT/nF).lnQ$ Equation 10

Where E is the OCV under given conditions and E_o is the OCV under standard conditions. R is the gas constant, T the temperature, n the number of moles of electrons transferred between oxidizing and reducing agents, F is the Faraday constant and Q is the reaction quotient. The reaction quotient relates the concentrations of the reactants and products:

$$Q = \frac{[C]^c[D]^d}{[A]^a[B]^b}$$ Equation 11

Where, in a reversible reaction:

$aA + bB \leftrightarrow cC + dD$ Equation 12

The OCV can also be measured directly and when compared against the theoretical value any gas leaks between the anode and cathode can be determined. A leak of gas causes a lowering of partial pressure difference which decreases the measured OCV. [14]

Figure 2b depicts closed circuit operation of an electrolyser. The flux (atoms per second) is given by Faradays law:

I/nF Equation 13

Where I is the current, F the Faraday's constant and n the number of electrons involved in the reaction. [12] The charge sets up the potential of the cell. In this process $n = 2$ since two electrons from the external supply dissociate the water molecule into hydrogen and an oxygen anion.

Figure 2c depicts fuel cell mode, an external load allows the passage of electrons from the negative anode, where hydrogen fuel is oxidised, to the positive cathode where oxygen gas is reduced. Oxygen ions travel through the electrolyte to form H_2O at the anode.

The materials for electrolysis and fuel cell modes of operation require different optimisations since the reactions taking place are the reverse of one another. For example a solid oxide fuel cell requires airflow to avoid overheating from exothermic hydrogen oxidation and ohmic heating, whereas in SOEC mode hydrogen reduction is endothermic. [11] Therefore if a single reversible SOFC/SOEC is desired, compromises may have to be made in performance.

1.4.1 Thermodynamic Considerations

For electrolysis to occur, thermodynamics determines the minimum energy required to split pure H_2O into hydrogen and oxygen. Starting from the first law of thermodynamics it is determined that the theoretical minimum voltage required to split water is 1.23V at a room temperature of 25^{o}C. [15] However, due to inefficiencies in the electrochemical cell, the required potential for hydrogen production is greater than this. Between the voltages of 1.23V and 1.48V a decreasing amount of energy is absorbed and the reactions become less endothermic. [16] Above 1.48V the reaction is exothermic, wasting electrical energy which is emitted as heat. [11] The overpotential is thus defined as the difference between the supplied potential and the theoretical potential needed to produce H_2 at a given temperature. [16]

Figure 3 shows that as operation temperature increases the overall energy demand also increases, however the amount required in the form of electrical energy decreases. As over two thirds of the cost of the process arises from the electrical consumption, a decrease in electricity demand leads to a reduction in cost. [14] High temperature operation is also advantageous for the ionic conductors of solid oxide fuel cells and solid oxide electrolysis cells (SOFCs/SOECs) as conductivity increases with increasing temperature.

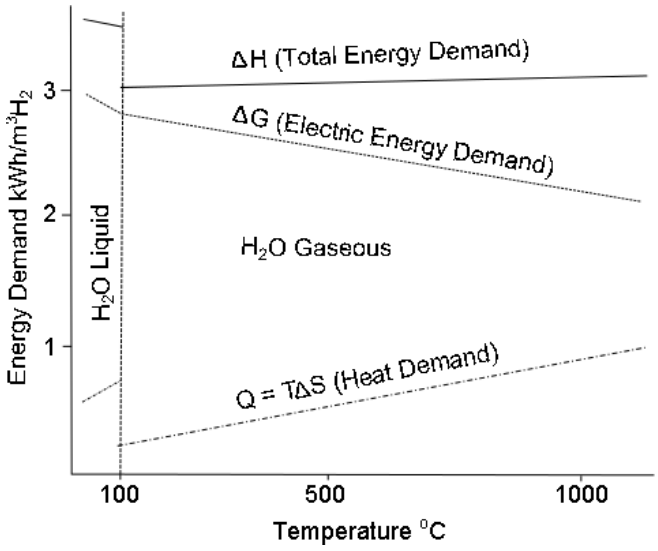

Figure 3. Graph showing heat (Q), electrical (ΔG) and total (ΔH) energy demands change with temperature. Image adapted from reference [14]

1.4.2 Electrolysis Efficiency

The total energy needed for high temperature steam electrolysis, ΔH, is comprised of the required thermal energy, Q_{es}, and the Gibbs free energy, ΔG, the minimal electrical work necessary:

$\Delta H = Q_{es} + \Delta G$ Equation 14

This is shown graphically in Figure 3 above. Although total energy required increases with increasing temperature, electricity demand is reduced which increases the thermal-to-hydrogen efficiency.

Yildiz et. al. [17] determined efficiency assuming that the heat from a source (namely nuclear reactor, Q_N) is split into two paths, one for power conversion for electricity generation and the other for high temperature steam electrolysis processes:

$Q_N = Q_{N,el} + Q_{N,es}$ Equation 15

Where $Q_{N,el}$ is the thermal energy used for electricity production and $Q_{N,es}$ is the thermal energy required to heat the steam, which Yildiz et. al assumed to be loss free. The Gibbs free energy of the electrical energy for electrolysis is written:

$\Delta G = \eta_{el} \, . \, Q_{N,el}$ Equation 16

where η_{el} is the electric power efficiency.

The ideal thermal-to-hydrogen production efficiency of high temperature steam electrolysis ($\eta_{H,HTSE,ideal}$) is the ratio of energy carried by the hydrogen produced ($Q_{H,out}$) to the amount of thermal energy required to produce that hydrogen (Q_N) [11] i.e.:

$$\eta_{\mathrm{H,HTSE,ideal}} = \frac{Q_{H,out}}{Q_N} = \frac{\Delta H}{Q_{N,el} + Q_{N,es}}$$ Equation 17

where ΔH is the change in enthalpy. Therefore:

$$\eta_{H,HTSE,ideal} = \frac{\Delta H}{\Delta G / \eta_{el} + Q_{N,es}}$$ Equation 18

Due to Equation 14, $\eta_{H,HTSE,ideal}$ can be written:

$$\eta_{H,HTSE,ideal} = \frac{\Delta H}{\Delta H + \frac{1-\eta_{el}}{\eta_{el}}.\Delta G} \qquad \text{Equation 19}$$

Two assumptions have been made in order to arrive at Equation 19, firstly that the thermal and electrical energy supplied by the source is equal to the heat generated during electrolysis due to polarization and so no net heat is generated in the cell. Secondly it is assumed that there is no thermal energy loss whilst heating the steam. In reality there will be losses due to polarization and ohmic losses which are given the symbol Q_{loss} [17]:

$$\eta_{H,HTSE,ideal} = \frac{\Delta H}{\Delta G/\eta_{el} + Q_{N,es} + Q_{loss}} \qquad \text{Equation 20}$$

where

$$Q_{loss} = \frac{\Sigma E_{pol}}{\eta_{el}} \qquad \text{Equation 21}$$

As temperature increases, polarization energy, E_{pol}, and therefore Q_{loss} decrease, improving the efficiency of the system. A further way to improve efficiency of the system would be to use the exit heat from the H_2 and O_2 outlets to preheat the H_2O entering the system, thereby reducing the thermal energy requirement from the heat source. [17]

1.4.3 Sources of Overpotential

An ideal SOEC would electrolyse water at the Nernst potential, however realistically there are a number of sources of overpotential and ohmic losses. Generally the overpotential comes from: reaction activation polarization; species concentration polarization; crystal boundary electrolyte resistance; ohmic resistance of anode, electrolyte, cathode [11] and their connections. These terms are described in more detail below and Figure 4 shows at what point in the electrolysis system some of these resistances occur.

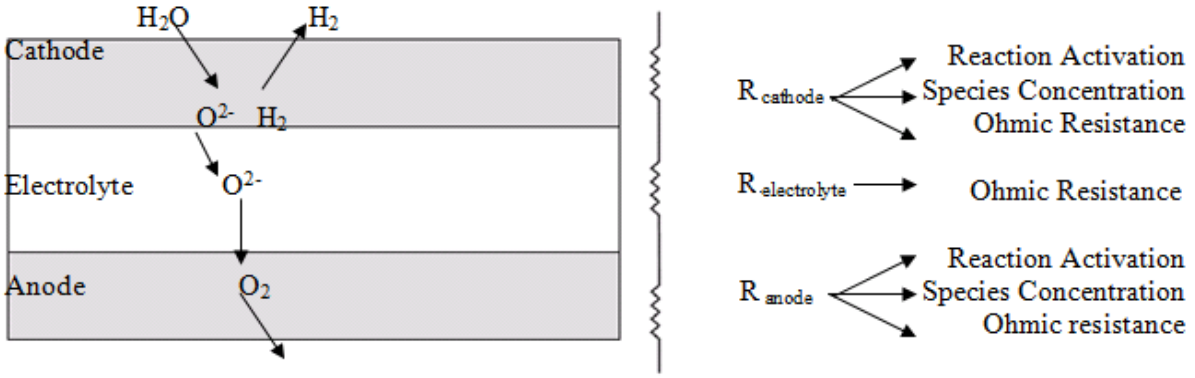

Figure 4. Energy loss mechanisms of overpotential in SOEC.

Activation overpotential relates to the rate of electrochemical reactions taking place on the electrode surface; high current density and good charge transfer properties will reduce activation overpotential.

Concentration (mass transfer) overpotential describes how well reactants are supplied to the reaction sites of the electrode. The product concentration at the electrode surface should be efficiently removed in order to ensure the reactant concentration remains high.

Grain boundary overpotential relates to the grain boundary of the electrolyte impeding the conduction of ions. [18] Larger grain sizes therefore reduce the total grain boundary surface area, reducing this source of overpotential. [19]

Ohmic overpotential is the ohmic resistance of the apparatus (wires, anode, electrolyte, cathode) to electron and ion transfer, which is equal to the product of cell resistance and current, *IR*. [11]

Methods to reduce overpotential include increasing the reactant partial pressure in order to improve transfer to the electrode, reducing the thickness of the electrolyte to reduce ohmic resistance, and increasing the temperature of operation which increases the use of direct heat requirement and reduces the need for electrical energy. Wang et al. [20] found that pure O_2, rather than air, fed to the electrolyser anode decreased impedance, as did increasing the cathode polarization current.

1.4.4 SOEC Material Properties

The electrolyte of both SOECs and SOFCs is usually inorganic and should be dense in order to avoid mixing the reactants. The electrolyte conducts ions only, as electronic conduction would result in a short circuit of the system. Electrodes are electronically conducting, thin and porous to ensure reactant gas has access to the triple phase boundary (tpb), the points where the gas, electrode and electrolyte phases meet and the reactions can occur. Use of a mixed ionic and electronic conductor (MIEC) electrode increases the area available for reaction. MIECs can be composites of an ionic conducting material with an electronic conducting material, however a single phase MIEC is theoretically advantageous as all the surface is available for reactions to take place. The mechanisms and theory of mass transport and ion conduction is discussed below and a review of electrolyte and electrode materials in the literature is presented in Chapter 2.

It is also important that the electrodes and electrolyte materials are stable and unreactive under operating conditions and have similar thermal expansion coefficients in order to avoid damage during operation. Although beyond the scope of this thesis, research is also needed for suitable connecting materials, as those which are capable of withstanding high temperature operation are often expensive alloys. [11]

1.4.4.1 Electrical Conductivity

Electrical conductivity is a measure of a material's ability to transport charge particles under the application of an electric field. [21] The electrical conductivity, σ, is given by Equation 22:

$$\sigma = \sum c.\mu.z.e \qquad \text{Equation 22}$$

where c is the concentration of mobile charge carriers, μ the electrical mobility, z the valence of the particle and e the charge of an electron. Electrical mobility, μ, is given by Equation 23:

$$\mu = \frac{z^2 e^2 D\, c}{kT}$$ Equation 23

where μ, z, e and c are the same as above and D is the diffusion coefficient, k is the Boltzmann constant and T is the temperature.

The Nernst-Einstein relationship given in Equation 24 combines Equations 22 and 23:

$$\sigma = \frac{z^2 e^2 D}{kT}$$ Equation 24

Total conductivity of a ceramic can be made up of a combination of electronic conduction of holes and electrons, ionic conduction of vacancies or interstitial ions, or a combination of the two, i.e. a mixed ionic and electronic conductor.

1.4.4.2 Ion Conduction Mechanisms

It is important to understand the mechanisms through which ions are conducted in the electrolyte and electrode materials. Mass transport of oxygen ions through a ceramic oxide material occurs through diffusion, the movement from an area of high concentration to an area of lower concentration. It is defects within the crystal, resulting from non-stoichiometry, that allow ions to be transported. In ceramic oxides these defects are commonly oxygen vacancies or oxygen interstitials.

Ionic conductivity is temperature dependant, the extent to which depends on the material and defect type. In SOEC and SOFC literature defect concentrations are increased by doping materials with oxides with a greater or lesser valence number, examples of which are given in Chapter 2

Vacancy

The vacancy mechanism occurs when an ion 'hops' from its lattice site to a vacant equivalent site, as shown in Figure 5. The ion leaves a vacancy on the originally occupied site and so the vacancy moves in the opposite direction to the ion.

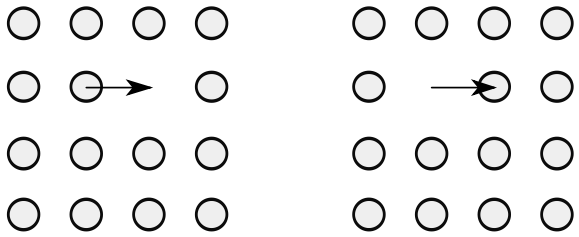

Figure 5. Ion migration via vacancy mechanism, the ion moves from lattice site to adjacent vacant lattice site.

Interstitial

Another common diffusion mechanism is that of interstitial atoms. Interstitial defects are an effect of over stoichiometry, the atoms lie in an interstitial position rather than on a crystal lattice position and move from one interstitial site to another, either by a direct or an indirect mechanism as shown in Figure 6 and Figure 7.

Direct migration is where the interstitial atom moves to another interstitial site in one step and can repeat this motion through the crystal lattice. This method is more common for smaller atoms such as hydrogen and is shown in Figure 6.

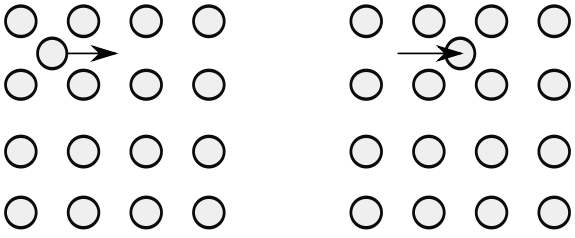

Figure 6. Ion migration via direct interstitial mechanism, the ion moves from interstitial site to adjacent interstitial site.

The indirect interstitial mechanism is displayed in Figure 7 and is a two-step process whereby the interstitial atom moves to an occupied lattice site, displacing the former occupant to an interstitial position.

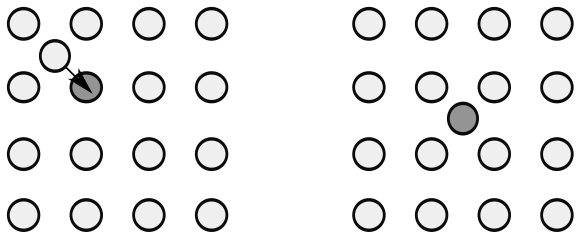

Figure 7. Ion migration via indirect interstitial mechanism, the ion moves from interstitial site to an occupied lattice site, displacing the occupant ion (dark circle) into an interstitial site.

1.4.4.3 Electronic Conductivity

In a metal, electronic conductivity decreases with increasing temperature as mobility decreases and electron concentration is largely temperature independent. However in semiconductors and insulators electronic concentration can be significantly temperature dependant, depending on the material.

In SOFCs and SOECs the electrolyte is required to be ionically conducting and the electrodes mixed ionic and electronic conductors. It is therefore necessary to develop materials that display high conductivities of the desired type (ionic, electronic or mixed) at operating temperatures.

1.5 Chapter Summary

In this chapter fuel cell technology was presented as a low carbon technology that can be adopted to reduce the amount of man-made greenhouse gas emissions. For the process to be truly carbon-free the fuel must be hydrogen and the method of hydrogen production must also emit no greenhouse gasses. A number of zero-carbon hydrogen production methods were presented and solid oxide electrolysis cells (SOECs) will be the focus of this thesis. The thermodynamics and efficiencies of SOECs were briefly discussed along with common sources of overpotential. An understanding of the different forms of charge conduction within such a system was also presented.

Chapter 2 – Literature Review

As discussed in Chapter 1, materials for SOFCs and SOECs must have a number of appropriate properties. Electrolytes must have high ionic conductivity and be dense in order to effectively separate reactant and product gases. Electrodes must have high ionic and electronic conductivity and be porous in order to aid reactions. All materials must be chemically and mechanically stable under working temperatures and atmospheres.

In this chapter a review of the materials used in SOFCs and SOECs is presented. An overview of the more common and well understood electrolytes is presented followed by a discussion of common and novel electrode materials. A discussion of the K_2NiF_4 electrode material is given paying particular attention to $La_2NiO_{4+\delta}$ (LNO) performance and stability. The apparent predisposition to fuel cell research over electrolysis is also explored with discussion on how this may affect electrolysis research.

2.1 Electrolyte Materials

It is recognised that electrolyte ionic conductivities of the order of $1x10^{-2}$ $S.cm^{-1}$ are required for competitive SOFC/SOEC performance. [21, 22] Materials that have widely demonstrated promising electrolyte properties are yttria stabilised zirconia (YSZ); gadolinium or samarium doped ceria (CGO or CSO); and strontium and magnesium doped lanthanum gallate (LSGM). [22] Investigation into electrolyte material for solid oxide devices has commonly focused on these materials. The conductivity mechanisms, merits and disadvantages of each material are discussed below.

2.1.1 Yttria Stabilised Zirconia (YSZ)

Historically the most common electrolyte material for solid oxide devices is yttria stabilised zirconia (YSZ). This material displays suitable conductive and mechanical properties at high temperatures and for a wide range of oxygen partial pressures. [23] Doping of ZrO_2 is

required in order to stabilise the structure into the highly symmetric cubic form, Figure 8, and to allow oxygen conduction via oxygen vacancies.

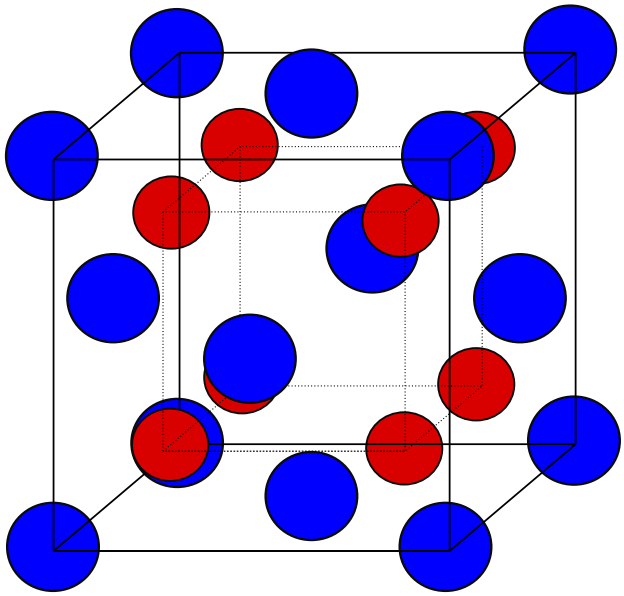

Figure 8. Cubic fluorite, face centred unit cell. Blue spheres: cations, Red spheres: oxygen ions.

Zr^{4+} in ZrO_2 is too small to adopt an ideal cubic fluorite structure unless at high temperature or doped with larger cations. [24] As temperature increases the ZrO_2 structure reversibly changes from monoclinic to tetragonal to cubic. [25] These structural changes are associated with volume changes which can result in cracking of the ZrO_2 material on cooling. To reduce these volume changes the addition of an oxide stabilises the tetragonal and/or cubic phases. Amongst others Sc_2O_3 [26], Y_2O_3 [27], MgO and CaO [28] dopants have been tested. The addition of such lower valence ions also leads to the formation of oxygen vacancies within the structure:

$$M_2O_3 \xrightarrow{ZrO_2} 2M'_{Zr} + 3O_0^x + V_o^{\bullet\bullet}$$

This permits the passage of oxygen ions through the structure that would not occur if the structure were perfect. In order for ions to 'jump' from site to site, vacancies are required along with thermal energy to overcome the energy barrier associated with such a transition.

An optimum doping level is present, above which immobile defect clusters form, thereby reducing conductivity. The optimum doping level is dependent on the doping species but is typically between 8 – 12 mol% Y_2O_3. For YSZ the optimum doping level is 8 mol% Y_2O_3. [27] YSZ has ionic conductivity of the order 0.1 $S.cm^{-1}$ at 1000^oC [29] however there is consensus that operating temperatures must be lower than this for practical SOFC/SOEC use. Reducing electrolyte thickness reduces electrolyte resistance, however down to 15µm thickness, the limit of conventional processing, [30] ionic conductivity is not significantly increased.

It is also noted that zirconia based electrolytes are reactive with perovskite electrodes containing lanthanum or strontium, forming $La_2Zr_2O_7$ and $SrZrO_3$ resistive layers at high temperatures. [21, 22]

2.1.2 Doped Ceria

Ceria, CeO_2, has the cubic fluorite structure and, like YSZ, becomes an oxygen ion conductor when doped with aliovalent species. Gadolinium (Gd_2O_3)- or samarium (Sm_2O_3)-doped ceria (CGO and CSO respectively) are alternative electrolytes studied for SOFCs that have been shown to produce higher conductivities at lower temperatures than YSZ. [22] Dopant levels of 10 – 20 mol% Gd_2O_3 or Sm_2O_3 are most commonly reported for these materials. CGO ionic conductivities of 0.01 $S.cm^{-1}$ at 500^oC ($Ce_{0.9}Gd_{0.1}O_{1.95}$) [30] and 0.25 $S.cm^{-1}$ at 1000^oC (composition not stated) [31] have been reported. The drawback of CGO is its instability at low pO_2, becoming electronically conductive at temperatures above ~600^oC as Ce^{4+} is reduced to Ce^{3+}. [23] Electronic conduction short circuits the electrolysis/fuel cell system and is therefore not desired. The lattice change associated with reduction can also lead to mechanical failure of the system. [32] Reducing operating temperature limits Ce^{4+} reduction but compromises ionic conductivity. [27] More recently samarium (Sm_2O_3)-doped ceria, CSO, has been investigated for electrolyte material and displays high ion conduction; $(CeO_2)_{0.8}(SmO_{1.5})_{0.2}$ displays a conductivity of 0.56 $S.cm^{-1}$ at 800^oC. [33] Investigations are divided as to which material, CGO or CSO, produces the higher conductivity and any significant differences are likely due to processing techniques and morphology differences. [34]

Tsoga et al. [35] used a CGO interlayer between a YSZ electrolyte and LSC ($La(Sr)CoO_3$) cathode for fuel cell use, the CGO acted as a barrier stopping reaction of the YSZ and LSC, the electronic conduction of CGO then became a benefit. However it was noted that there are also chemical compatibility problems with the CGO interlayer/YSZ inter-diffusing during the sintering process, and so another protective layer is required to avoid reactions taking place, in this case a composite of CGO and YSZ was used.

The highest oxygen ion conductivity is recorded as ~2.3 $S.cm^{-1}$ at 800^{o}C for face centred-cubic δ-Bi_2O_3. [36] This highly conducting phase is only stable between 730^{o}C and 804^{o}C, the melting point. Below 730^{o}C this material is monoclinic in structure and displays conductivities on a par with YSZ. On cooling the material can undergo a number of phase changes from the metastable tetragonal β-phase at 630^{o}C or the second-body-centred-cubic *γ* phase also at 630^{o}C before forming the stable monoclinic phase. It is therefore of interest to stabilise δ-Bi_2O_3 for mechanical stability and high ionic conductivity. Substitution of Bi for WO_3, Y_2O_3, or Gd_2O_3 have been demonstrated to stabilise the δ-phase to as low as room temperature. [36] Substitution does reduce the conductivity, but not significantly; however further research is required to prevent detrimental aging and further phase transformations.

2.1.3 Lanthanum Strontium Gallate Magnesite (LSGM)

Lanthanum gallate ($LaGaO_3$) has a cubic perovskite structure ABO_3 where A and B are cations; in this case A = La, B = Ga. This structure is shown in Figure 9:

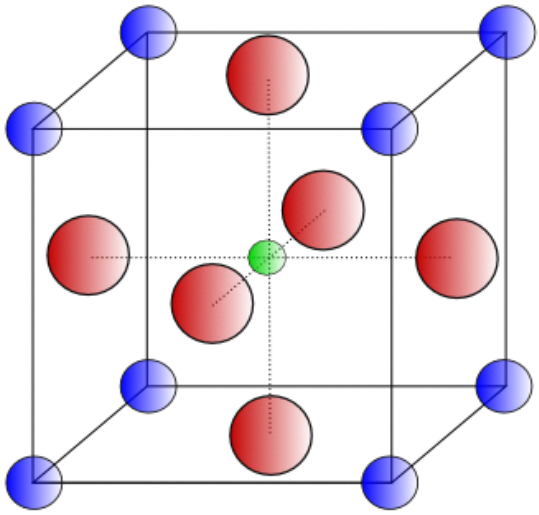

Figure 9. Cubic perovskite, unit cell. Blue spheres: A cations, Green sphere: B cation, Red spheres, oxygen anions.

When doped with SrO and MgO on the A and B sites respectively, $La_{1-x}Sr_xGa_{1-y}Mg_yO_{3-\delta}$ (LSGM), this material conducts oxygen ions. As with ZrO_2 and ceria based electrolytes, substituting $LaGaO_3$ with low valence oxides introduces oxygen ion conductivity via oxygen vacancies in the lattice. The conductivity is reported to be high, of the order of 0.01 $S.cm^{-1}$ at 600^{o}C [31, 36] with the advantage of low electronic conductivity even in reducing atmospheres. [23] Bulk ionic conductivity is reported to be highest in the LSGM composition $La_{0.8}Sr_{0.2}Ga_{0.83}Mg_{0.17}O_{2.815}$ displaying 0.01 $S.cm^{-1}$ at 600^{o}C [36] Although Steele et al. [30] claim the composition $La_{0.9}Sr_{0.1}Ga_{0.8}Mg_{0.2}O_{2.85}$ displays the highest conductivity but is not stable at low temperatures, this reference does not state a value of conductivity.

There are a number of reported reactions between LSGM and electrode materials. When used in conjunction with a NiO electrode material, oxygen ion insulating phase $LaNiO_3$ is formed. [27] Inter-diffusion of species was observed when LSGM was used with $La_{0.5}Sr_{0.5}CoO_{3-\delta}$ (LSC), an electronically conducting electrode. In this case migration of Co and Ga into the interface was detected from the LSC and LSGM respectively. [36] LSGM is reportedly only suitable for use in the intermediate temperature range ~500-800^{o}C as partial reduction of Ga followed by vaporisation of Ga and Ga_2O from the surface occurs above this temperature range. [27] Philippeau et al. [37] noted the formation of $LaSrGa_3O_7$, $Sr_4Ga_2O_7$ and La_2O_3 phases when LSGM is sintered with an electrode material (in this case La_2NiO_4) at

1150^{o}C. Therefore reactions may not occur with the electrode material either during sintering or electrolysis/fuel cell operation so long as cell fabrication and operation temperatures are kept below 1150^{o}C, however undesirable phases may still segregate from the LSGM electrolyte material during electrolyte pellet preparation as this process typically involves sintering the pellet to ~1400^{o}C.

For all electrolytes discussed in this chapter there is a step change of activation energy, E_a, within the typical SOEC/SOFC working temperature regime (300 – 1000^{o}C) dependant on material composition. Higher activation energy is regularly observed at lower temperatures and increases in value with higher doping due to the formation of immobile ordered-vacancy clusters. A change to lower activation energy above a certain temperature may imply that immobile defect clusters disassociate thereby removing some of the energy barrier for ion conduction. [36]

2.1.4 $LaNb_{0.84}W_{0.16}O_{4.08}$

A new electrolyte material, $LaNb_{0.84}W_{0.16}O_{4.08}$ (LNW), is included in this review as there is some suggestion that this material both allows conduction of oxygen ions via interstitial defects, and shows enhanced performance in electrolysis mode. [38] This material displays ionic conductivity on a par with YSZ, ~0.1 S.cm^{-1} at 1000^{o}C and low electronic conductivity down to 10^{-22} atm. In preliminary investigation this material shows no reactivity with common electrode materials Ni-YSZ and LSM. It is theorised that the enhancement in electrolysis mode is due to the material's ability to incorporate excess oxygen ions, formed at the electrode/electrolyte interface during electrolysis. However this material has only recently been presented and much more work is required to fully determine its structure and properties.

A summary of the common electrolytes used in electrochemical cells is presented in Table 1.

Table 1. Comparison of the advantages and disadvantages of current electrolyte candidate materials.

Material	Advantages	Disadvantages	Conductivity
YSZ	Excellent mechanical stability in oxidizing and reducing environment. Mature, well studied material, >40000 hr of fuel cell operation demonstrated. High quality raw materials available. [39]	Low ionic conductivity compared to other electrolytes. Incompatible with some cathode materials.	0.1 $S.cm^{-1}$ at $1000^{o}C$ [29]
CGO	Higher ionic conductivity than YSZ. Good compatibility with cathode materials.	Poor mechanical stability. Electronic conductivity leading to short circuit in reducing atmospheres.	0.25 $S.cm^{-1}$ at $1000^{o}C$ [31] 0.01 $S.cm^{-1}$ at $500^{o}C$ [30]
CSO	Higher ionic conductivity than YSZ. Good compatibility with cathode materials.	Less mature material for electrolyte. Electronic conductivity leading to short circuit in reducing atmospheres.	0.56 $S.cm^{-1}$ at $800^{o}C$. [33]
LSGM	Higher ionic conductivity than YSZ. Good compatibility with cathode materials.	Ga evaporation at low pO_2. Incompatible with NiO. Poor mechanical stability.	0.01 $S.cm^{-1}$ at $600^{o}C$ [31, 36]
LNW	Conductivity of the same order of magnitude as YSZ Apparent compatibility with Ni-YSZ and LSM	Understudied	~0.1 $S.cm^{-1}$ at $1000^{o}C$ [38]

2.2 Electrodes

Electrodes should be chemically and mechanically stable, they should also catalytically assist the desired reactions and be both ionically and electronically conductive. The morphology of the electrodes should be porous in order to provide a great number of reaction sites, in other words a greater surface area of triple phase boundary. Porosity also allows the migration of gases to and away from the reaction sites.

2.2.1 Fuel Electrodes

At the negative cathode of a SOEC, hydrogen is being created and oxygen ions are drawn to the electrolyte. Steam is supplied to this electrode and oxygen partial pressures can be of the order of 10^{-12} – 10^{-16} atm. [40] In these conditions metal electrodes such as Pt, Ni and Co can be implemented, however these only display electronic conductivity. A cermet is produced when the metal is mixed with an ion-conducting ceramic material, often the same material as the electrolyte. A cermet therefore provides a much greater number of triple phase boundary points at which reaction can occur. A common SOEC cathode cermet is nickel/YSZ (Ni/YSZ). [11] [4] [17] This material must be reduced before it is an active cathode for steam electrolysis, and there is reported Ni agglomeration degradation after electrolysis operation, reducing the number of triple phase boundary points. [11] [41]

Marina et al. [41] found that lanthanum-substituted strontium titanate/ceria composite ($La_{0.35}Sr_{0.65}TiO_3$ – $Ce_{0.5}La_{0.5}O_{2-\delta}$) performed better than Ni/YSZ during electrolysis, producing higher current densities and not suffering from agglomeration. Another reported cathode is samaria-doped ceria (CSO) with highly dispersed Ni catalysts, however beyond these materials there has been relatively little investigation into electrolysis cathodes. This may be due to the fact that of the two electrodes, the negative cathode (anode in the case of a SOFC) presents the lower overpotential. As the electrodes assist different reactions the

overpotentials associated with each electrode are different, the positive anode (cathode in the case of a SOFC) accounts for a larger portion of the inefficiency of the system.

2.2.2 Oxygen Electrodes

At this electrode, oxygen is delivered to a highly oxidising environment. Noble metals can be used, however should be eliminated due to high cost. As was the case with the fuel electrode, mixed ionic and electronic conducting materials are desired. Currently the most common SOEC anodes have centred on testing known successful SOFC cathodes, for example the perovskite strontium doped lanthanum manganite, $La_{1-x}Sr_xMnO3$, (LSM). This is a popular SOFC cathode due to its high electrical conductivity, stability and compatibility with common electrolytes. [22] [40] Doping Sr^{2+} on the La^{3+} site improves p-type conductivity as the Mn^{4+} concentration is increased, but it has the disadvantage of increasing the thermal expansion coefficient. [42] Another disadvantage of LSM is that it is not ionically conductive. [43] An option is to mix LSM with an oxide ion-conductor in order to form a composite with greater triple phase boundary (tpb) length, often the same material as the electrolyte is chosen in order to reduce thermal expansion mismatch between electrode and electrolyte. In order to increase the tpb further, mixed ionic and electronic conducting materials have been researched as alternative electrode materials and are discussed below.

Along with LSM, Sr-doped $LaCoO_3$ (LSCo), Sr-doped $LaFeO_3$ (LSF), and Sr and Fe doped $LaCoO_3$ (LSCF) have been tested as the positive electrode on YSZ electrolytes but the formation of insulating layers of $La_2Zr_2O_7$ or $SrZrO_3$ is noted to be a problem. [21] [20] [40] [35] Ni et al. [40] suggest that MnO_x from LSM diffuses into the YSZ phase resulting in La_2O_3 or SrO left to react with YSZ to form the insulating phases, therefore over-doping of MnO_x in LSM by a few % reduces the amount of free La_2O_3 or SrO for reaction with the YSZ but reduces the conductivity of the electrode. Conversely, limiting the strontium proportion in LSM is possible, thereby reducing the available SrO to react with YSZ, hence $La_{0.8}Sr_{0.2}MnO_{3-\delta}$

is a common composition of LSM. [21] Laguna-Bercero et al. [44] detected evidence of $La_2Zr_2O_7$ when LSCF or LSM-YSZ composites were used as electrodes in contact with scandia doped ceria stabilised zirconia (ScCeSZ) electrolyte material, but found it to have no adverse effect on performance. However, it was found that the LSM-YSZ composite on ScCeSZ showed degradation after use, which is attributed to a distortion to the rhombohedral β-$Sc_2Zr_7O_{17}$ phase. However Wang et al. [20] claim no formation of the insulating layers when using LSM-YSZ composite of the same composition ($La_{0.8}Sr_{0.2}MnO_3$-YSZ) on a YSZ electrolyte. Composites of YSZ with LSCo and LSF were also studied by Wang et al. [20] and found to form no insulating layers. It was found that LSM-YSZ is a less than ideal electrode material as after an initial improvement of impedance when run in fuel cell mode, the performance decreased during electrolysis mode. The LSCo-YSZ and LSF-YSZ composites showed good initial performance with no need for a preliminary cathode polarization step (fuel cell mode). The LSCo-YSZ anode showed the best initial performance of the three, but was noted to also deactivate after time in electrolysis mode. The LSF-YSZ anode on the other hand was proven to be stable during electrolysis over a short-term time period of 5 hours. [20]

Zhao et al. [45] state that composites of LSM-CGO and LSM-CBO (LSM – $Ce_xBi_{1-x}O_2$) show improved conductivity over LSM-YSZ, and it is shown that LSM-CBO does not form the insulating layers associated with LSM-YSZ. However this was tested as part of a fuel cell set-up and so any possible deactivation in electrolysis mode was not investigated. Hart et al. [46] improved the conductivity of the LSM-YSZ system by applying a functionally graded technique, building up a SOFC cathode on a YSZ electrolyte with a number of LSM-YSZ composite layers consisting of an increasing concentration of LSM further from the substrate. Again, this study did not include testing of the material in electrolysis mode.

Other common SOFC cathodes tested as SOEC anodes include lanthanum strontium copper ferrite (LSCuF) and lanthanum strontium cobalt ferrite (LSCoF). These materials were shown to be less effective as SOEC anodes than as SOFC cathodes. [41] $Sm_xSr_{1-x}CoO_3$ (SSC) is reported to be a good SOFC cathode when used in conjunction with or as a composite with LSGM or CGO electrolytes. [22] $Ba_{0.5}Sr_{0.5}Co_{0.8}Fe_{0.2}O_{3-x}$ (BSCF) is also reported to be a good SOFC cathode material when used in combination with the electrolyte CSO. [22] However, there appears to be little investigation of these systems in electrolysis mode.

Laguna-Bercero et al. [47] suggest $La_2NiO_{4+\delta}$ (LNO) type materials should be studied for use as oxygen electrodes. La_2NiO_4 accommodates oxygen excess via the oxidation of Ni^{2+} to Ni^{3+}. [48] Along with high oxygen ion transportation, another advantage of LNO is its low lattice expansion in changing temperatures and oxygen partial pressures. [22] LNO is able to accommodate excess oxygen under high pO_2 via interstitial sites and can also cope with low pO_2 atmospheres via oxygen loss. The structure and oxygen transport of LNO is discussed further in Section 2.2.3. It is not recommended that this material be used in conjunction with the electrolyte YSZ as interfacial reactions between the electrode and electrolyte have been inferred, forming the insulating $La_2Zr_2O_7$ phase. [22, 49, 50] Rieu et al. [49] tested graded LNO electrode layers on YSZ which included a CGO diffusion barrier, a dense thin LNO layer and a thick porous LNO layer. It was found that the porous LNO layer readily delaminated from the CGO interlayer, but the addition of a dense thin LNO layer improved adhesion and provided more contact points for oxygen diffusion to the electrolyte. Clearly, another option is to use alternative electrolyte materials, studies of LNO in conjunction with the electrolyte LSGM showed no reactivity in air up to $1000^{o}C$. [51]

Table 2 lists the electrodes commonly reviewed in literature along with their individual advantages and disadvantages and example conductivity values. This thesis focuses on the use of $La_2NiO_{4+\delta}$ and so further discussion of this material is presented in the following section.

Table 2. Comparison of advantages, disadvantages and typical electrical conductivity of common electrode materials.

Material	**Advantages**	**Disadvantages**	**Conductivity** **σ_e = electronic** **σ_i = ionic**
LSM	Lower formation of insulating phases compared to other La based electrodes, [20] Well studied, Commercially available, Good TEC match with YSZ	Non-ionically conductive, High doping of Sr reacts with Zr based electrolytes	σ_e = 200 - 300 S.cm^{-1} at 900°C [21] σ_i = Low/zero
LSCo	MIEC, High electronic conductivity.	Reactions with Zr based electrolytes, [35] High TEC [52]	σ_e = 2237 S.cm^{-1} at 800^{o}C [52] σ_i = 0.22 S.cm^{-1} at 800^{o}C [53]
LSCF	Most common electrode material, MIEC, Good TEC match with CGO [52]	Sr diffusion out of electrode causes degradation with time, Lower electronic conduction that LSCo	σ_e = 230 S.cm^{-1} at 900^{o}C σ_i = ~0.2 S.cm^{-1} at 900^{o}C [54]
LNO	MIEC, Well matched TEC,	Less well studied, Lower electrical conductivity, Incompatable with YSZ	σ_e = 76 S.cm^{-1} at 800^{o}C [55] σ_i = ~0.05 S.cm^{-1} at 800^{o}C [56]

2.2.3 K_2NiF_4 Structure

The lanthanide nickelates, Ln_2NiO_4 (Ln = La, Nd, Pr) have the K_2NiF_4 type structures and are described as a stack of alternating perovskite layers ($LnNiO_3$) and rock salt (LnO) layers. The ion conductivity is due in some part to perovskite vacancy transportation [57] and, predominantly, oxygen excess, δ, in the LnO interstitial sites where, in $La_2NiO_{4+\delta}$ (from here on referred to as 'LNO'), the O_i are tetrahedrally coordinated by La^{3+} cations. [22] Figure 10 depicts the K_2NiF_4 structure.

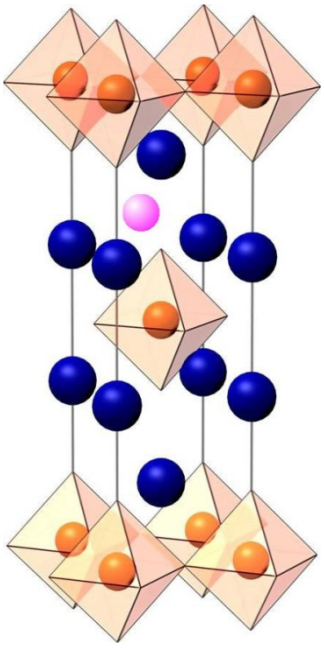

Figure 10. K_2NiF_4 structure showing blue = 'K' cation; orange = Ni; orange oxygen octahera; and pink = oxygen interstitial δ. I4/mmm space group is depicted. [21]

The interstitial oxygen transport is largely limited to the ab rock salt plane. However oxygen ion transport is reported to be high in this material; [58] δ values as high as 0.3 have been reported. [59]

Oxygen interstitials are created by intrinsic anti Frenkel disorder, as well as hole formation as shown below. [21]

$$O_o^x \leftrightarrow V_o^{\bullet\bullet} + O_i''$$

$$\frac{1}{2}O_2 + 2Ni_{Ni}^x \leftrightarrow O_i'' + 2Ni_{Ni}^{\bullet}$$

Therefore oxygen ions are able to travel via interstitials due to the mixed valency of nickel, Ni^{2+} oxidising to Ni^{3+} and creating holes. There is some debate as to whether charge is compensated through Ni^{3+} alone or through a combination of Ni^{3+} and an oxidised lattice oxygen ion as shown below. [21]

$$\frac{1}{2}O_2 + Ni_{Ni}^x + O_0^x \rightarrow O_i'' + Ni_{Ni}^{\bullet} + O_0^{\bullet}$$

Recently Burriel et al. [60] used a suite of complementary surface analysis techniques to determine that the surface, outermost atomic layer of Sr-doped LNO ($La_{2-x}Sr_xNiO_{4+\delta}$) does not include a Ni constituent. This goes against the prevailing theory stated above that assumes, for K_2NiF_4 based materials, Ni at the surface catalyses oxygen transfer from the atmosphere to the electrode. Clearly further work is required to fully understand the mechanisms occurring at the gas/electrode interface.

Structurally, Boehm et al. [43] noted a change of LNO structure from Fmmm to I4/mmm at about 150^{o}C. [43] However it has been noted that the structural transitions are not just dependent on temperature, but are also susceptible to the oxidising nature of the atmosphere, and therefore the stoichiometry of the material. [21] Reports of orthorhombic Fmmm or Bmab are stated for room temperature and when heated tetragonal I4/mmm and F4/mmm structures are reported. [21] [61] The effect of pO_2 atmosphere conditions are discussed in further detail in Section 5.2.

The formation of higher order Ruddlesden Popper (RP) phases ($La_{n+1}Ni_nO_{3n+1}$) has been shown to occur from LNO material under various conditions. Higher order RP phases form when LNO is oxidised and has a similar structure to that of Figure 10 with additional perovskite layers (*n* in total) between the rocksalt layers as shown in Figure 11.

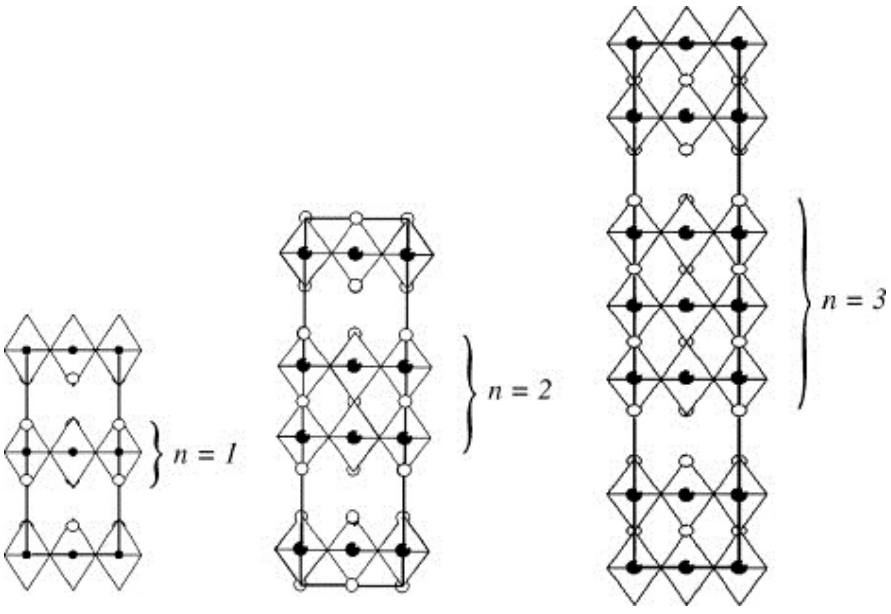

Figure 11. Structure of the Ruddlesden-Popper materials, n = 1, 2 and 3 respectively. [62]

When investigating the increase of interstitial oxygen in LNO by heat treatment, Aguadero et al. [63] found that heat treatment under high oxygen pressure of LNO (1098 K and 250 bar) caused the development of a higher order Ruddlesden Popper phase; lowering the temperature to 873 K supressed the formation of the secondary phase. Platinum has also been shown to catalyse the formation of higher order RP phases above 800^{o}C in air. [21] LNO has also been shown to react with CSO and CGO to form RP phases. [37, 64, 65] However Ferkhi et al. annealed non-stoichiometric LNO ($La_{1.98}NiO_{4\pm\delta}$) and CGO in air at 900^{o}C for 5 hours and subsequently found no reactant phases, [50] highlighting the need for further research in to the effect of stoichiometry on the behaviour of LNO.

Doping of LNO has been widely investigated. Doping the Ni site with high valence transition metal, namely Mn, Fe, Co, Cu and Zn, reportedly increases electronic conduction by increasing the number of holes. [21] [57] However Boehm et al. [43] studied LNO doped with Cu on the Ni site, $La_2Ni_{1-x}Cu_xO_{4+\delta}$, ($0 \leq x \leq 1$) for cathode use in SOFCs and found that as copper content increased electrical conductivity was reduced. Electrical conductivity was also seen to reach a maxima at around 700 – 800 K and decrease at higher and lower temperatures; at lower temperatures the material acts as a semi-conductor whereas at higher temperatures the material loses oxygen which results in a loss of M^{3+} and so carrier density. Another effect of Cu doping was a decrease of oxygen over stoichiometry, δ. Boehm et al. concede that electronic conductivity of LNO does not quite reach the value of 100 $S.cm^{-1}$ stated as required for cathode use within a commercial SOFC, but that doping on the La site would enhance conductivity sufficiently.

An example of doping on the A (La) site is the addition of up to 0.3 Sr^{2+} in place of La^{3+}, reportedly reduces electronic resistance and improves stability. [61] However, it is noted elsewhere, [21] that the addition of Sr increases oxygen vacancies when doped into perovskite materials, and so reduces ionic conductivity in K_2NiF_4 structures since these materials conduct oxygen predominantly via interstitials. Aguadero et al. [61] agree that Sr^{2+} doping in place of La^{3+} decreases ionic conductivity due to the hole doping effect resulting in the oxidation of Ni^{2+} to Ni^{3+} to preserve charge neutrality without the need of excess oxygen. However it is argued that the reduction of ionic conductivity is acceptable for the increase of electronic conductivity which is noted to be poor in LNO. Aguadero et al. also found that ionic and electronic conductivity of $La_{1.9}Sr_{0.1}NiO_{4+\delta}$ could be increased by

applying heat treatment of 650^{o}C and high oxygen pressure of 200 bar to the powders, this treatment increases electrical conductivity and oxygen interstitial concentration.

Laberty et al. [66] tested LNO as a cathode material for SOFC, agreeing that LNO by itself does not act as a good catalyst, despite being a MIEC with reported high oxygen self-diffusion coefficient (D*) and oxygen surface exchange coefficient (k) values, 2 x 10^{-7} cm^2s^{-1} and 2 x 10^{-6} $cm.s^{-1}$ respectively. In this study the authors found that a thin composite cathode of LNO-CSO in conjunction with an LSCo current collector performed better than just a thin LNO cathode on an SOFC cell comprising of YSZ electrolyte on an anode support made of YSZ-Ni composite. Power densities of 2.2 $W.cm^{-2}$ vs. 0.3 $W.cm^{-2}$ at 800^{o}C were observed for composite and single phase electrodes respectively. Sayers et al. [51] tested a layered electrode system consisting of a dense LNO layer in contact with a CGO electrolyte and a porous LNO layer above. It was found that the compact LNO layer improved performance compared to a system with just LNO porous layer and this is attributed to a superior contact between the electrolyte and electrode, thereby improving ion conduction across the interface. Area specific resistances of 7.4 Ωcm^2 vs. 1 Ωcm^2 at 700^{o}C were recorded for the non-dense layer system and dense layer system respectively. Sayers et al. note that the addition of the dense layer improves electrode processes of mass transport and charge transfer suggesting that LNO facilitates oxygen reactions at the triple phase boundary rather than acting as a MIEC, indeed the addition of a Pt current collector reduces the electrode resistances further. However, as mentioned earlier, above 800^{o}C Pt is thought to catalyse the irreversible formation of higher order Ruddlesden-Popper phases, $La_3Ni_2O_{7-\delta}$ and $La_4Ni_3O_{10-\delta}$. Therefore if a Pt current collector is to be used, care must be taken over the operating temperature. Furthermore atmosphere conditions are known to affect LNO stoichiometry therefore further investigation of the catalytic effect of Pt on RP phase formation in various pO_2 is required.

As mentioned above, RP phases have the formula $La_{n+1}Ni_nO_{3n+1}$ increasing *n* has the effect of increasing the number of perovskite layers between the rocksalt layers of the structure. The number of Ni^{3+} increases with *n* thereby increasing the electronic conductivity of the material. For this reason RP phases are studied for electrode material in their own right.

Finally, although not the focus of this thesis, mixed conducting ordered double perovskites have been researched for cathode materials in SOFCs. These have the general formula $AA'Co_2O_{5+x}$ where A is a rare earth or yttrium and A' is Ba or Sr and oxygen transport is via interstitials. It is noted that a wide variety of these materials can be created and only a few have yet been tested, yet those that have exhibit good area-specific resistances and high ionic conductivity. For further discussion on these materials please refer to the reference: [22]

2.3 Chapter Summary

A range of oxide ion conducting electrolytes has been investigated for SOEC and SOFC application. YSZ appears to be the most common electrolyte however efforts are focused on attaining higher ion conductivities at lower temperature regimes. LSGM and gadolinia (Gd_2O_3)- or samaria (Sm_2O_3)-doped ceria display conductivities up to two orders of magnitude greater than YSZ, however the former reacts with Ni electrodes. [40] Ceria based electrolytes appear to be effective, yet can become electronically conductive in reducing environments, however this can be reduced by doping, co-doping or combining with other electrolytes in order to shield from the environment. The material of choice as electrolyte material for this study is LSGM chosen for its stability in a range of pO_2 atmospheres.

The negative electrode is typically a Ni/electrolyte cermet, most commonly Ni/YSZ although the ceramic component may be matched to the electrolyte of choice. It has been shown that there is some interest in negative electrode optimisation within the SOEC/SOFC community, however research is limited compared to that of positive electrode materials. This is because the positive electrode contributes the higher overpotential of the two electrodes.

Investigation into suitable oxygen electrodes is an important area of study for fuel cells and electrolysers. A large number of materials have been considered, largely these are materials of perovskite or perovskite-related structures. Historically the material of choice has been the electronic conductor LSM, however research has been conducted with the aim of

developing materials that are mixed ionic and electronic conductors with high chemical and mechanical stability in conjunction with electrolyte materials in operational temperatures and atmospheres. The materials LSCo, LSF and LSCF have been widely tested as electrode material to some success, reporting satisfactory mixed conductivities although reactivity has been noted with some common electrolyte materials. The creation of composites and graded electrodes made from a mixture of these materials and electrolytes has been found to improve structural compatibility and reduce reactivity. Some work has been conducted in testing solid oxide cells in both electrolysis and fuel cell mode.Despite the research being limited there is evidence that the mode of operation does have an effect on the electrode performance and degree of degradation.

The Ruddlesden Popper family of materials has been developed as an alternate material type for SOFC/SOEC electrode use. Particular attention has been given to LNO (n=1) material which shows good oxygen ion conductivity via oxygen excess. Although some reactivity has been observed between LNO and electrolyte materials, LNO has been shown to be stable with LSGM electrolyte material in operating temperatures. However more research is required into the stability and performance of LNO in operating atmospheres and current distributions, which is the focus of this thesis.

Electrolysis electrodes often seem to be chosen after they are proven to be suitable fuel cell electrodes, which is sensible if ultimately a reversible fuel cell/electrolyser is desired. However, different reactions are taking place, and under different conditions and so the improvement of electrolysis may be found by determining the best materials for the specific job independently from fuel cell investigations.

For further discussion on solid oxide electrolysis and fuel cell materials, the reader is directed to a number of reviews: [30, 67-70]

Chapter 3 – Experimental Methods

3.1 Material Characterisation

Powders of electrolyte material $La_{0.8}Sr_{0.2}Ga_{0.8}Mg_{0.2}O_{2.8}$ and electrode material La_2NiO_4 were commercially supplied by Praxair Speciality Ceramics and CerPoTech respectively. Powder characterisation was determined by particle size analysis, scanning electron microscopy and X-Ray Diffraction as described in the sections below.

3.1.1 Particle Size Analysis

To produce a large electrode surface area for reactions to take place, small electrode particle size is required. The particle size distributions of the LNO powder were studied using a Coulter small volume module LS230 laser diffraction particle size analyser. This instrument determines the size distribution of particles in a sample by irradiating an incident light on powder suspended in distilled water and measuring the angle and intensity of the scattered light, smaller particles scatter light at higher angles than those of larger particles. Polarisation Intensity Differential Scattering (PIDS) consists of incident light of three different wavelengths in two planes of polarisation and detectors placed at higher angles, up to 150^{o}, allowing for detection of sub-micron particles. A drawback is that this instrument determines particle size based on the Mie theory, which assumes spherical particles. In reality this is often not the case so scanning electron microscopy should also be used to confirm particle size.

3.1.2 Scanning Electron Microscopy (SEM)

Visual examination of the surface or cross section of a cell can be achieved using Scanning Electron Microscopy (SEM). Electrons produced from an electron gun accelerate towards a positively charged, ring anode, a beam of electrons passes through to a magnetic lens which aligns and focuses the beam onto the target of interest. Electrons hitting and interacting

with the target cause electrons and X-rays to be ejected from the surface, some of the electrons are so called back scattered electrons from the SEM electron beam. Other, lower energy electrons are secondary electrons displaced from the target. In secondary electron imaging (SEI) mode the ejected electrons are detected and displayed as an optical image showing the surface of the sample. Backscattered electron imaging mode (BEI) allows the imaging of different phases since the intensity is dependent on the atomic number of the detected atoms. For this study a JEOL 5610 LV SEM in SEI mode was used throughout. In order to ensure electronic conductivity all samples were sputtered with 20 – 30 nm thickness of gold and mounted on a metallic stub with conductive carbon tape prior to imaging.

3.1.3 X-Ray Diffraction (XRD)

X-Ray Diffraction (XRD) is used to analyse the structure of crystalline materials and relies on the similarity of X-ray wavelengths and the atomic spacing of a crystalline lattice. X-rays incident on the material at an angle θ are diffracted according to Braggs law:

$$n\lambda = 2d_{hkl}\sin\theta \qquad \text{Equation 25}$$

Where n is the order of reflection, λ is the wavelength of the X-ray and d_{hkl} is the lattice spacing with *h, k, and l* the Miller indices. Figure 12 shows this principal. The difference in X-Ray path length (A→B→C) when two lattice planes separated by distance d_{hkl} is $2d_{hkl}\sin\theta$. For the reflected waves to constructively interfere this path difference must equal a whole number of the X-ray's wavelength. λ, n and d_{hkl} are constant during a measurement, and θ is varied by moving the incident X-ray and the detector. The unit cell parameters are derived from the 2θ position of the peaks of a diffraction pattern whereas the intensity of the scattered X-rays depends on the structure of the material, therefore a generated diffraction pattern is unique to the material's structure and composition.

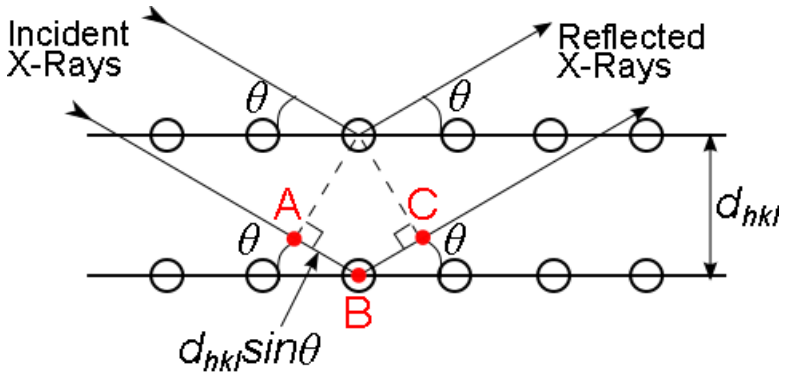

Figure 12. Diagram showing the scattering of X-rays from hkl lattice planes.

The intensity of a diffraction peak, I_{hkl}, gives information about the positions of the atoms in the cell and is proportional to the structure factor, F_{hkl}.

$$I_{hkl} \propto |F_{hkl}|^2 \qquad \text{Equation 26}$$

The structure factor is dependent on the size any given atom and the position within the cell described by fractional coordinates (x, y, z).

$$F_{hkl} = \sum_{j=1}^{atoms} f_i \exp[2\pi i(hx_j + ky_j + lz_j)] \qquad \text{Equation 27}$$

Where f_i is the atomic scattering factor of the i^{th} atom which is proportional to the number of electrons in that atom.

X-rays are generated by directing high energy electrons at a metal target with sufficient energy to displace atomic electrons from low energy levels of the metal. Electrons from outer atomic layers then drop to the unoccupied lower energy level, releasing an X-ray specific to that transition. The metal most frequently used is copper which generates X-rays of three different wavelengths: Cu-$K_{\alpha1}$, Cu-$K_{\alpha2}$ and Cu-K_{β}, a monochromator can be used to filter out the Cu-K_{β} X-rays but is not sufficient to filter out Cu-$K_{\alpha1}$ or Cu-$K_{\alpha2}$ and so diffraction peaks often display two peaks, associated with each Cu-K_{α} wavelength.

In this study XRD data was obtained using XRD PANalytical X'Pert Pro MPD using Ni filtered Cu-K_α radiation (λ = 1.5418 Å) operated at 40 kV and 40 mA. XRD data taken at temperature was obtained using HT-XRD Philips X'Pert MPD with a Buhler HDK 2.4 heating chamber.

The angles and relative intensities supply information about lattice spacing and atomic positions respectively, these can be compared against a database such as the Inorganic Crystal Structure Database (ICSD) from the Chemical Database Service (CDS). For more detailed analysis of an XRD pattern Le Bail fitting or Rietveld refinement is performed. [71]

Since X-rays interact with the electrons in the atom, the positions of the oxygen atoms in the materials of this study cannot be refined due to oxygen's low atomic number. Therefore, for this study, the Le Bail method was deemed a satisfactory refinement method, used to determine lattice parameters from the XRD data. The Le Bail method does not refine structure factors F_{hkl} including atom positions, scattering factors, atomic occupation and thermal factors. Le Bail fitting estimates intensity by refining unit cell parameters, background, peak shape and diffractometer parameters.

The weighted profile, R_{wp}, describes the agreement between the observed and calculated data:

$$R_{wp} = \left(\frac{\sum_i w_i[y_i(obs) - y_i(calc)]^2}{\sum_i w_i[y_i(obs)^2]^{1/2}}\right)^{1/2} \quad \text{Equation 28}$$

where $y_i(obs)$ is the observed intensity and $y_i(calc)$ is the calculated intensity and w_i is the weighting. The statistically expected R value, R_{exp} given by Equation 29:

$$R_{exp} = \left(\frac{(N-P)}{\sum_i^N w_i y_i(obs)^2}\right)^{1/2} \quad \text{Equation 29}$$

where N is the number of observations and P is the number of parameters. The 'goodness of fit' is defined by χ^2:

$$\chi^2 = \left(\frac{R_{wp}}{R_{exp}}\right)^2 \quad \text{Equation 30}$$

R_{wp} values of < 10%, and χ^2 values between 1 < 4 are desired in order to be confident of reasonable fitted data.

3.2 Cell Fabrication

3.2.1 Electrolyte Preparation

Commercial powder $La_{0.8}Sr_{0.2}Ga_{0.8}Mg_{0.2}O_{2.8}$ supplied by Praxair Speciality Ceramics was used throughout this study as the electrolyte material. In this thesis 'LSGM' is assumed to be $La_{0.8}Sr_{0.2}Ga_{0.8}Mg_{0.2}O_{2.8}$ stoichiometry unless otherwise stated. Pellets of LSGM were formed by uniaxial pressing of the powder to 1.5 tonnes followed by isostatic pressing at 300 MPa. These 'green' pellets were then sintered at 1450^{o}C at a heating and cooling rate of 5^{o}C.min^{-1} and held at temperature for two hours to form dense pellets.

The density of the electrolyte ρ_b is determined using Archimedes' Principle and Equation 31.

$$\rho_b = \frac{W(a).\rho_{fl}}{A.(W(a) - W(fl))} + B$$

Equation 31

Where *W(a)* is the weight of the sample dry, *W(fl)* is the weight of the sample when immersed in water, ρ_{fl} is the density of the water, *A* is a correction factor individual to the apparatus and *B* is the density of air at atmospheric pressure.

In order to ensure that any porosity of the sample was fully filled with water, the sample was kept in distilled water under vacuum before measurements of *W(fl)* were taken. The density of the sample is then compared to the theoretical density which is calculated from the unit cell parameters of the material which can be found from XRD data (Section 4.3.1) or literature.

Theoretical density, ρ_T, is found by Equation 32:

$$\rho_T = \frac{m_a.Z}{VN_A}$$

Equation 32

Where m_a is the atomic weight (g.mol^{-1}) of the sample, *Z* is the number of formula units per unit cell, *V* is the unit cell volume and N_A is Avogadro's number. A density of > 95% compared to theoretical is desired to ensure no gas leaks within the system. All electrolyte pellets used in this study displayed such a density.

3.2.2 Ink Preparation and Deposition

Commercial powder $La_2NiO_{4+\delta}$ (LNO) supplied by CerPoTech was used throughout this study as the electrode material. To adhere the electrode material to the dense electrolyte the LNO was processed into an ink. To form the ink the LNO powder was first rough mixed in a pestle and mortar with a commercially sourced, terpineol based, ink vehicle (Fuel Cell Materials Ink Vehicle 311006). The ratio of LNO to ink vehicle used was 2:1 by weight. This mixture was then three-roll milled in an Exakt 80E to ensure greater uniformity of the ink. It was deemed unnecessary to have a preliminary ball milling step (powder ball milled with zirconia balls in ethanol) as the particle size distribution was observed to be optimal without this step (see Section 4.1).

The ink was then deposited on the dense electrolyte pellets by screen printing. The thickness of the applied electrode can be controlled by the number of depositions. After the electrode was deposited on one side of the electrode it was placed in an oven at 100^{o}C to dry before applying the electrode to the second side. Complete pellets were then calcined at 1100^{o}C at a heating and cooling rate of 2.5^{o}C.min^{-1} and held at temperature for two hours to adhere the electrode to the electrolyte surface.

3.3 Electrochemical Impedance Spectroscopy (EIS)

Electrochemical impedance spectroscopy is used to study the electrochemical performance of electrodes and electrolytes and can distinguish different processes occurring within the system. This technique has been extensively used in the study of SOFCs/SOECs, however great care has to be taken when interpreting the results.

Impedance theory can be applied to systems which don't obey Ohm's law. Inducing a small alternating potential produces a small alternating current, the polarization curve can be described as pseudo linear if the perturbation is small, as depicted in Figure 13.

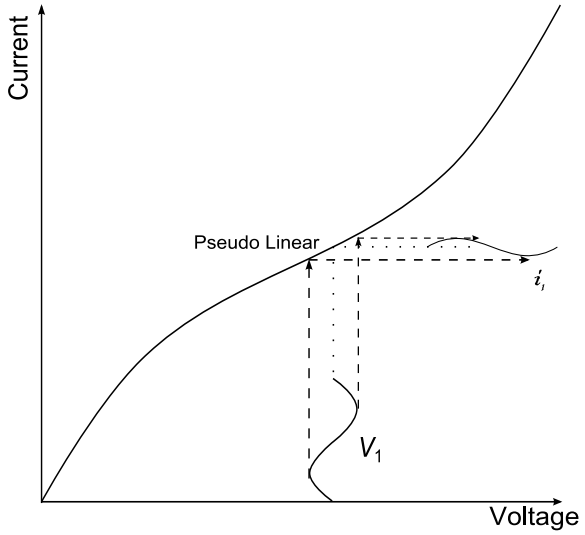

Figure 13. Non ohmic polarization curve showing AC potential input and current response. Supplied potential, V_1, results in current response i_1.

When applying an alternating potential, $V(\omega)$, with amplitude V_o and angular frequency ω (frequency $v = \omega/2\pi$):

$$V(\omega) = V_o e^{j\omega t} \qquad \text{Equation 33}$$

Where $j = \sqrt{-1}$. The resulting current $I(\omega)$ is:

$$I(\omega) = I_o e^{(j\omega t + \varphi)} \qquad \text{Equation 34}$$

Where I_o is the current amplitude and φ is the phase shift ($\varphi = 0$ for a purely resistive element and $\pi/2$ for a purely capacitive element).

Therefore, as impedance $Z(\omega) = V(\omega)/I(\omega)$ and writing $|Z| = V_o/I_o$

$$Z = |Z|.e^{(-j\varphi)} \qquad \text{Equation 35}$$

or

$$Z = |Z|.(\cos\varphi - j.\sin\varphi) \qquad \text{Equation 36}$$

Impedance is therefore a complex number and is often written:

$$Z = Z' - jZ'' \qquad \text{Equation 37}$$

where:

$Z' = |Z|cos\varphi$ Equation 38

$Z'' = |Z|sin\varphi$ Equation 39

Impedance spectroscopy involves applying an alternating potential at a range of frequencies, from MHz to mHz, and recording the subsequent impedances on a Nyquist plot of real impedance, *Z*' against imaginary impedance, *Z*", an example of which is shown in Figure 14.

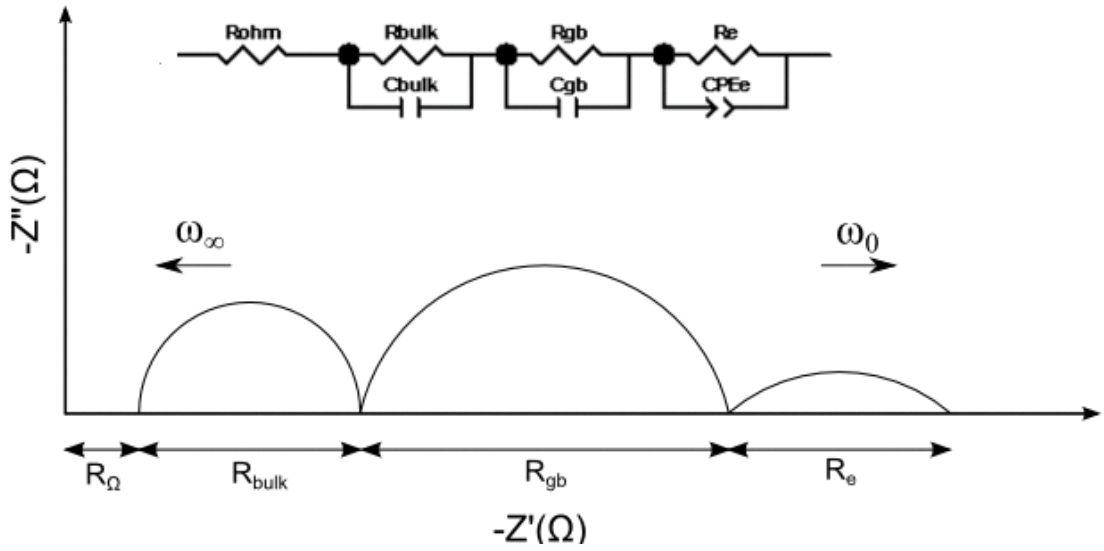

Figure 14. An example Nyquist plot for a solid, oxygen ion conducting electrolyte with conducting electrodes. The equivalent circuit for such a system is displayed above.

On the Nyquist plot characteristic arcs are formed representing responses from different processes of the system. The ability of this technique to separate each process is due to each process possessing a unique relaxation time, the responses therefore occur at different frequencies. A limitation of the Nyquist plot is shown in Figure 14, which is that the frequency is not explicitly plotted along with the Z' and Z" values.

Each semicircle on the plot represents a different component of the system being studied. Curves produced at high frequencies are often attributed to the bulk of the electrolyte,

curves at medium frequencies are associated with the grain boundaries (gb) of the electrolyte and curves at lower frequencies are attributed to processes of the electrode material. However, analysis is often less simplistic as features of the plot can be caused by surface layer effects, interface effects and more. [72]

An equivalent circuit of resistors, capacitors, constant phase elements (CPE) etc. can be created which would result in an identical curve for each component. The simplest equivalent circuit for a single semicircle is an RC circuit, this is a resistor (R) and capacitor (C) connected in parallel. The equivalent circuit of more than one semicircle is then the parallel RC circuit of each component connected in series. However, a number of different equivalent circuits may describe the same plot. Knowledge of the system is therefore required in order to select the circuit which best describes the processes occurring.

The total resistance due to each component can be found from the diameter of the curve on the real axis. Furthermore, the capacitance of each component may be determined from Equation 40.

$$f_{\max} = \frac{\omega_o}{2\pi} = \frac{1}{2\pi RC} \qquad \text{Equation 40}$$

Where, for each component, f_{max} and ω_o are the relaxation frequency and relaxation angular frequency which occur when Z" is maximum, R is the resistance and C the capacitance.

The dielectric relaxation time, or time constant τ is related to R, C and ω_o:

$$\tau = RC = \omega_o^{-1} \qquad \text{Equation 41}$$

Knowing the capacitance of a particular Nyquist curve gives an indication as to what the underlying process is. Irvine et al. [73] state capacitance values with possible phenomenon, and these are shown in Table 3.

Table 3. Summary of capacitance values and their corresponding physical process. Unless otherwise stated information from reference [73].

Capacitance (F)	**Phenomenon Responsible**
10^{-12}	Grain Bulk
10^{-11}	Minor, Second Phase
$10^{-11} – 10^{-8}$	Grain Boundary
$10^{-10} – 10^{-9}$	Bulk Ferroelectric
$10^{-9} – 10^{-7}$	Surface Layer
$10^{-7} – 10^{-5}$	Oxygen Transfer at Sample - Electrode Interface
10^{-4}	Electrochemical Reactions, Charge Transfer
$10^{-4} – 10^{-3}$ [74]	Oxygen Exchange on the Electrode Surface
10^{-3} [45]	Electrochemical reactions on Electrode
$10^{-3} – 10^{-2}$ [51]	Oxygen Diffusion Through Electrode, Charge Transfer at Electrode Surface
10^{-1} [74]	Gas Diffusion to Electrode Surface

Often a constant phase element (CPE) in parallel with a resistor element is more appropriate than a capacitor, this is required when the semicircle is seen to be depressed. Although it is not fully understood why depression occurs it may be due to the surface roughness; regions of two or three phases; and absorbed species causing a non-uniform electric field at the interface. [75]

The capacitance from a CPE is calculated using Equation 42:

$$C = (TR^{1-p})^{1/p}$$

Equation 42

Where T is the pseudo capacitance, R the element's resistance and p is a parameter related to the depression angle of the curve. [21] p is a value between 0 – 1, if $p = 1$ the process has a phase shift of π/2, therefore a pure capacitor. If $p = 0.5$ a 45^{o} line is produced in place of the so far discussed characteristic arc, this implies Warburg diffusion.

As impedance is conducted over a range of temperatures different processes become apparent or disappear from the Nyquist plot with changing temperature. At low temperatures and high frequencies, R_o is the point at which the high frequency impedance response crosses the Z', real, axis and represents the resistance of the equipment wires. For a solid oxide cell, the electrolyte bulk arc is clearly visible at low temperatures, as temperature increases the relaxation frequency increases until it is no longer within measurable range and is seen to 'disappear' into R_o. It is still possible to calculate the bulk resistance so long as the equipment resistances are known and removed from the R_o. As temperature increases further the grain boundary relaxation frequency also becomes too high to measure, at this point it is no longer possible to distinguish the two processes.

Resistivity and conductivity can be calculated from the resistance of each process. If the impedance technique is conducted over a range of temperatures an Arrhenius plot can be drawn. This is based on the Arrhenius equation:

$$\sigma = \sigma_o . e^{E_a / R_g T}$$

Equation 43

Where E_a is the activation energy, T is the absolute temperature, R_g is the gas constant, σ_o is a pre-exponential constant which derives from a number of constants such as the vibrating frequency of the moving ions. [76] σ is the conductivity = $\left(\frac{l}{R.A}\right)$ where R is resistance, l the thickness of the cell and A is the cross sectional area of the cell. Rearranging Equation 43 and plotting as an Arrhenius plot of log σ against T^{-1} allows the activation energy of each process to be calculated from the gradient of the subsequent straight line.

Area specific resistance is often used as a measure of electrode performance. The ASR of an electrode of a symmetrical cell is given by the following equation:

$$ASR = \frac{R_P . A}{2}$$

Equation 44

Where R_P is the polarization resistance, or resistance of the electrode as worked out from the Nyquist plot, A is the surface area of the cell and the factor of 2 is for symmetrical cells and so gives the ASR of one electrode only. In some cases it is appropriate to state the ASR

of the entire cell configuration; in this case ASR is equal to the total cell resistance multiplied by the surface area.

As with the conductivity, it is possible to find the activation energy using the resistance in the Arrhenius equation:

$$ASR = R_P . e^{E_a / R_g T}$$ Equation 45

3.3.1 EIS Experimental Instrumentation and Conditions

Electrochemical impedance spectroscopy measurements were performed using Solartron Analytical ModuLab frequency response analyser (FRA) over the frequency range 1MHz – 0.01Hz, with an applied potential amplitude of 50 mV and over the temperature range 300 – 800^{o}C, in a range of pO_2 atmospheres. The pellets were mounted in a ProboStat^{TM} sample holder in two and three electrode configurations as described in Figure 15.

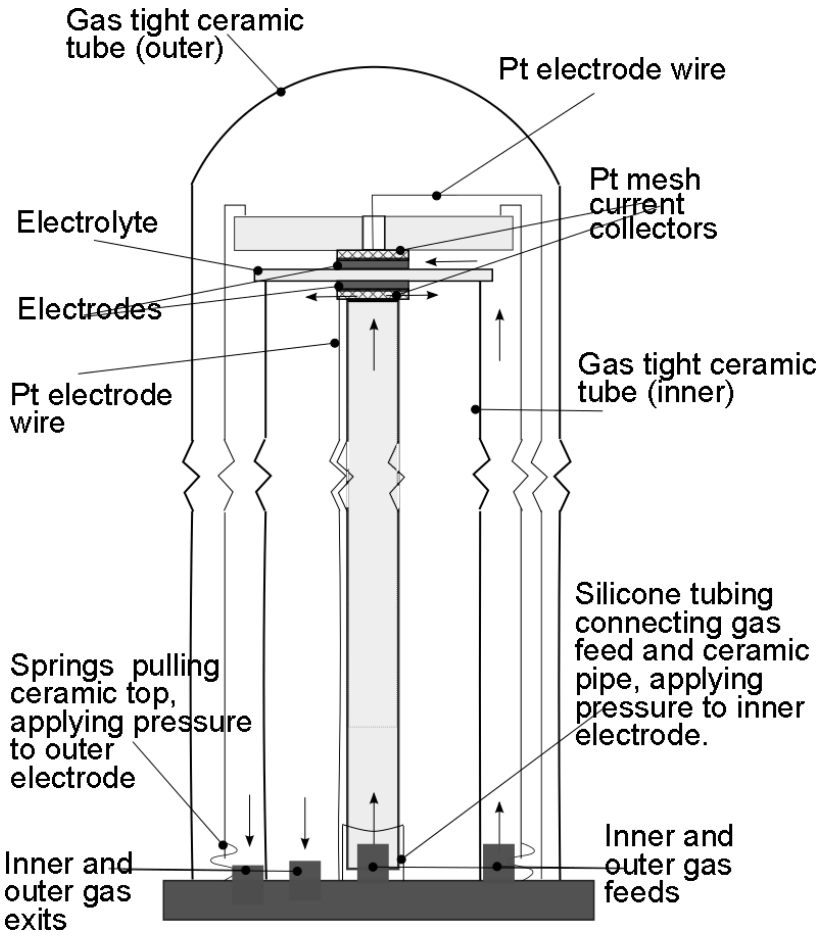

Figure 15. Impedance sample holder and gas inlet and outlet for measuring EIS under a range of pO_2 atmospheres.

pO_2 was varied by conducting the experiment in ambient atmosphere and by supplying pure O_2 or N_2 to the gas feeds for high or low pO_2 atmospheres respectively. The pO_2 was measured using Systech Instruments ZR893 Oxygen Analyser and the rate of flow was controlled using Aalborg gas flow controllers. The mixed gas was fed to the 'inner' and 'outer' gas feeds to ensure identical atmospheres on both sides of the cell.

Electrical measurements were made by platinum wires and platinum mesh for the symmetrical cell electrode current collectors. Platinum paint was applied in a ring configuration to the pellets, and sintered at 900^{o}C for two hours to create a reference electrode which was connected via a platinum ring wire. The reference electrode configuration is discussed in more detail in Section 3.4.

In order to determine the effect of steam on electrode performance an in-house impedance rig was created, the set-up of which is depicted in Figure 16. EIS measurements were performed using a Solartron 1260 FRA over the frequency range 13MHz – 0.01Hz and temperature range 300 – 800^{o}C. Electrical measurements were made by platinum wires and platinum mesh for the symmetrical cell electrode current collectors.

Measurements were taken in 'humid' air by flowing dry air through a water bath at ambient temperature upstream of the sample holder. To measure EIS in 'dry' air the water bath was removed and the dry air allowed to flow directly to the sample holder. For both humid and dry experiments a Sensirion SHT 75 complementary metal oxide semiconductor (CMOS) type humidity sensor was used to measure the humidity and the rate of flow was controlled using Aalborg gas flow controllers.

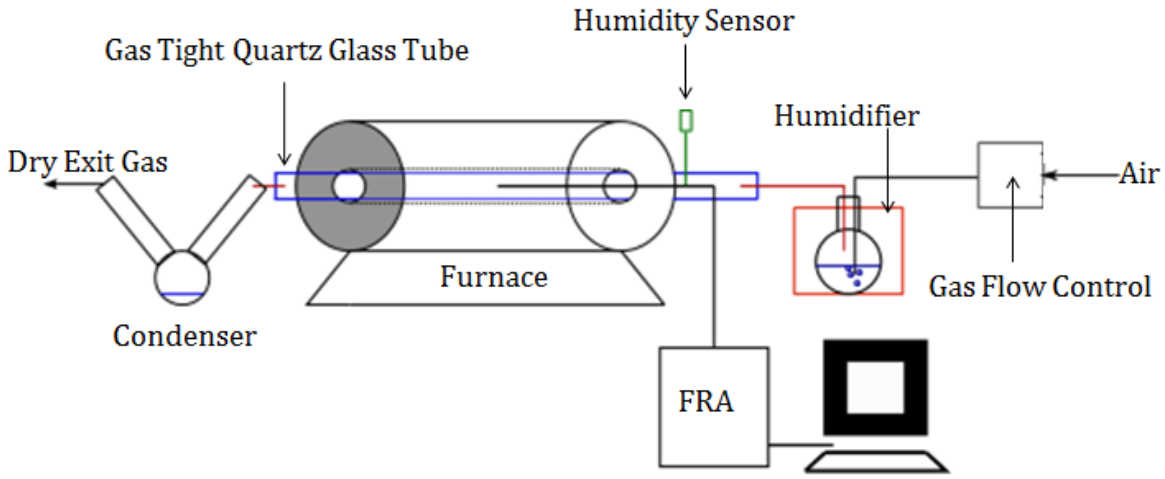

Figure 16. Gas flow for 'dry' and 'humid' EIS, inlet gas flows from right to left in this figure. FRA: Frequency Response Analyser.

Due to size restrictions of the set-up depicted in Figure 16 it was not possible to include three electrode tests under humid atmosphere and so a symmetrical, two electrode, configuration was used for the varying pH_2O experiments.

For all EIS experiments the data was modelled using Scribner Associates' ZView v 3.2c. Error values are automatically calculated by the software and are given by a ±'error' which are

directly stated for capacitance and resistance values or used for the calculation of error of constant phase elements (CPEs).

Example data from the equipment used in this study are displayed in Figure 17 and show a 'jump' in the high frequency arc. This jump occurs at frequency *v* = 1MHz when the frequency response analyser, FRA, changes from high (> 1MHz) to low (< 1 MHz) frequency, in such a case fitting of the arc is problematic. However in this study the 'jump' is only apparent in the electrolyte bulk response at low temperatures, for fitting purposes only the data lower than 1MHz was fitted with the ZView software.

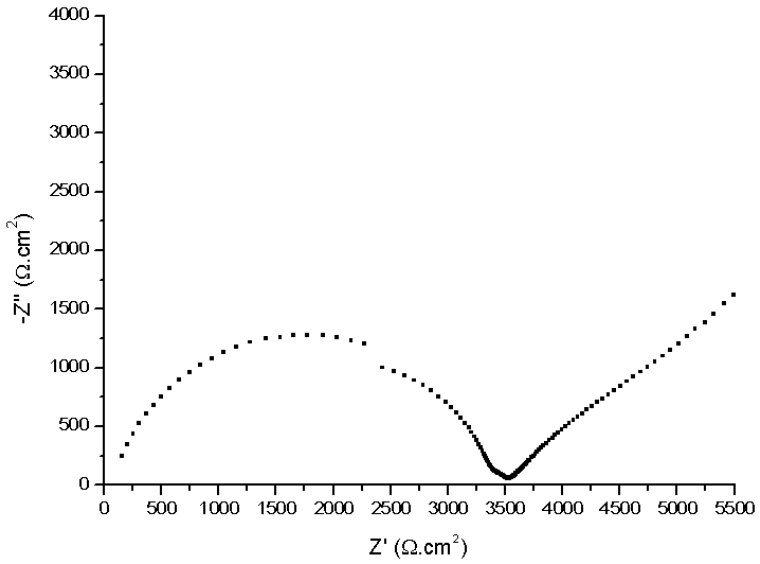

Figure 17. Example impedance data using Solartron 1260 FRA displaying a 'jump' in data points at *v* = 1MHz.

3.4 Reference Electrode

A reference electrode is required to determine the responses of one electrode only. This is required when a non-symmetrical cell is used, i.e. having different electrode materials for the anode and cathode; changing the atmospheres of one or both cathodes; and when applying a potential bias. A reference electrode, RE, is a third electrode added to the standard two electrode system. Placed in a region of stable potential the RE measures the

potential change of the working electrode, WE, due to any change in the current passed through the working and counter electrodes. In the literature there are a number of three electrode configurations, as depicted in Figure 18.

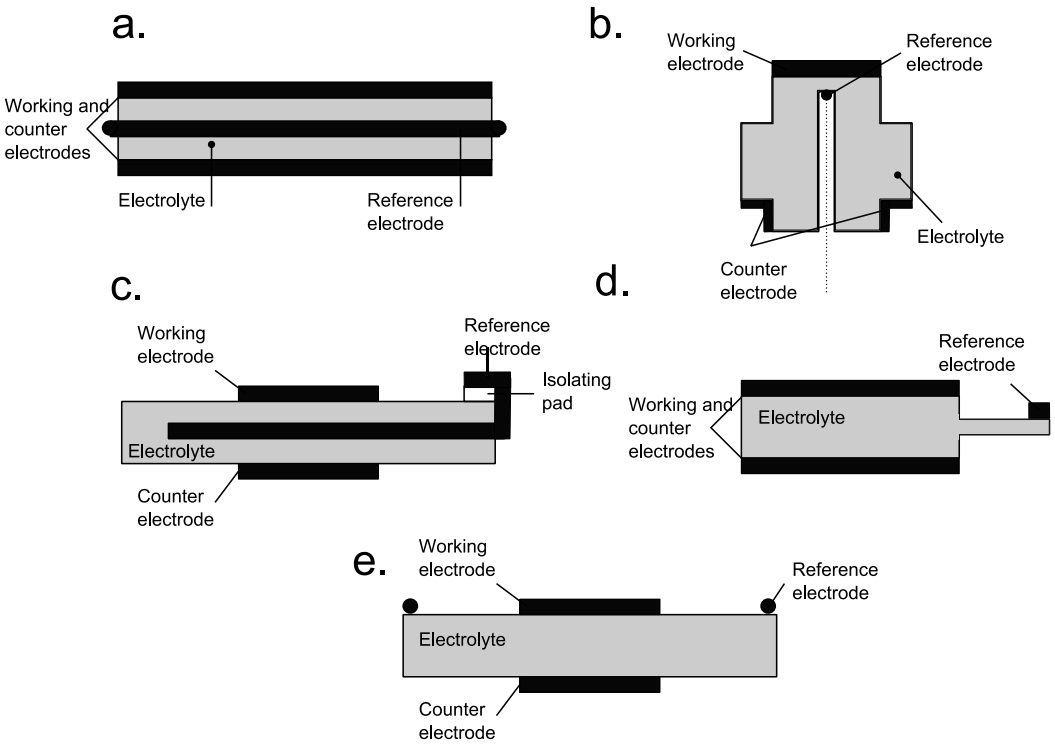

Figure 18. Reference electrode configurations. a: Reference electrode placed around the edge of a cylindrical electrolyte. b: Reference electrode placed in a well cut into the electrolyte. c: Reference electrode sandwiched inside the electrolyte. d: Reference electrode placed on an arm away from the cell, and e: Reference electrode placed as a ring around the circular working electrode.

Configuration a in Figure 18 enables a uniform current density within the system but the thickness of the electrolyte must be enough to accommodate the reference wire which must be accurately placed. The Luggin-type configuration shown in Figure 18b also ensures uniform current density. This setup is preferred by O. A. Marina et al. [41] due to accuracy, however the drawback of this arrangement is that it is an unusual design compared to conventional SOFCs/SOECs and the electrolyte must be thick in which case wrapping the reference around the electrolyte may be more suitable. Another method is to embed the

reference electrode in the electrolyte as described in configuration c, the Pt reference electrode is much narrower than the thickness of the electrolyte and so causes little disruption to the current density, however re-use of the reference electrode is difficult. Configuration d also has reduced effect on the current density but is awkward to manufacture and potentially fragile. Configuration e is commonly used for three electrode measurements and has been adopted for this study due to its ease of fabrication and use. This configuration is seen in more detail in Figure 19.

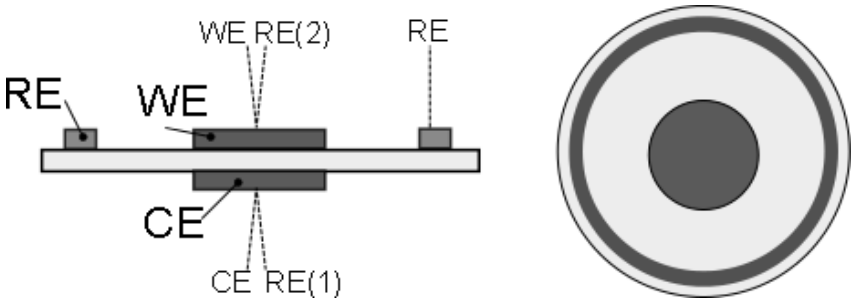

Figure 19. a: Planar view of SOEC/SOFC cell. Dotted lines represent the external electrical connections. Symmetrical cell tests require the connection of RE(1) and RE(2) to the CE and WE respectively. Connecting the reference to RE rather than RE(1) allows electrochemical study of the WE and half of the electrolyte only. b: View of the SOEC/SOFC from above showing the ring reference electrode placement.

The use of a third electrode (RE) allows the measurement of the working electrode and half the electrolyte response. In order to assume equipotential potential between the working electrode (WE) and the counter electrode (CE), the reference electrode (RE) must be placed at least three electrolyte thicknesses away from the WE. [77] If the electrodes of this set-up are not perfectly aligned the current density through the electrolyte is disrupted as shown in Figure 20.

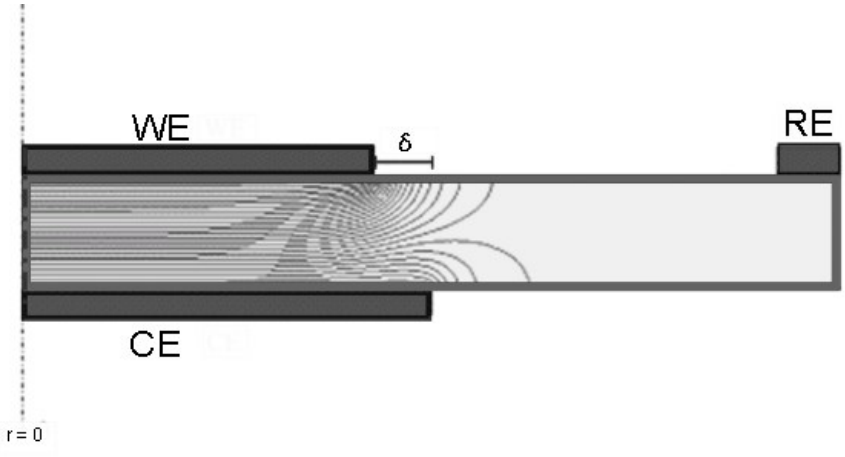

Figure 20. Cross section of a cylindrical cell. δ: the misalignment between two electrodes. The lines within the electrolyte represent lines of equal potential, distorted by electrode misalignment. Image adapted from reference [78]

As can be seen from Figure 20 misplacement of the electrodes may lead to error in the potential measured at the reference electrode. However Rutman et al. [78] determine that, to first approximation, this error would be averaged out by an equal but opposite error on the opposite side of the electrode, assuming that the electrodes are identical in shape and size. Therefore error in misalignment can be avoided if a ring electrode is placed at least three electrolyte thicknesses away from a circular electrode. This configuration viewed from the side and from above is shown in Figure 19.

However, even with correct RE placement, errors may arise if the difference in the impedances of the WE and CE are large. Errors also occur due to changing from primary current distribution to secondary current distribution, definitions below. [77]

Primary current distribution: The potential is uniform and the current density is non-uniform within the electrolyte beyond the double layer. This occurs when the electrolyte has much higher overpotential than the electrode or during the high frequency range of EIS measurements at open circuit.

Secondary current distribution: The potential is non-uniform and the current density is uniform within the electrolyte beyond the double layer. This occurs when the electrode as

well as the electrolyte dictate the current density or during the low frequency range of EIS measurements at open circuit.

Changing from primary to secondary current distribution, or from high frequency to low frequency regime during EIS, changes the potential distribution within the electrolyte. Misaligned electrodes on thin cells result in greater errors than on thick cells as the misalignment distance δ is proportionally more significant compared to the thickness of the cell. [79] Subjecting the cell to load can also result in an error of the potential measured by the RE. This is observed by a shifting of the high frequency intercept on the impedance plot when bias is applied to the cell during EIS.

3.5 Applied DC Potential Bias

In order to mimic Electrolysis and Fuel cell operation an external potential bias is applied during EIS. Potential bias was applied using the Pobostat set-up with Solartron Analytical ModuLab. Biases of ±200mV, ±500mV and ±1000mV were applied, ±1000mV being the maximum the instrument would allow. By definition positive bias is the flow of external current to the working electrode and therefore the supply of external electrons is to the counter electrode, making the working electrode the anode. In negative bias the current flows in the opposite direction, external electrons supplied to the working electrode making it the cathode.

Chapter 4 – Characterisation of Test Materials

The materials used in this study were characterised by particle size analysis and X-ray diffraction to ensure optimal particle size distribution and phase purity.

4.1 Particle Size Analysis

For electrode use a small particle size and small particle size distribution is desired in order to provide large surface area on which electrolysis or fuel cell reactions can occur. In order to determine the optimal amount of time to ball mill the LNO powder before use as electrode material, particle size analysis was conducted on LNO powder that had undergone different ball milling times. The resultant data is displayed in Figure 21.

Figure 21a shows that the powder received displayed the lowest particle size and particle size distribution compared to powder subsequently milled for any amount of time. Ball milling caused agglomeration of this powder. Ball milling for 12 – 16 hours reduces the particle size distribution but not back to the starting level of the received powder; increasing time above 20 hours again increases particle size distribution. For the LNO commercial powder it was therefore not necessary to ball mill the powder before it was prepared into an ink.

a.

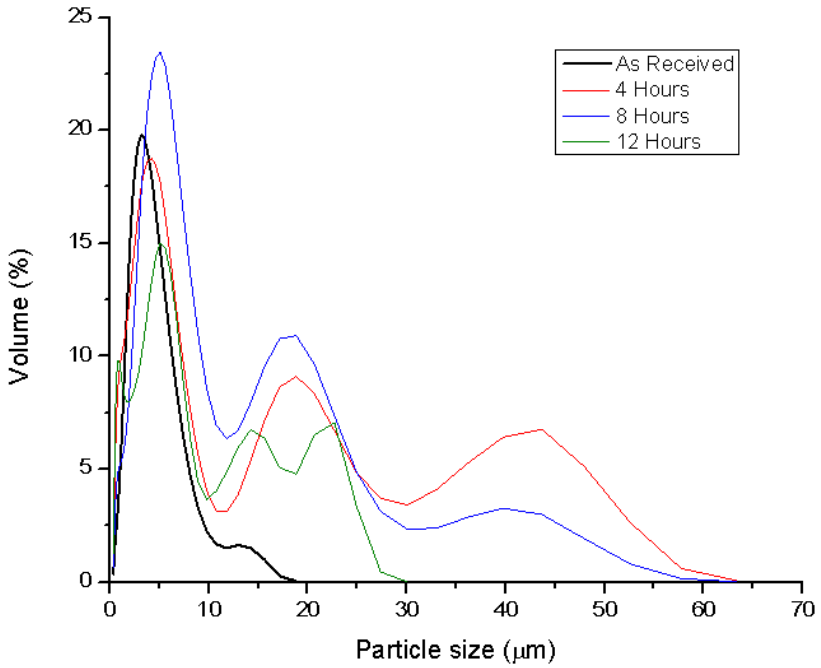

b.

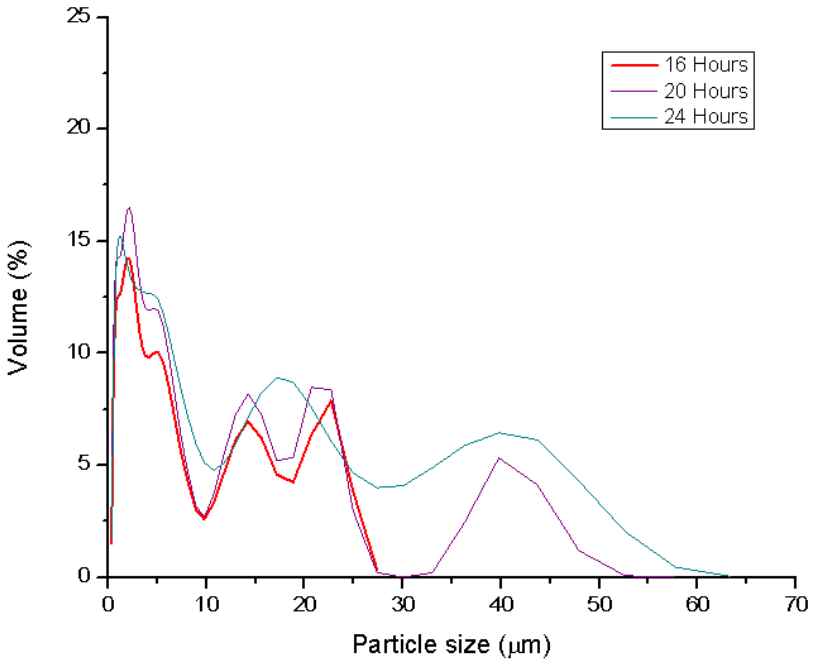

Figure 21. Particle size analysis of LNO powder after ball milled for a: 0, 4, 8 and 12 hours and b: 16, 20 and 24 hours.

As discussed in Section 3.1.1 the particle size analysis technique assumes spherical particles and greater error is introduced if the particles deviate from this shape. For this reason scanning electron microscopy was used as another method to determine the particle size. An SEM image for 'as received' LNO powder is displayed in Figure 22 in which agglomerates of the order of 5 -10 µm are seen.

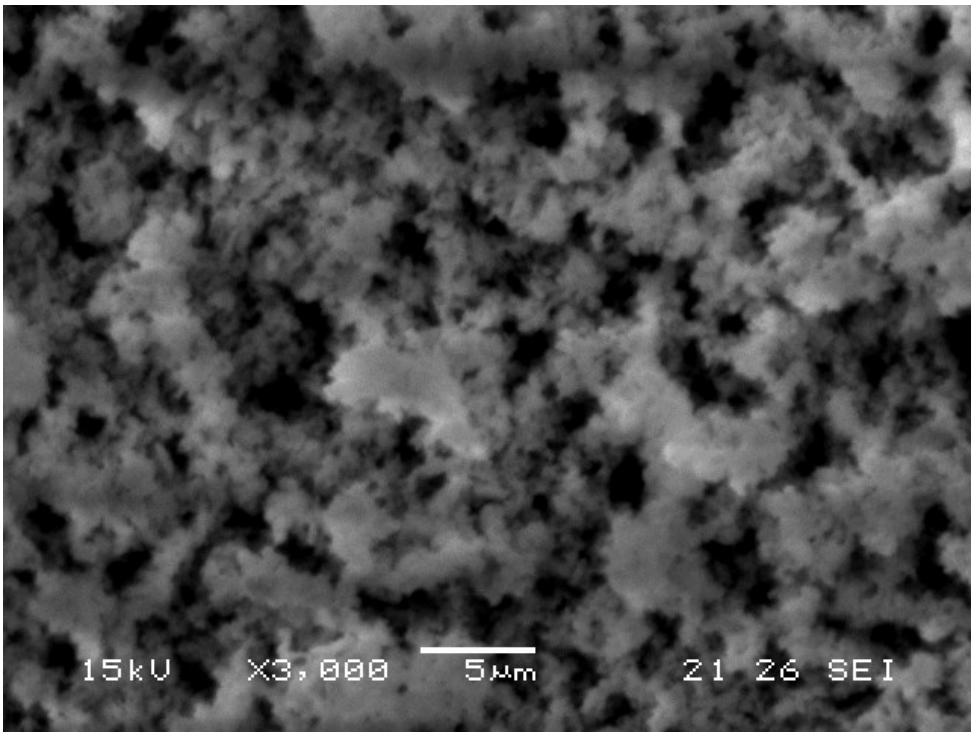

Figure 22. SEM image of commercial LNO powder as received showing particle sizes smaller than 5µm and some agglomeration greater than 5 µm.

4.2 XRD of Commercial Powders

In order to determine the phase purity of the commercial powders LSGM and LNO, the powders were analysed with X-Ray diffraction (XRD) and refined with Le Bail fitting.

4.2.1 LSGM

Figure 23 displays the diffraction pattern of LSGM pellet (preparation method discussed in Section 3.2.1); Le Bail refinement is also displayed.

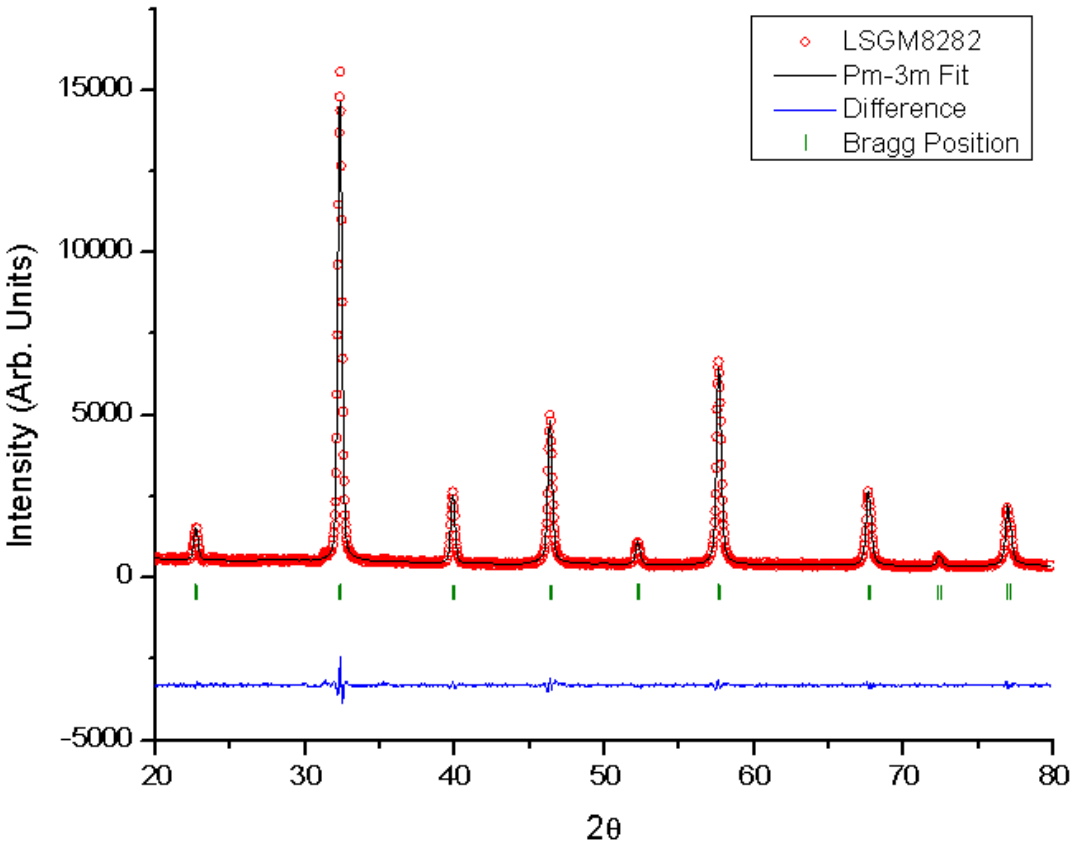

Figure 23. The observed (red symbols) and calculated (black line) diffraction patterns with difference plot (blue line) and the phase markers for Le Bail refinement of LSGM pellet at ambient temperature.

Figure 23 shows LSGM powder of single phase. Le Bail fitting of the XRD pattern for LSGM with space group Pm-3m returns 'goodness of fit' values of R_{wp} 8.61% and χ^2 = 1.83. Lattice parameter = 3.9160(2) Å.

Literature also presents $La_{0.9}S_{0.1}G_{0.8}M_{0.2}O_{2.85}$, LSGM(9182), with the space groups of orthorhombic Imma, [80] and monoclinic I12/a1 [81] at room temperature. However for these structures extra peaks would be visible in the XRD data, for example at ~2θ = 50.8^o and 71.2^o which are not present in Figure 23. As the sample in this study is a processed LSGM pellet having undergone sintering at 1450^{o}C it is reasonable to expect cubic Pm-3m structure.

4.2.2 LNO

Commercial LNO powder was also analysed with Le Bail refinement. An example XRD pattern of LNO powder in ambient conditions with Le Bail fit is shown in Figure 24. Figure 24 assumes space group Fmmm however, as discussed in Section 2.2.3, this material has been reported to display space groups Fmmm, Bmab at room temperature and I4/mmm and F4/mmm at high temperature. For this reason the XRD pattern was fitted assuming each of these space groups, the unit cell parameters and 'goodness of fit' values for these fittings are listed in Table 4.

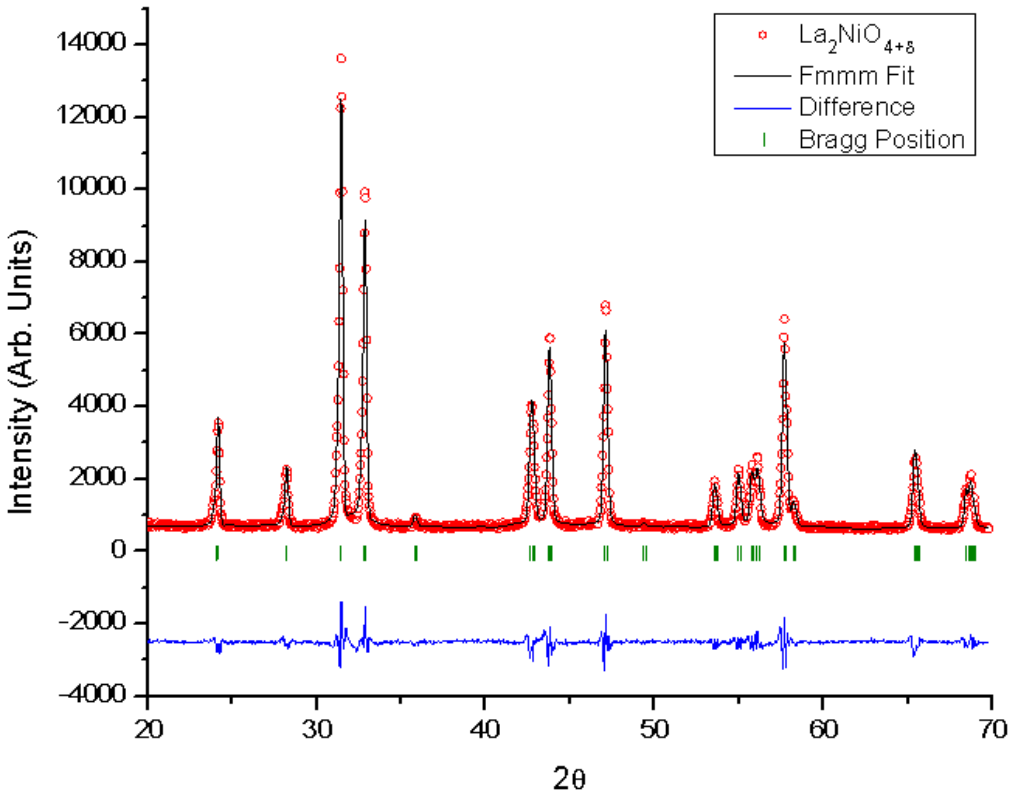

Figure 24. The observed (red symbols) and calculated (black line) diffraction patterns with difference plot (blue line) and the phase markers for Le Bail refinement of $La_2NiO_{4+\delta}$ at ambient temperature.

Table 4. LNO unit cell parameters, R_{wp}, and χ^2 values from Le Bail refinement of LNO at room temperature assuming various space groups.

Space Group	**'a' Lattice Parameter**	**'b' Lattice Parameter**	**'c' Lattice Parameter**	**R_{wp} (%)**	**χ^2**
Fmmm	5.458(2)	5.455(4)	12.668(6)	7.19	5.47
Bmab	5.457(1)	5.453(6)	12.667(5)	7.07	5.27
I4/mmm	3.8592(9)	-	12.6697(3)	7.23	5.51
F4/mmm	5.458(2)	-	12.670(6)	7.23	5.52

Table 4 shows very little difference in the goodness of fit values irrespective of which space group is applied. The space group of LNO is dependent on the position of the oxygen atoms in the lattice. XRD patterns are generated by the interaction of the incident X-rays with the

electrons, the intensity of the scattering is proportional to the number of electrons in an atom. Light elements such as oxygen are therefore difficult to determine in XRD data.

It is shown in literature that Fmmm or Bmab is expected for LNO at room temperature. [39] [18] [54] In this study the space group with the highest symmetry, Fmmm, is attributed for this material at room temperature although more detailed analysis with techniques such as neutron diffraction would be required in order to assign a definitive structure.

4.5 Chapter Summary

The phase purity and structure of LSGM and LNO has been investigated with X-ray diffraction (XRD) and refined with Le Bail fitting. Good phase purity was seen for both materials at room temperature in ambient atmosphere with no additional reflection peaks observed.

The diffraction pattern of LSGM pellet was successfully fitted with the cubic Pm-3m structure.

From literature four possible structures were presented for LNO but it wasn't possible to determine a definitive structure with XRD. At room temperature and ambient atmosphere an orthorhombic structure is assumed, the simplest, Fmmm, structure is chosen to represent the LNO of this study under ambient conditions, however it is noted that more powerful techniques are available to probe this structure further, namely neutron diffraction.

Chapter 5 – Compatibility of LNO with LSGM

To determine the reactivity of the two materials LNO and LSGM a mixture of 1:1 by weight of each material was mixed by pestle and mortar and analysed by in-situ XRD in a range of temperatures and atmospheres.

The following XRD spectra were collected by The Rose Noelle Vannier Group, National Graduate School of Engineering Chemistry of Lille, using D8 Bruker AXS diffractometer equipped with a LynxEye detector and an Antonn Paar, XRK900 high temperature chamber, Cu-K_α radiation. Spectra were taken every 50^{o}C from ambient temperature to 800^{o}C with a heating rate of 0.2^{o}C/s. The sample was deposited on a gold sheet and a fresh sample was used for each experiment. Le Bail fit and analysis was conducted by the author using FullProf Suite Program (2.05) software.

5.1 In-Situ Temperature XRD in Ambient Air

An example XRD pattern of the 1:1 LSGM/LNO sample in dry air at 100^{o}C is shown in Figure 25. Table 5 lists the unit cell parameters of both phases along with the goodness of fit values determined by the Le Bail method.

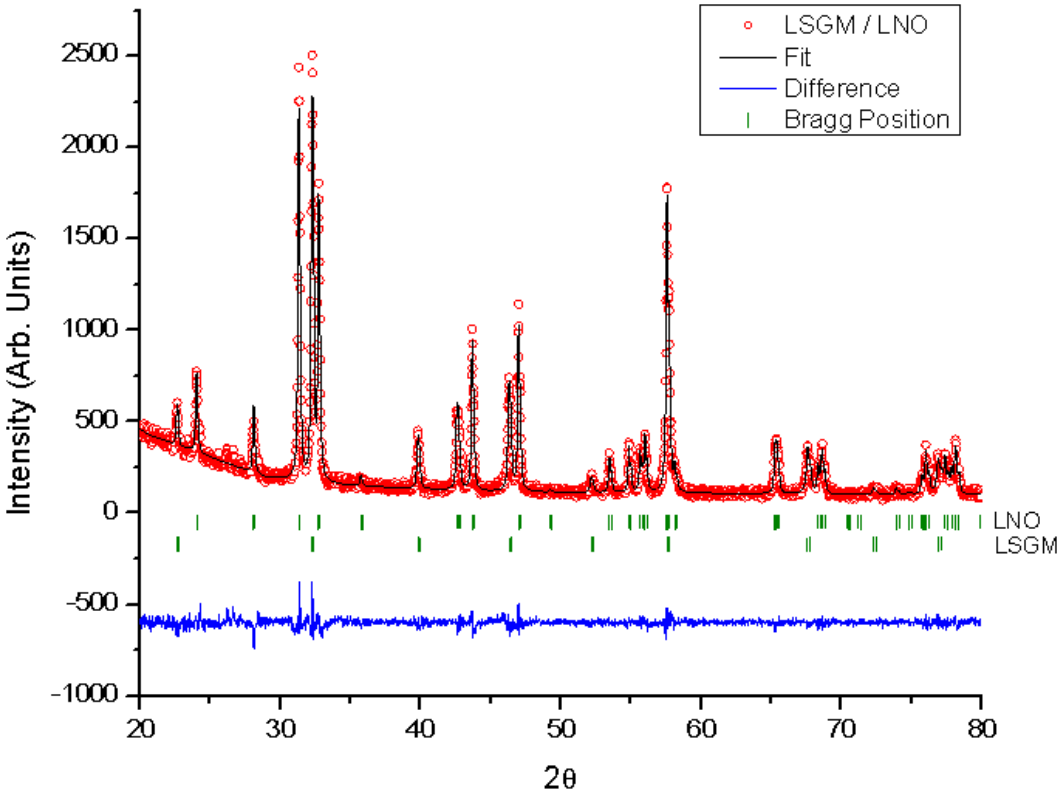

Figure 25. The observed (red symbols) and calculated (black line) diffraction patterns with difference plot (blue line) and the phase markers for Le Bail refinement of 1:1 LSGM/LNO in dry air at 100°C.

Table 5. Unit cell parameters, R_{wp}, and χ^2 values from Le Bail refinement of LSGM/LNO mix at 100°C.

Phase	**'a' Lattice Parameter**	**'b' Lattice Parameter**	**'c' Lattice Parameter**	**R_{wp} (%)**	**χ^2**
LSGM (Pm-3m)	3.9167(1)	-	-	7.77	1.55
LNO (Fmmm)	5.4656(3)	5.4633(3)	12.6854(4)		

In Figure 25 a peak is visible at 2θ ~26.5° that is not attributed to the LSGM or LNO structure and as such is not fitted by the LSGM/LNO model. Indeed this peak is shown to vary with temperature as shown in Figure 26.

a.

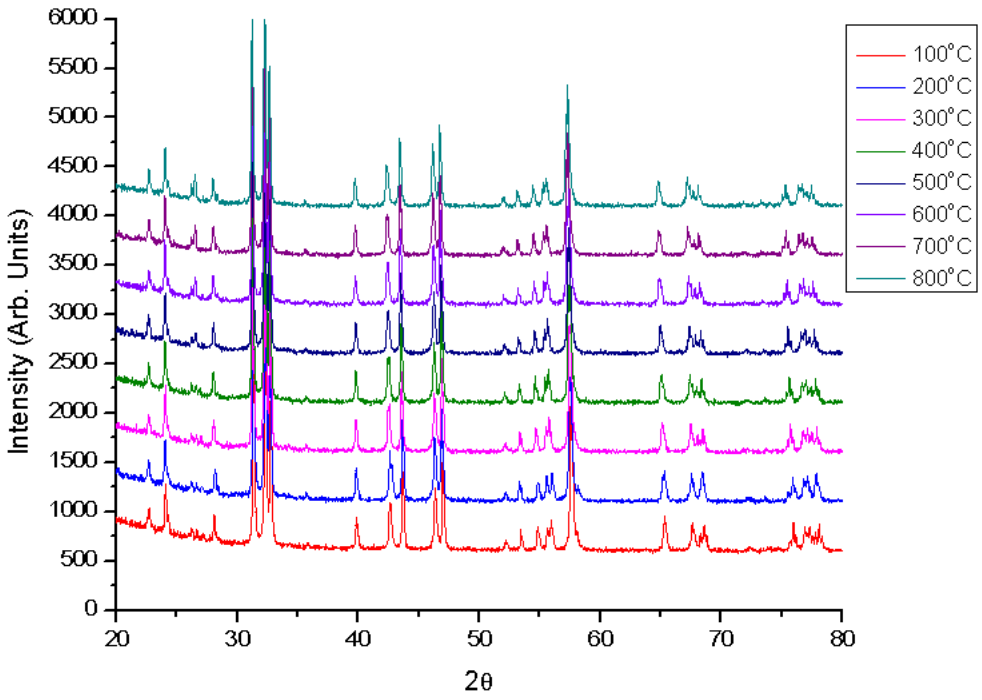

b.

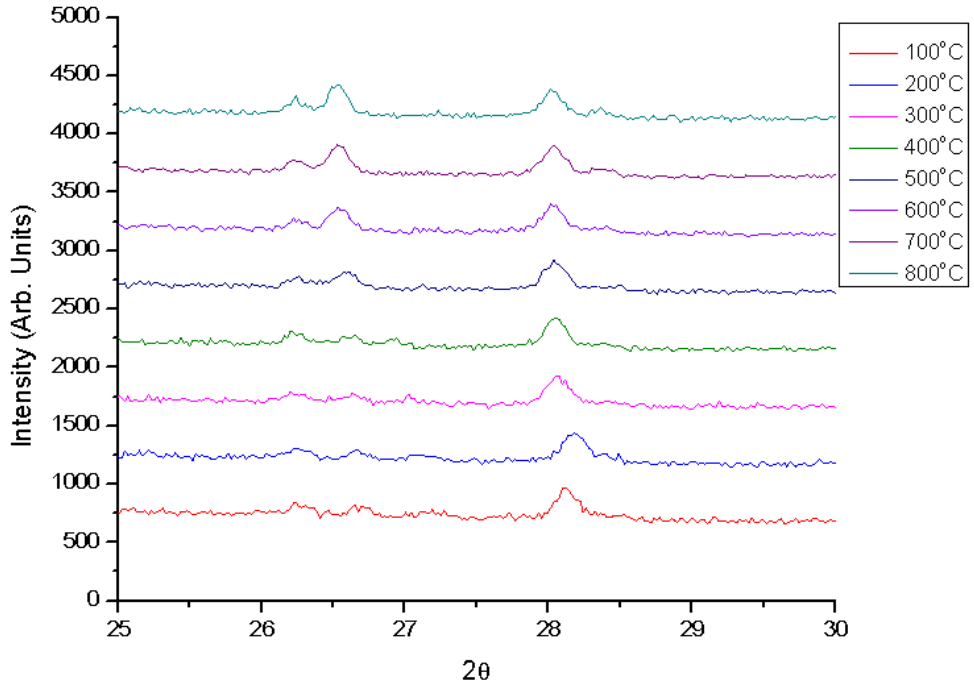

Figure 26. The observed diffraction patterns of 1:1 LSGM/LNO in dry air in the temperature range 100-800°C. a: 2θ range 20-80°, b: expanded view of extra phase peak development with increasing temperature.

Figure 26b displays the increase of the extra peak as temperature increases. As mentioned in Section 2.1.3 reaction species and inter-diffusion of species has been observed at high temperature for LSGM and electrode materials, however in this study La_2O_3, NiO, SrO, Ga_2O_3 and MgO were all discounted as the source of this peak due to inconsistent diffraction patterns. According to Jones et al. [82] a strong XRD peak is displayed at 2θ ~26° for Au_2O_3. As the LNO/LSGM powder was deposited on gold sheet for this experiment this may well be the source of the peak. The diffraction pattern of Au_2O_3 includes another strong peak at 2θ ~32° which is not seen in this data (Figure 27) although the strong LNO/LSGM diffraction peaks at this angle may be obscuring an Au_2O_3 peak.

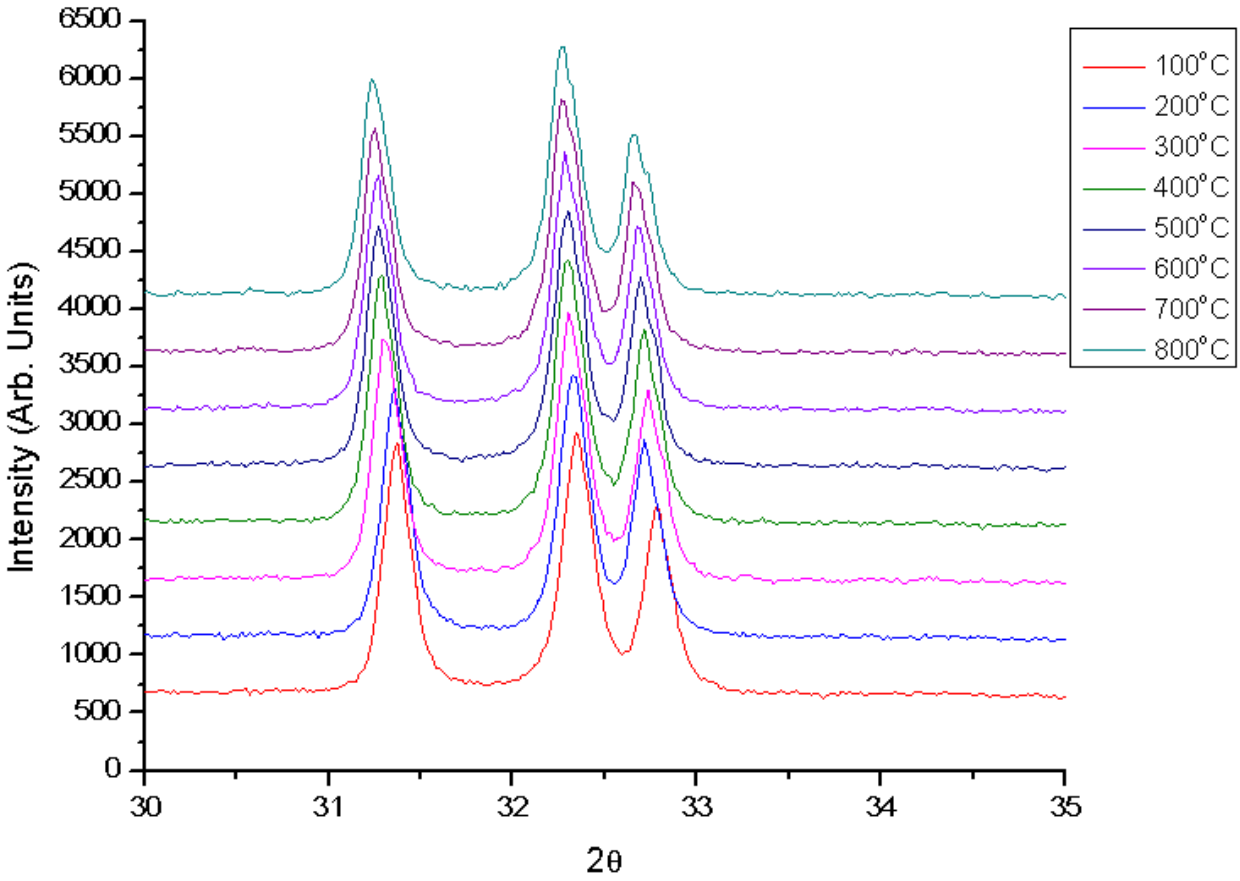

Figure 27. The observed diffraction patterns with of 1:1 LSGM/LNO in dry air in the temperature range 100-800°C. 2θ range 30-35°.

Another explanation for the 2θ ~26.5° may be the formation of higher order LNO Ruddlesden-Popper (RP) phases. Sayers [21] observed the formation of RP phases $La_3Ni_2O_{7-\delta}$ and $La_4Ni_3O_{10-\delta}$ above 800°C during in-situ XRD, catalysed by a platinum substrate however neither of these phases caused a peak at 2θ ~26.5°. The additional peak in this study is also observed at lower temperatures than 800°C. Literature presents the formation of higher order Ruddlesden-Popper phases when LNO is paired with CGO [21] [64] and no such reactions are observed for LNO with LSGM in air. [65] For this reason the additional peak is attributed to Au_2O_3 diffraction from the gold sheet the LNO/LSGM powder was deposited on. In order to determine reactivity in a wider range of atmospheres, in-situ XRD data on LNO/LSGM mixes have been collected in various atmospheres and are presented in subsequent sections.

Figure 28 displays the change of unit cell volume of the LSGM phase in the LNO/LSGM mix in air as temperature is increased. The two sets of data represent the calculated unit volume for LSGM when the model uses Fmmm (red) or I4/mmm (black) as the space group for the LNO phase.

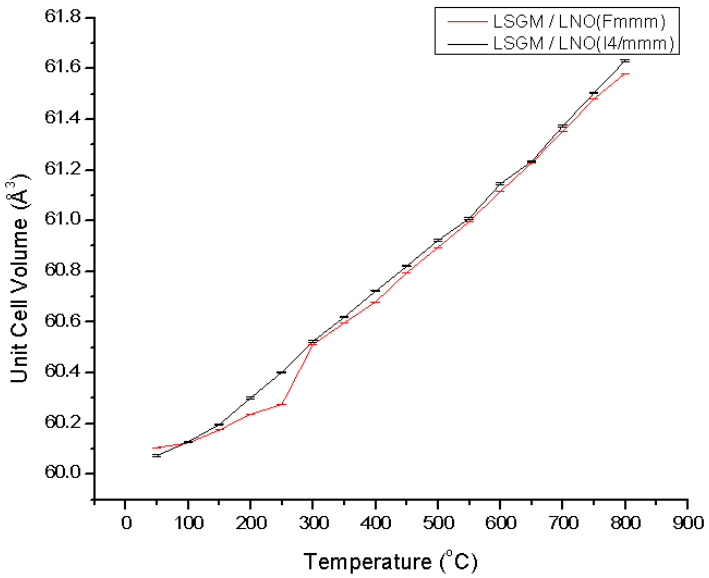

Figure 28. Unit cell volume of LSGM, from mixed LSGM/LNO powder, as refined by Le Bail fitting when assuming LNO space group: Fmmm (black line) and I4/mmm (red line). Note error bars are shown.

The assumed space group of the LNO phase has an effect on the unit parameters fitted for the LSGM phase. When the space group I4/mmm is assumed for the LNO phase, the unit cell volume of the LSGM phase is seen to increase linearly with increasing temperature. However if the space group Fmmm is assumed for the LNO phase, the unit cell volume of the LSGM phase is seen to deviate from linearity from 50 – 300°C possibly implying that Fmmm is not the correct structure for LNO in this temperature range.

Figure 29 displays the change of LNO 'a' and 'b' unit cell parameters with increasing temperature depending on the assumption of Fmmm (Figure 29a) or I4/mmm (Figure 29b) space group. It is clear that irrespective of space group the a/b unit cell parameters increase with temperature with deviation from linearity in the temperature range 200 – 400°C. Figure 30 shows the change of LNO 'c' unit cell parameter with increasing temperature depending on the assumption of Fmmm or I4/mmm space group. The 'c' unit cell parameter also displays deviation from linearity, apparently compensating for that of 'a' and 'b'.

a. **b.**

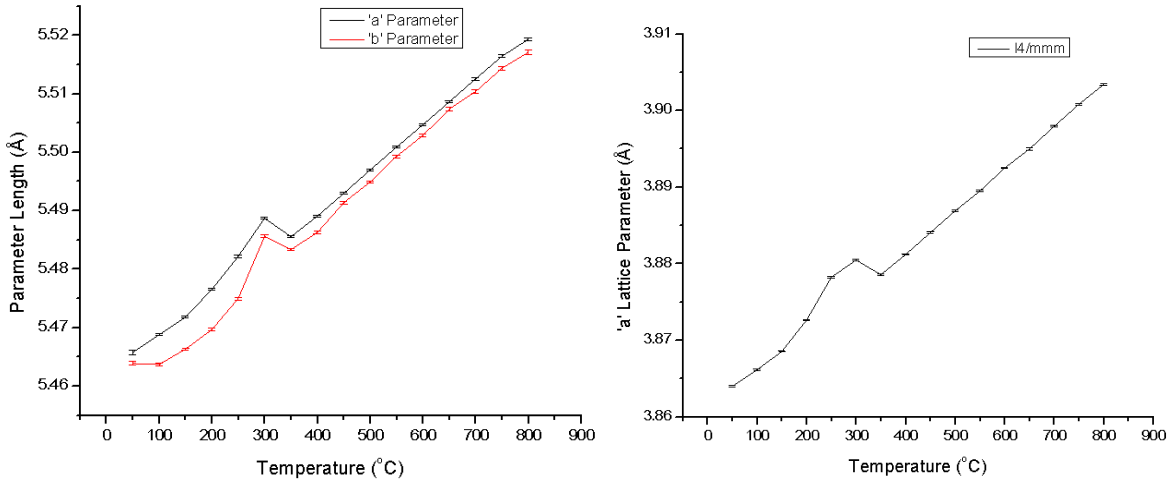

Figure 29. Change of unit cell parameters with temperature a: LNO fitted as Fmmm, 'a' parameter (black) and 'b' parameter (red). b: LNO fitted as I4/mmm, 'a' parameter. Note error bars are shown.

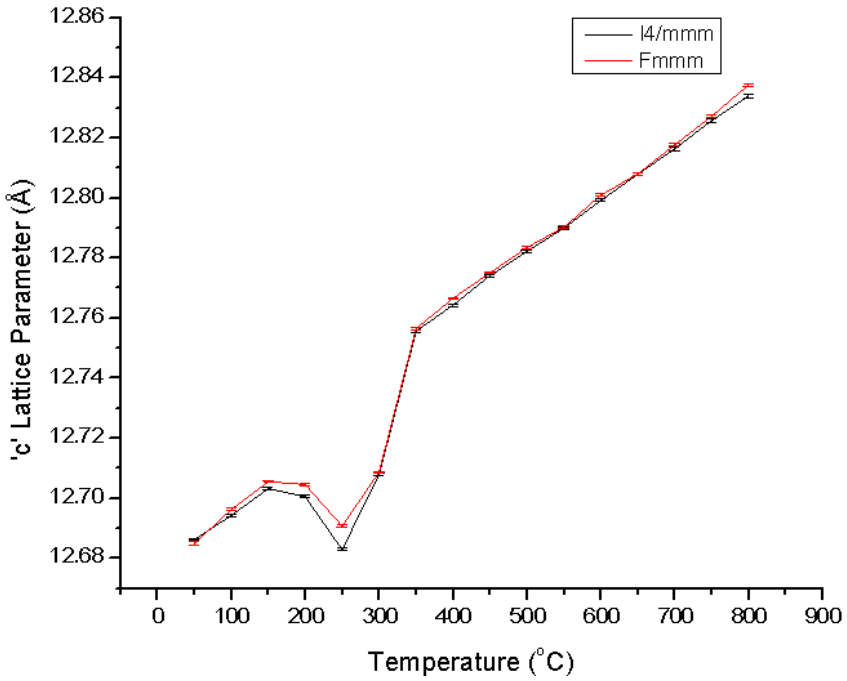

Figure 30. Change of LNO unit cell parameter 'c' with temperature assuming Fmmm (red) or I4/mmm (black) space group. Note error bars are shown.

Figure 31 displays the calculated LNO unit cell volume with increasing temperature, fitted assuming Fmmm space group (Figure 31a) and I4/mmm space group (Figure 31b). When I4/mmm space group is assumed for the LNO phase, the 'c' parameter almost entirely compensates for the deviation in linearity of the 'a' parameter. This is not the case when Fmmm is assumed, deviation from linearity is noted for the unit cell volume at 250°C. Skinner [83] found by neutron diffraction that LNO displays linear increase in cell volume with increasing temperature despite non-linearity of bond lengths and other unit cell parameters with temperature. It was also noted that the structural transformation from orthorhombic to tetragonal occurs in the temperature regime of room temperature – 150°C and pure I4/mmm up to 800°C. For these reasons, this study assumes the space group I4/mmm for the LNO phase above 100°C.

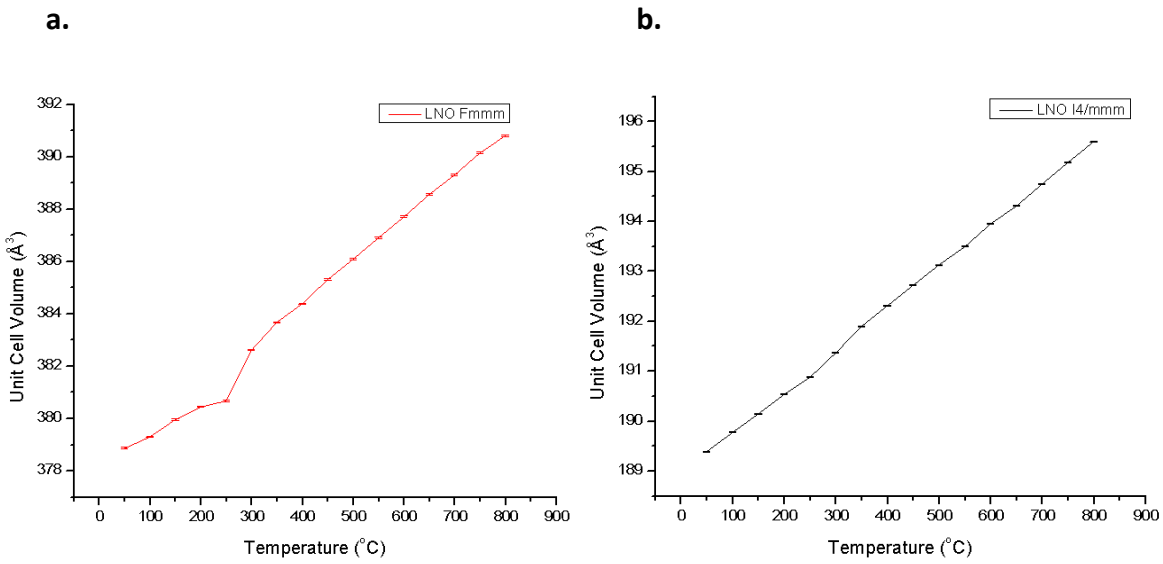

Figure 31. Unit cell volume of LNO with temperature calculated from lattice parameters fitted assuming a: Fmmm space group and b: I4/mmm space group. Note error bars are shown.

All subsequent in-situ XRD data assumes LSGM and LNO with the space groups Pm-3m and I4/mmm respectively.

5.2 In-Situ Temperature XRD in Varying Atmosphere

To ensure the stability of LNO with LSGM in electrolysis and fuel cell working conditions, the LSGM/LNO mix was analysed at temperatures up to 800°C in dry air, humid air (20% H_2O balanced with air) and reduced pO_2 (0.1 atm. balanced with N_2).

Figure 32 shows the observed diffraction patterns for the LSGM/LNO mix at a range of temperatures in 20% H_2O atmosphere, Figure 32a, and in pO_2 = 0.1 atm atmosphere, Figure 32b.

a.

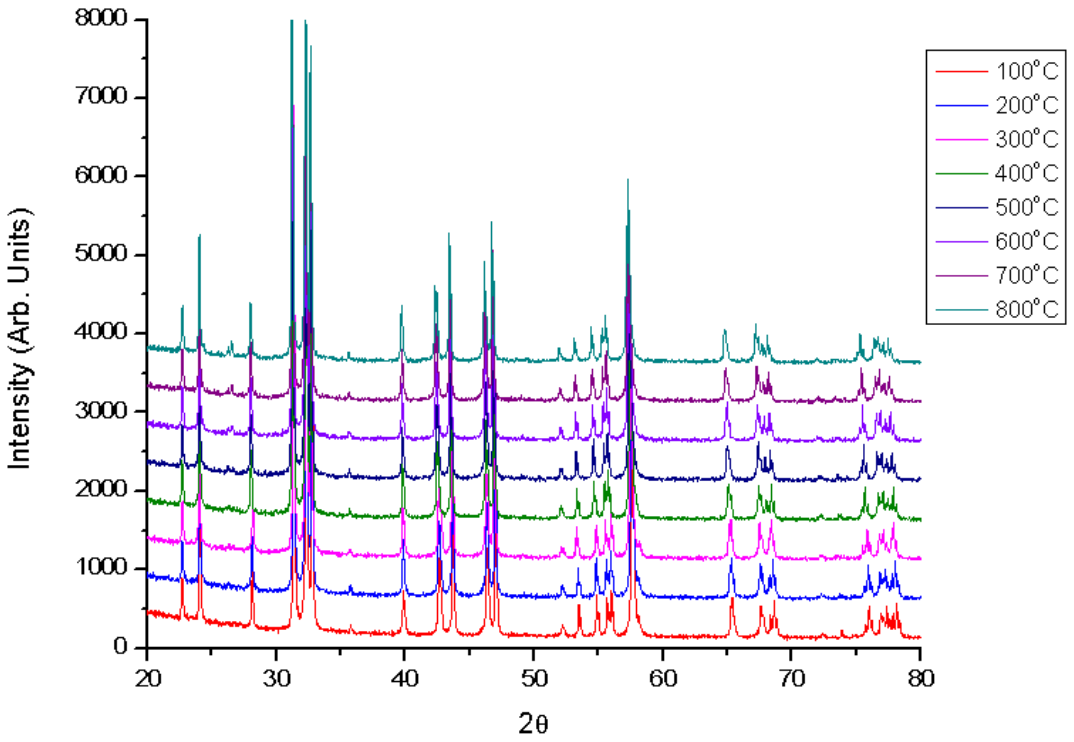

b.

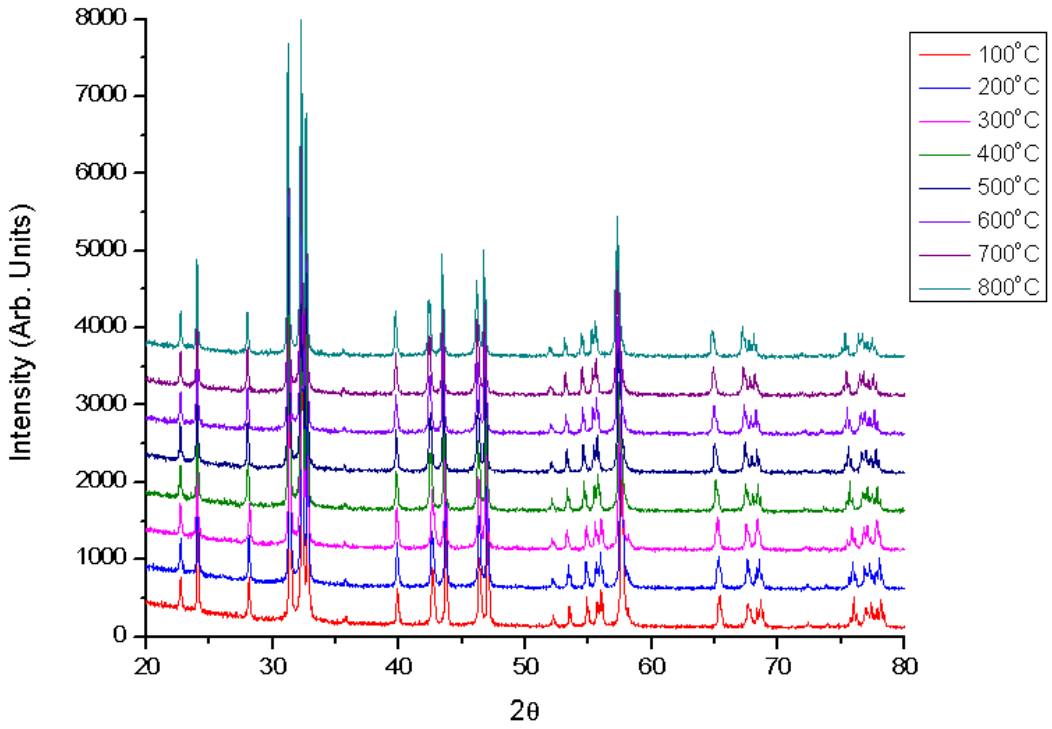

Figure 32. The observed diffraction patterns of 1:1 LSGM/LNO in the temperature range 100-800°C. a: 20% H_2O atmosphere and b: pO_2 = 0.1 atm.

It is observed in Figure 32 that the additional peak at 2θ ~26.5°, discussed in Section 5.1, is once again visible in the patterns produced under humid atmosphere but is missing from those produced in the reduced pO_2 atmosphere. Presuming the peak to be cause by the gold sheet, and because fresh sample powder was used for each experimental run, it is speculated that inexact amounts of powder were analysed with each experiment. A thicker layer of sample may shield the gold sheet sufficiently as to obscure it from the incident X-ray beam and it is suggested this may be the cause of the missing 2θ ~26.5° peak in reduced pO_2 atmosphere. However to be sure that Au_2O_3 is the source of the peak XRD should be run on the gold sheet alone in order to adequately calibrate the XRD patterns.

Figure 33 depicts the change in unit cell volume of LSGM in the temperature range 50 – 800°C in dry air, humid air and reduced pO_2. Unit cell volume increases with temperature with slight deviation from linearity for the sample recorded in reduced pO_2 atmosphere in the temperature range 200 – 400°C.

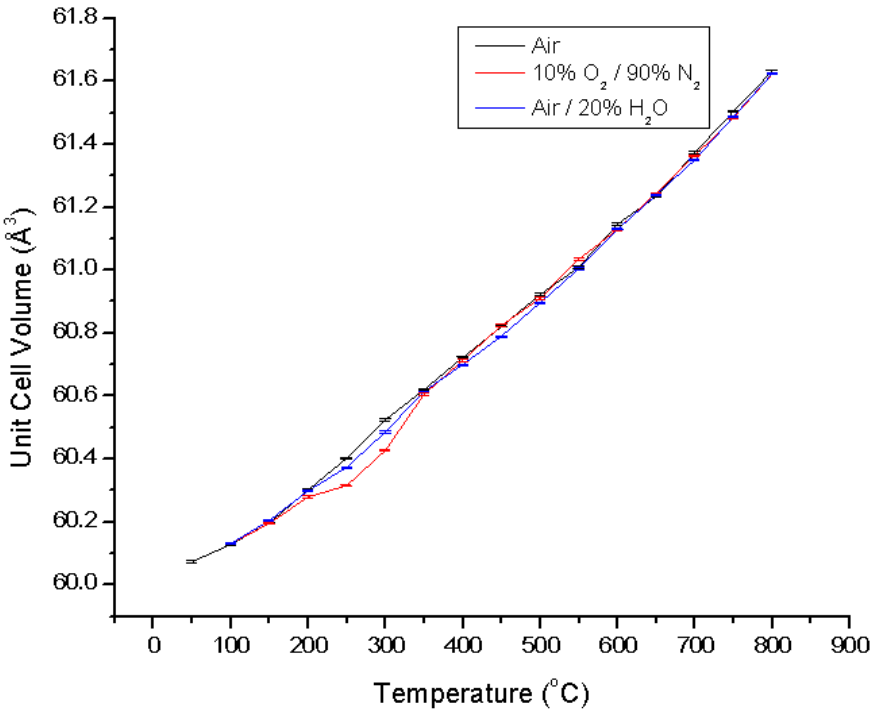

Figure 33. LSGM unit volume with temperature in dry air (black), pO_2 =0.1 atm (red), and 20% H_2O atmosphere (blue). Note error bars are shown.

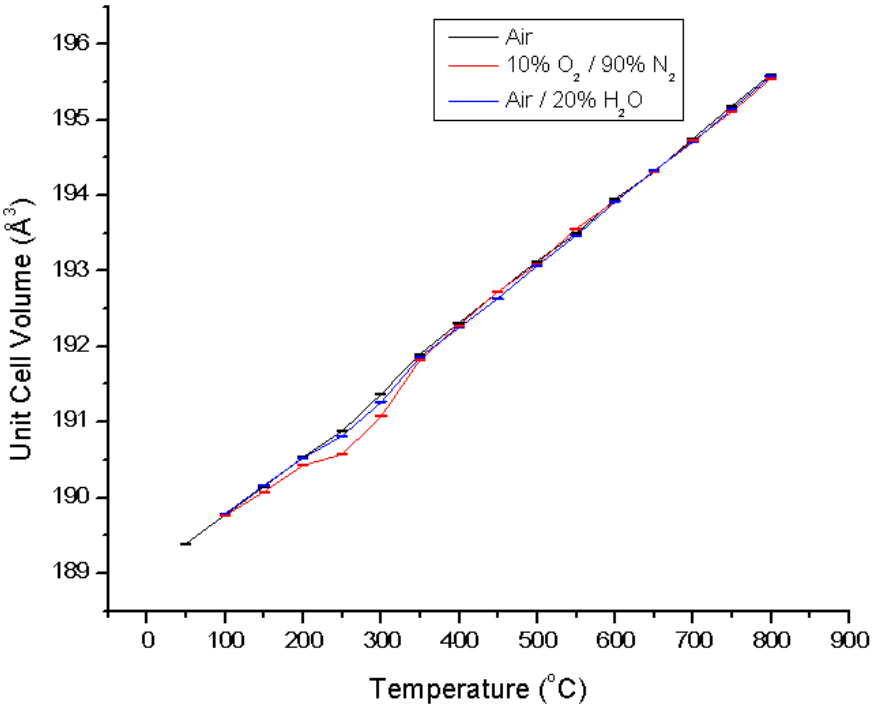

Figure 34. LNO I4/mmm unit volume with temperature in dry air (black), pO_2 = 0.1 atm (red), and 20% H_2O atmosphere (blue). Note error bars are shown.

Figure 34 depicts the change in unit cell volume of LNO in the temperature range 50 – 800°C in dry air, humid air and reduced pO_2. Unit cell volume increases with temperature with deviation from linearity for the sample in reduced pO_2 atmosphere in the temperature range 200 – 400°C.

Jorgensen et al. [84] determined that LNO displayed a mixture of phases at low temperature (Fmmm and Bmab) implying the fitting of LNO with just one phase may be over-simplistic. As temperature increases the LNO undergoes a phase transition from orthorhombic to tetragonal with some discrepancy in the literature as to which temperature this transition is observed, with examples of <150°C [83], 150°C [59] and 350°C [21] presented. The temperature at which LNO undergoes this transition is dependent on the oxygen stoichiometry of the material which itself is influenced by the pO_2 in which the material was produced [59], the pO_2 in which the material is analysed and at what temperature the material is analysed. It is therefore proposed that the deviations from linearity shown in the unit cell parameters of both LNO and LSGM in all atmospheres may be due to an inaccurate

fitting model based on too-simplistic a phase mixture. Further work would include a more detailed analysis of the LNO phase composition in various pO_2 atmospheres.

5.3 Chapter Summary

The compatibility of the powders LSGM and LNO were tested by analysing 1:1 mixture of LSGM and LNO mix in a range of temperatures and atmospheres with in-situ XRD.

LNO unit parameters were seen to deviate from linear expansion with increasing temperature irrespective to the space group used to fit the xrd data, Fmmm or I4/mmm. However only for I4/mmm did the unit cell volume expansion remain linear with increasing temperature, a characteristic observed in literature. I4/mmm structure was therefore used in Le Bail refinement of all data above 100^oC. A review of literature implies that the use of a single LNO phase over this temperature range may be overly simplistic as a phase mixture of different space groups has been reported, as such more detailed analysis techniques and more powerful instrumentation must be employed to fully determine the structure of LNO over a range of atmospheres and temperatures.

Le Bail analysis of the LSGM phase implies the retention the cubic Pm-3m structure across the entire temperature range studied and in all atmospheres. A deviation from linearity of the unit cell volume may be due to the error in analysis of the LNO phase. In order to determine if this is the case, identical in-situ XRD experiments should be conducted on the individual materials.

As temperature was increased on the LSGM/LNO mix an extra diffraction peak was observed to grow with increasing temperature at the angle $2\theta \sim 26.5^o$. After reaction and segregation phases were discounted, this peak was attributed to the gold substrate on which the powder mix was deposited for analysis.

The work presented here suggests that LSGM and LNO do not react at increased temperature up to 800^oC and under reduced pO_2 or increased pH_2O, however further analysis of these two materials, separately and as a mix, is required in order to definitively

determine the compatibility of LSGM and LNO in operational conditions, including increased time at temperature. Determining the stability of LSGM and LNO over a greater range of pO_2 and any current catalytic effects would be invaluable for establishing the suitability of these materials for practical SOEC/SOFC use.

Chapter 6 – Electrochemical Performance of LNO Electrode

The electrochemical performance of the LSGM/LNO system has been determined by Electrochemical Impedance Spectroscopy (EIS) under a range of temperatures, atmospheres and potential biases in order to replicate SOEC and SOFC conditions. Symmetrical and three electrode systems were studied in order to determine individual cathode and anode responses. The three electrode set up is described in section 3.4.

6.1 Pt Electrodes on LSGM in Static Air

To determine LSGM impedance responses, LSGM electrolyte pellets with symmetrical Pt electrodes were first tested under atmospheric conditions.

The electrodes were symmetrical brush painted Pt and were tested in ambient air atmosphere. The EIS response for this system at 400^{o}C is shown in Figure 35. At high to mid frequency two impedance arcs are discerned (Figure 36) with capacitances of the order of R_1 = 10^{-11} F and R_2 = 10^{-8} F which are associated with grain bulk (R_{bulk}) and grain boundary (R_{gb}) electrolyte responses respectively [73].

At low frequency the Pt electrode material displays two impedance responses with capacitances of the order of 10^{-4} F and 10^{-2} F. A capacitance of 10^{-4} F is associated with charge transfer at the electrode surface (R_{ct}) [73] and a capacitance of 10^{-2} F is associated with gas diffusion through the electrode (R_{diff}). [74]

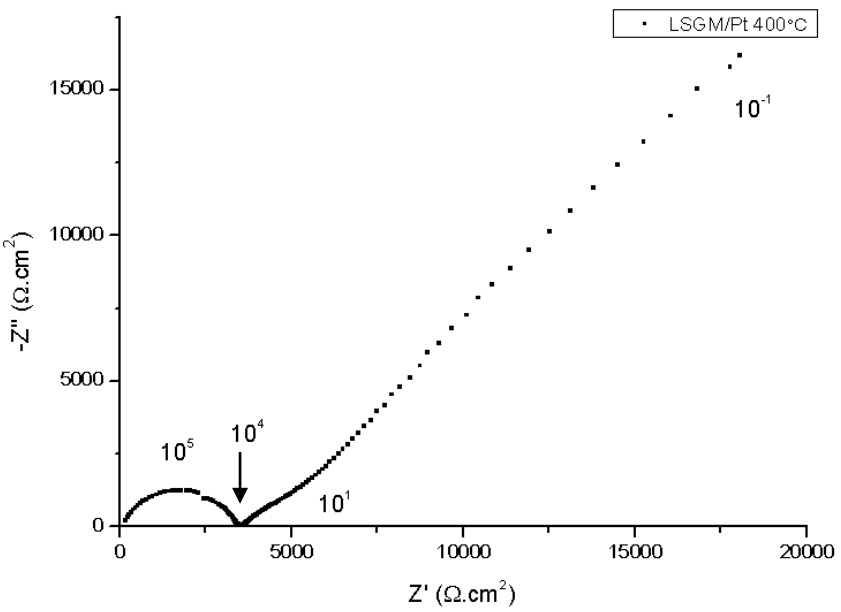

Figure 35. LSGM/Pt symmetrical cell EIS response at 400°C. The frequency (Hz) at which each arc appears is noted on the diagram.

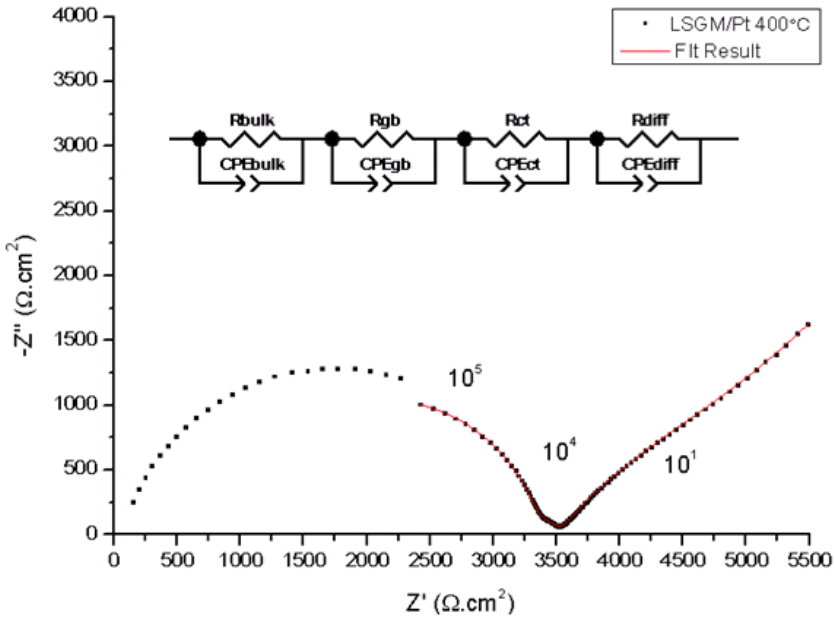

Figure 36. Increased view of high frequency LSGM/Pt symmetrical cell EIS response at 400°C with equivalent circuit displayed. The frequency at which each arc appears is noted on the diagram.

Figure 35 and Figure 36 display the 'jump' in data points at 1MHz, this phenomenon is an artefact of the equipment and discussed in more detail in experimental Section 3.3.

Generating EIS responses across a range of temperatures allows us to build a picture of the processes occurring within the cell. As temperature is increased the electrolyte arcs reduce in magnitude and are incorporated into R_0 as expected (see Section 3.3). R_{bulk} is no longer discernible at 400°C and R_{gb} at 500°C. The equivalent circuit for this cell is shown in Figure 36. *R* and *CPE* represent the resistances and the constant phase elements for the electrolyte bulk, grain boundary and electrode charge transfer and diffusion respectively.

Figure 37 shows an Arrhenius plot of the LSGM responses for the temperature range 200 – 875°C.

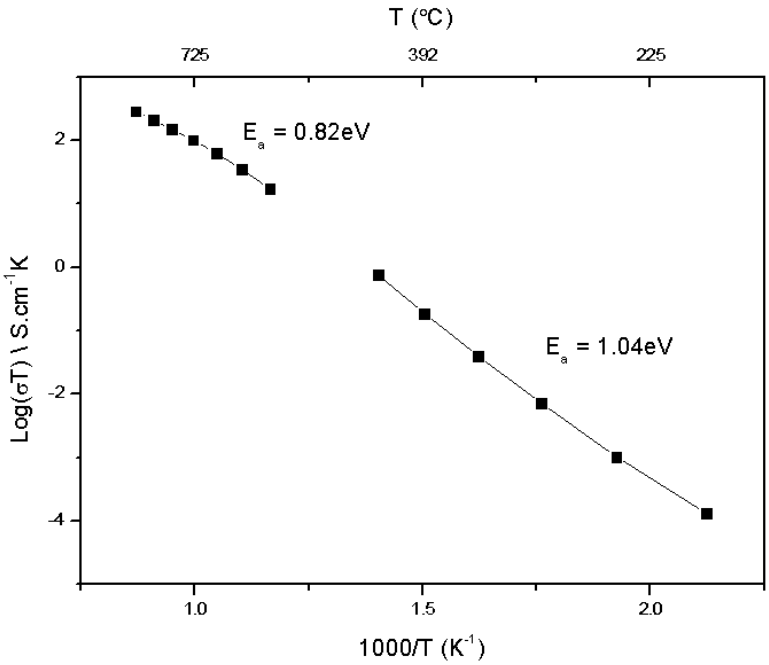

Figure 37. Arrhenius Plot for LSGM recorded with Pt electrodes in ambient air. Activation energies (E_a) for high and low temperature regimes are displayed.

At 600°C a conductivity of 0.03 $S.cm^{-1}$ is recorded for the LSGM electrolyte, this is in line with values reported in the literature. [31, 36] From the Arrhenius plot LSGM activation energies for the low and high energy regimes are calculated to be 1.04 eV and 0.82 eV respectively.

At low to medium temperatures (350 – 550°C) two arcs attributable to the Pt electrode material are visible at low frequency but it is not possible to accurately fit the data as there are not enough data points in the frequency range (Figure 35). The software is able to run a fitting routine for a certain number of data points. However that number of data points may not accurately represent the incomplete arc, highlighting the need for accurate analysis. Conducting the experiment over a wider range of frequencies thereby collecting more data for the low frequency response would increase the accuracy of the fit but drastically increases the run time for collection of each data-set.

Figure 38 shows the Arrhenius plot of the Pt electrode measured in ambient air and shows good linearity of ASR with temperature.

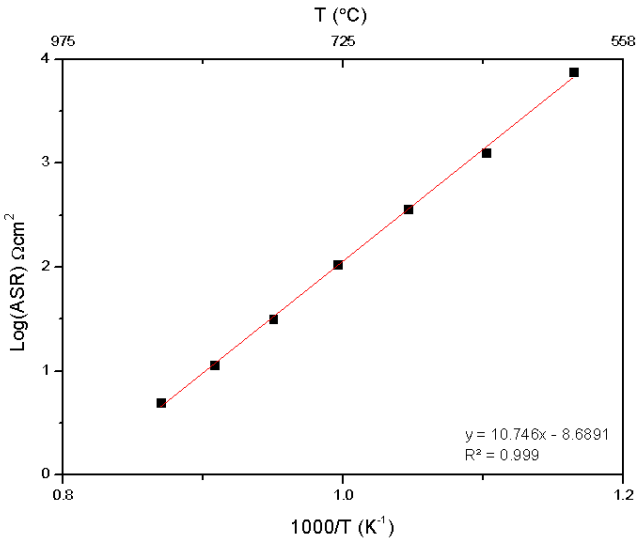

Figure 38. Arrhenius Plot for Pt electrode material recorded on LSGM electrolyte in ambient air. Linear fit displayed as red line.

6.2 LSGM Conductivity in Varying Atmosphere

Figure 39 and Figure 40 show the dependence of total, bulk and grain boundary, LSGM conductivity on atmospheric conditions. Figure 39 is an Arrhenius plot of LSGM in varying pO_2. Three variations of pO_2 atmospheres were applied: high pO_2 of 1 atm.; ambient air with a pO_2 of 0.23 atm.; and a low pO_2 of 6.5×10^{-3} atm. balanced with N_2. In the low temperature

regime conductivity is not dependent on pO_2 atmosphere. However in the high temperature regime the atmospheric conditions do have an effect on conductivity, LSGM conductivity is reduced in low pO_2, this is theorised to be a mass transport issue due to fewer oxygen species being present in the atmosphere. In all atmospheres the activation energy remains fairly constant.

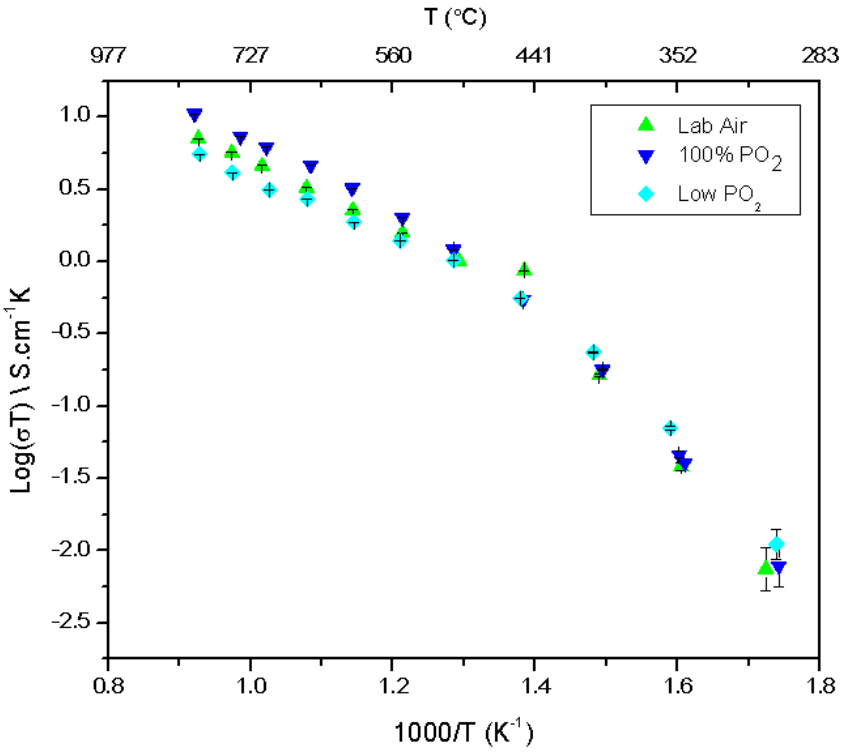

Figure 39. Arrhenius Plot of total LSGM recorded in a range of pO_2. Error bars shown.

Figure 40 depicts LSGMs conductivity response to water vapour. As before three atmospheres were applied: 'humid air' is air passed through a humidifier at room temperature as described in Section 3.3.1; ambient air; and 'Dry Air' has zero pH_2O. Notwithstanding the anomalous 'humid air' result at high temperature, we see that humidity has little effect on the conductivity of LSGM at low or high temperatures. In this experiment humidity was relatively low, 'humid air' = ~3% humidity. [85] Levels of humidity could be increased further by applying heat to the humidifier, using this method humidity of 60% can be achieved. [86]

The conductivities of humid atmospheres against pO_2 cannot be directly compared as the experiments were necessarily conducted on different impedance rigs which required test cells of different dimensions and therefore fabrication techniques, for example an extra sintering step for three-electrode cells which may have an effect on morphology. Although internal resistance of the equipment and cell dimensions are accounted for, large changes in conductivity are noted.

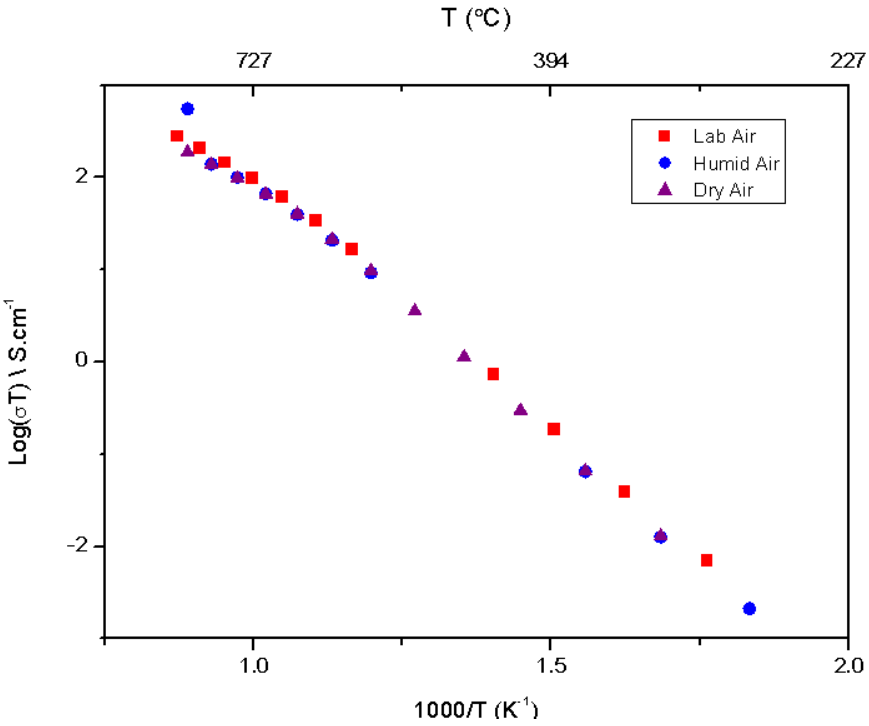

Figure 40. Arrhenius Plot of LSGM recorded in a range of humidities. Square: ambient air; Circle: Humid, 3%, air; Triangle: Dry Air, 0% humidity.

6.3 LNO Polarization in Varying Atmosphere

EIS data were measured for LSGM with LNO electrodes in varying pO_2 and pH_2O atmospheres. As with the impedance data for samples with Pt electrodes, responses may be seen for the LNO electrodes at low to medium temperatures (350 – 550°C) at low frequency. Below 400°C the electrode response is visible but not complete; reliable fitting of the LNO electrode response is only possible above 400°C.

6.3.1 LNO Polarization in Air

Three example EIS plots for medium and high temperature regimes in ambient air are shown in Figure 41, Figure 42 and Figure 43 respectively. In total there are four LNO electrode responses (R_2 – R_5) observed over the temperature range and these are depicted in Figure 44 and detailed in Table 6. Figure 41 depicts the LSGM/LNO system at 500°C. Two responses are observed as two impedance arcs, R_3 and R_4, partially merged. As temperature is increased to 650°C (Figure 42) two more arcs become apparent, R_2 at high frequency and R_5 at low frequency. At temperatures above 500/550°C, responses R_3 and R_4 overlap to such an extent that they are not distinguishable using the ZView software. R_5 becomes more pronounced compared to the total response as temperature is increased to 800°C as shown in Figure 43.

As temperature increases inductance responses are observed at both high and low frequency. Inductance at high frequency is relatively common and predominantly associated with interference from the electronic equipment. An inductance response at low frequency is less common and Jorgensen et al. [87] suggest low frequency inductance is related to segregates or that intermediate oxygen species at the triple phase boundary are responsible, however this phenomenon is not clearly understood. Low frequency inductance is discussed in further detail in Section 6.5.

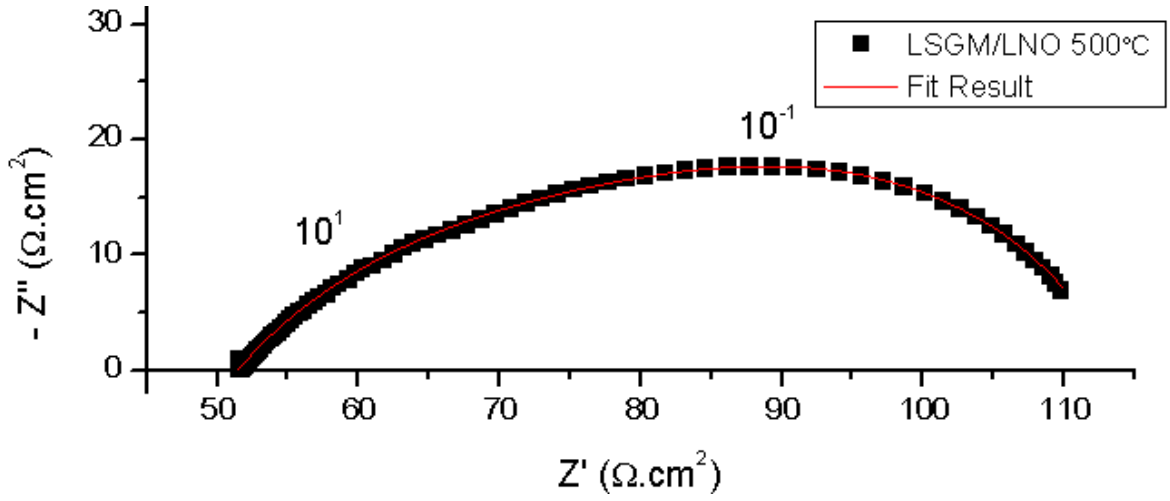

Figure 41. Impedance plot and fitted data for LSGM/LNO symmetrical cell in ambient air at 500°C.

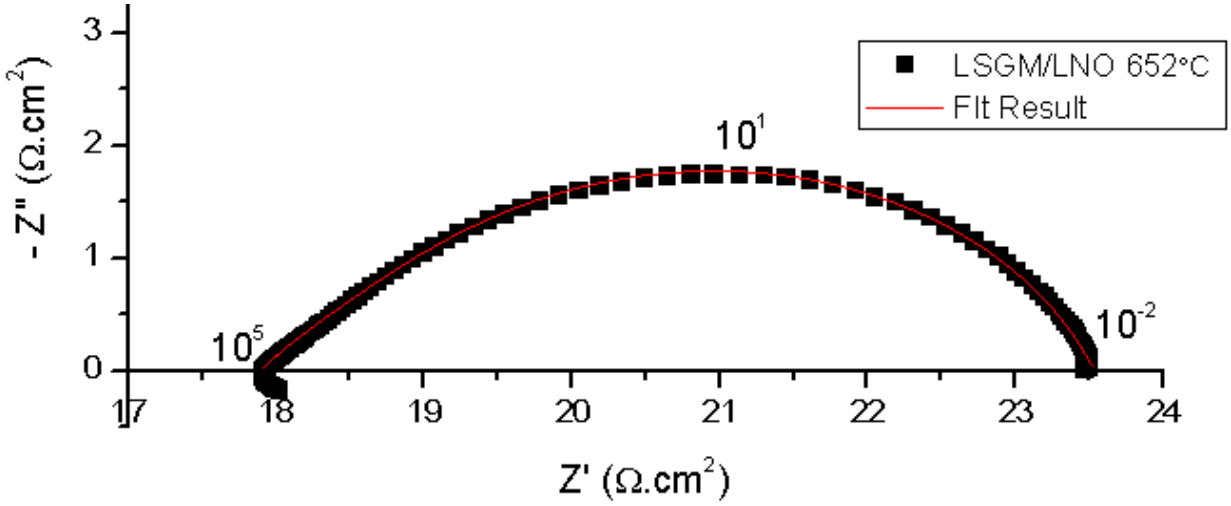

Figure 42. Impedance plot and fitted data for LSGM/LNO symmetrical cell in ambient air at 652°C.

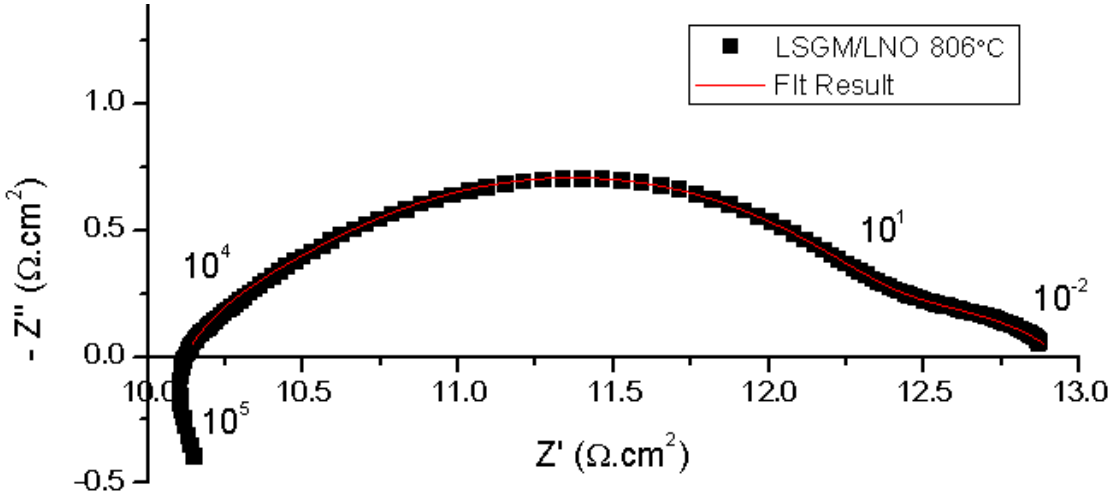

Figure 43. Impedance plot and fitted data for LSGM/LNO symmetrical cell in ambient air at 806°C.

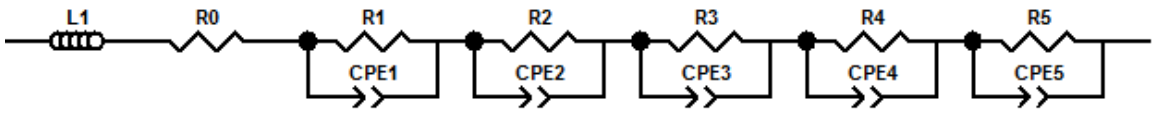

Figure 44. Equivalent circuit for LSGM/LNO symmetrical cell equivalent circuit for temperature range 300 – 800°C. R_1: Electrolyte response, R_2-R_5: LNO electrode response.

For the same material Ferkhi et al. [50] discerned just two "main" impedance responses for LNO and attributed them to charge transfer at the electrode/electrolyte interface and transport phenomena at medium frequency and low frequency respectively. Suggestions for the four LNO responses shown in this study are presented in Table 6.

Table 6. LSGM/LNO Impedance responses and the possible physical phenomena.

Impedance Response	**Capacitance**	**Physical Phenomenon**	**Notes**
R1	2.31 x10^{-9}F at 307^{o}C	Electrolyte grain boundary	Only observable below 400^{o}C
R2	5.5 x10^{-4} F at 709^{o}C	Oxygen ion transfer from electrode-electrolyte interface. [64]	Observable above 650^{o}C; below this temperature this response is so merged with R_3 as to not be visible
R3	7.3x10^{-3}F at 400^{o}C	Electrochemical reactions on Electrode, charge transfer [45]	R_3 is present throughout the temperature range, however as temperature increases R_3 and R_4 merge until inseparable at about 650/700^{o}C, above 450^{o}C, even, the fitting of R_3 may not be reliable due to the influence of R_4
R4	1.36 x10^{-1}F at 500^{o}C	Gas Diffusion to Electrode Surface [74]	R_4 is observable in this frequency range above 400^{o}C but there are only enough points to create a fitting above 500^{o}C, during this temperature range the results may still be influenced by the presence of R_3. Above 650/700^{o}C R_4 merges with R_3, making separate analysis impossible
R5	2.3 x10^{-1}F at 800^{o}C	Oxygen adsorption phenomena. [88]	Only observable above 700^{o}C

Despite being unable to successfully separate the responses R_3 and R_4 this technique offers the total real impedance response for the LNO electrode. It is therefore possible to compare the LNO electrode response under a range of temperatures and potential biases.

6.3.2 LNO Polarization in Varying pO_2

LSGM/LNO cells were examined by EIS under three pO_2 atmospheres: pO_2 = 0.23 atm. (ambient air), pO_2 1 atm. (high pO_2) and $pO_2 = 6.5x10^{-3}$ atm. (low pO_2). Figure 45 depicts the effect of pO_2 on LNO ASR. It is clear that increased pO_2 improves electrode performance. At 800°C ASRs of 1.13, 2.82, and 9.16 $\Omega.cm^2$ were recorded for LNO response in high pO_2, ambient air and low pO_2 respectively.

An improvement of electrode response is expected due to the increased number of available oxygen molecules for reaction. LNO material has also been shown to display increased oxygen stoichiometry via interstitial oxygen ions when exposed to higher oxygen partial pressure, [89] thereby increasing oxygen conduction through the electrode bulk.

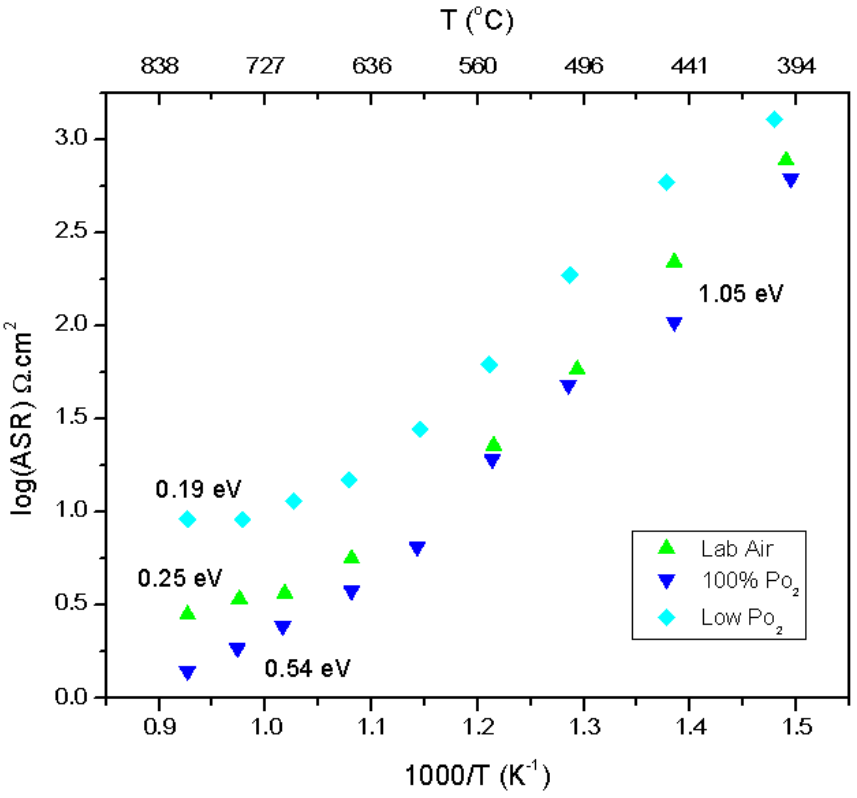

Figure 45. Arrhenius plot of LNO in various pO_2 atmospheres in the temperature range 450 – 850°C. Triangles: Ambient laboratory air; Inverted triangles: 100% pO_2; Diamonds: Low pO_2.

It is also noted that for all pO_2 atmospheres the LNO electrode displays two regimes. In the low temperature regime (~400 – 650°C) the electrode has an E_a of ~1.05 eV independent of oxygen partial pressure. In the high temperature regime (~700 – 850°C) ASR is seen to decrease less rapidly with increasing temperature. Figure 45 implies that the extent to which the electrode polarisation response increases with temperature may be dependent on oxygen partial pressure.

Whilst it may be expected for an electrode material to display linear activation energy over the temperature range 300 – 800°C, the non-linear behaviour of LNO on YSZ and CGO has been noted by Sayers et al. [7] who suggest the change in activation energy is due a change in dominant electrode process. The high temperature regime may be dominated by the electronic conductivity of LNO. [10] As temperature increases electronic conductivity decreases thereby increasing the electrode ASR. Sayers et al. [7] also studied LNO with a Pt current collector layer, which had the effect of removing the change of activation energy; this further suggests that the change is due to the reduced electronic conductivity of the electrode at elevated temperatures.

6.3.3 LNO Polarization in Varying pH_2O

As discussed in Section 2.2.1 the oxygen electrode is most commonly studied in SOEC/SOFC literature as it contributes the greatest proportion of electrode overpotential to an SOEC or SOFC cell. In this study EIS was also conducted under humid atmosphere in order to determine the suitability of LNO as a potential electrolysis cathode. Humid atmosphere was achieved by flowing air through a water bubbler at room temperature. The humid air was then passed through the impedance rig as described in Section 3.3.1.

Figure 46 depicts the effect of pH_2O on LNO polarisation response. A humidity of 3% appears to increase LNO polarisation, but reduces the change in activation energy so that at high temperature the recorded ASRs for dry and humid atmosphere are almost equivalent at 10.4 and 10.9 $\Omega.cm^2$ respectively. A possible explanation for the reduced change in E_a is the presence of water vapour aids charge transfer thereby counterbalancing the reduction

in electronic conductivity that LNO suffers above 650°C, as discussed further in Section 6.4.2. However it is shown that the addition of water vapour to the atmosphere may cause degradation of the LNO material in contact with the Pt mesh current collector; see Chapter 7 for more detail.

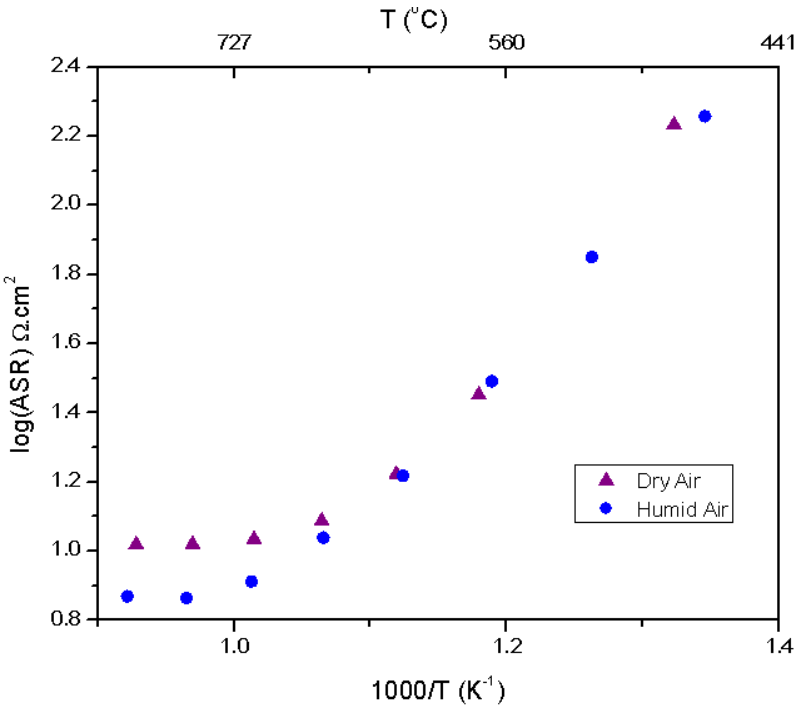

Figure 46. Arrhenius plot of LNO ASR in dry and humid atmosphere in the temperature range 450 – 850°C. Triangles: 0% humidity Dry Air, Circles: 3% Humid Air.

It is noted that there is a discrepancy in the activation energy of LNO in the low temperature regime conducted in varying pO_2 (Figure 45) and pH_2O (Figure 46). It is not possible to determine if this is the effect of humidity or the necessity to use separate experimental rigs for each set of experiments. Despite equipment and cell calibration the fabrication of cells of two different dimensions may cause the fabrication techniques to have different effects on the material's microstructures. This highlights the necessity to reduce variables in such a study.

6.4 Potential Bias

In order to more accurately recreate the conditions in which electrolytes and electrodes operate when used in SOEC and SOFC cells, the LSGM/LNO system was examined by EIS with varying potential bias. As described in Section 3.5, positive bias represents operation in an anodic mode and negative bias represents cathodic mode.

6.4.1 LSGM Conductivity in Varying Bias

Figure 47, Figure 48 and Figure 49 depict the effect of implementing bias on the LSGM electrolyte in ambient laboratory air, high pO_2 and low pO_2 respectively. In ambient air and pO_2 = 1 atm., varying potential bias from OCV to ±1000mV has no visible effect on the electrolyte material. When placed in $pO_2 = 6.5x10^{-3}$ atm. a greater degree of 'noise' is seen in the impedance data thereby making analysis less reliable. Figure 49 shows a slight degree of spread in the LSGM conductivity dependant on potential bias; -1000mV displays the largest effect on LSGM conductivity, reducing conductivity at high temperature.

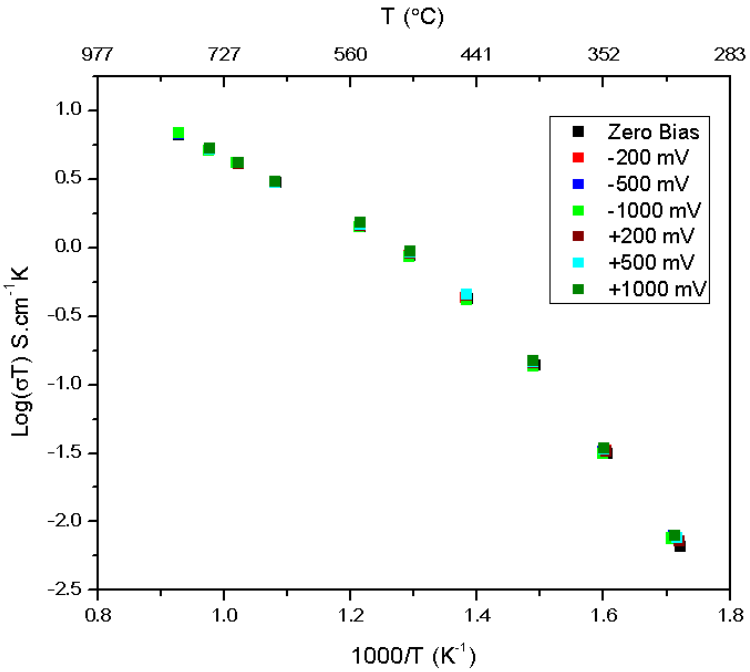

Figure 47. Arrhenius plot of LSGM in ambient air atmosphere under potential bias in a temperature range 300 – 850°C. Due to low dependence of the conductivity of LSGM on potential bias, many data points are not visible.

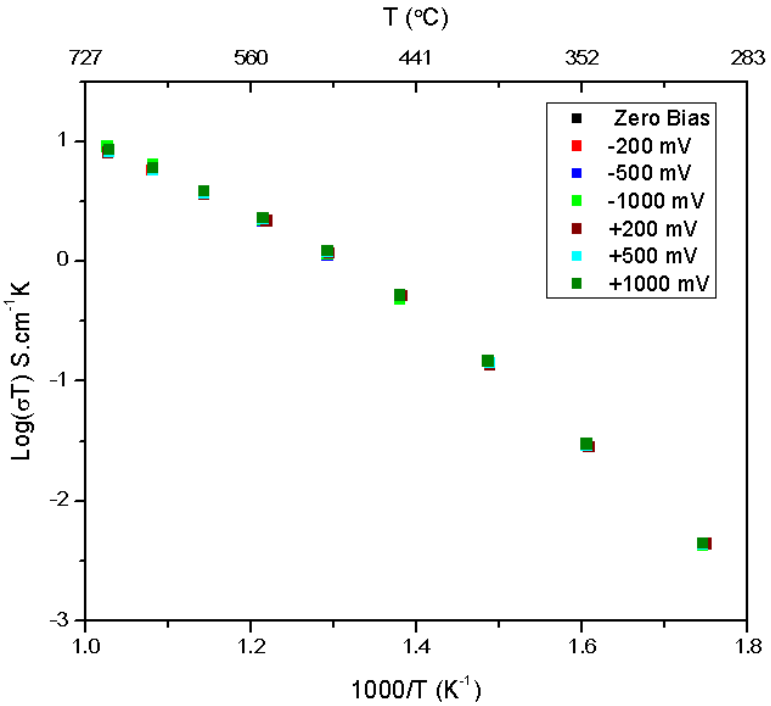

Figure 48. Arrhenius plot of LSGM in pO_2 = 1 atm. under potential bias in a temperature range 300-850°C. Due to low dependence of the conductivity of LSGM on potential bias, many data points are not visible.

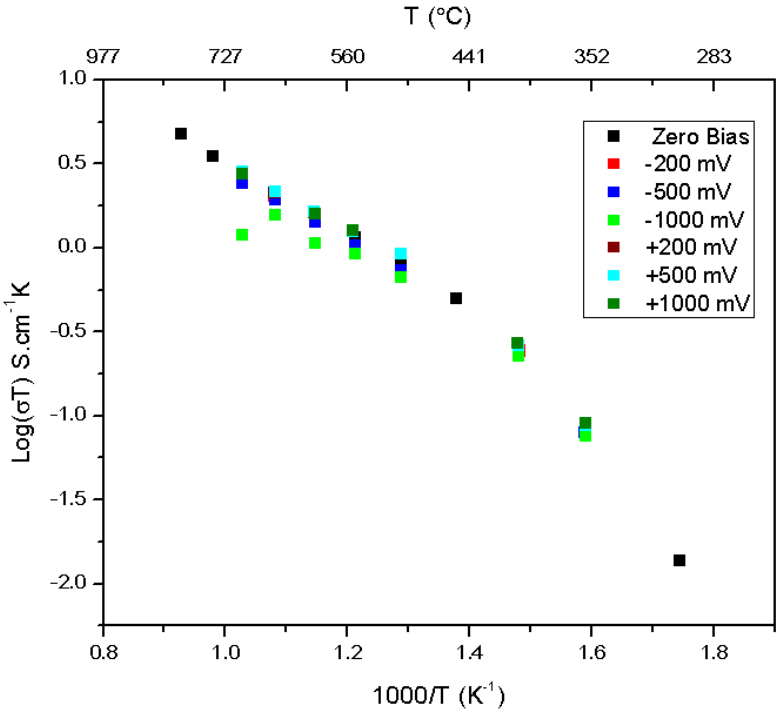

Figure 49. Arrhenius plot of LSGM in pO_2 = $6.5x10^{-3}$ atm. under potential bias in a temperature range 300 – 850°C. Due to low dependence of the conductivity of LSGM on potential bias, many data points are not visible.

6.4.2 LNO Polarization in Varying Bias

Figure 50, Figure 51 and Figure 52 depict the effect of implementing bias on the LNO electrode in ambient laboratory air, high pO_2 and low pO_2 respectively. It should be noted that applying a bias often had the effect of introducing noise and artefacts into the plots that could not be fitted with the software. This was exacerbated with increasing potential bias and is discussed in more detail in Section 6.5. In such cases the data have not been included in the figures.

In both ambient air and pO_2 = 1 atm. the application of bias in either anodic or cathodic mode has a positive effect on the LNO material, reducing ASR across the temperature range. At high temperature the change in activation energy of LNO is still observed independent of potential bias.

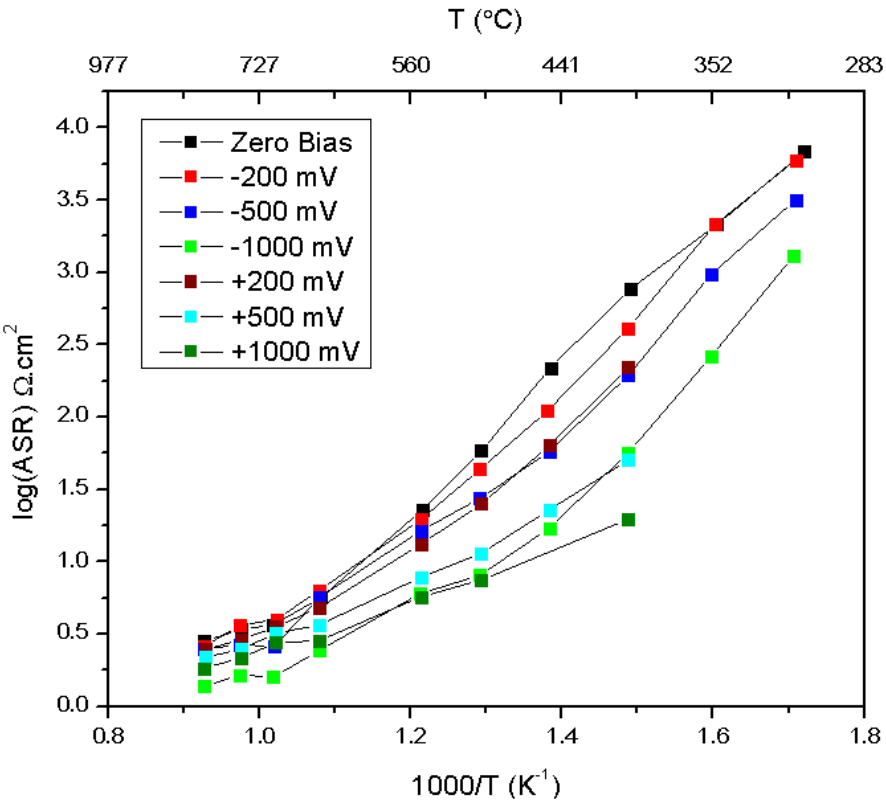

Figure 50. Arrhenius plot of LNO in ambient air atmosphere under potential bias.

In ambient air at high temperatures, the greatest improvement to LNO ASR is achieved by applying -1000mV, followed by +1000mV, +500mV and -500mV respectively. Across the temperature range the increase in applied bias improves ASR. Towards the low temperatures, the positive bias data display greater instability and cannot be fitted below 400^{o}C. In ambient air at 800^{o}C LNO ASRs were 2.82, 1.83 and 1.37 Ω.cm^{2} in OCV, +1000mV bias and -1000mV bias respectively.

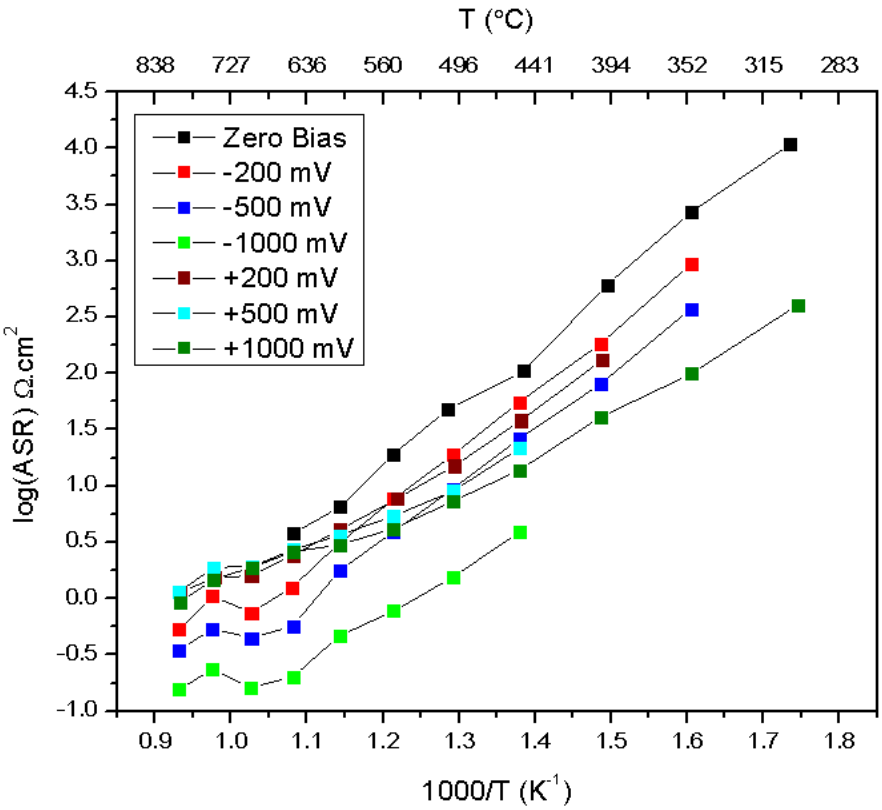

Figure 51. Arrhenius plot of LNO in pO_2 = 1 atm. under potential bias.

In pO_2 = 1 atm. at high temperatures, -1000mV clearly displays the greatest improvement to LNO ASR followed by -500mV and -200mV respectively. The positive bias showed little variation from OCV at high temperature but shows greater improvement and stability at lower temperatures. In low pO_2 at 800°C LNO ASRs were 1.13, 0.93 and 0.16 $\Omega.cm^2$ in OCV, +1000mV bias and -1000mV bias respectively.

Chen et al. [90] noted that applying a potential bias may cause reduction and oxidation of an electrode material thereby varying the number of oxygen vacancies. This may only be part of the explanation for the reduced ASR shown in this study as LNO predominantly conducts oxygen via interstitials. Perez-Coll et al. [12] also state that the relaxation time of electrodes enhanced by current polarization to return to pre-bias ASR is longer than the time taken for oxidation states to revert (hours and days rather than minutes), thereby highlighting the need for further study of the processes occurring during potential bias.

In this study it is suggested that the increase in electrode performance when a bias is applied is due to an increased reaction rate at the working electrode when a negative bias is applied (external electrons flow to the WE), or counter electrode when positive bias is applied (external electrons flow to the CE).

In low oxygen atmosphere, $pO_2 = 6.5x10^{-3}$ atm. the application of bias has a drastic effect on the ASR of LNO, Figure 52.

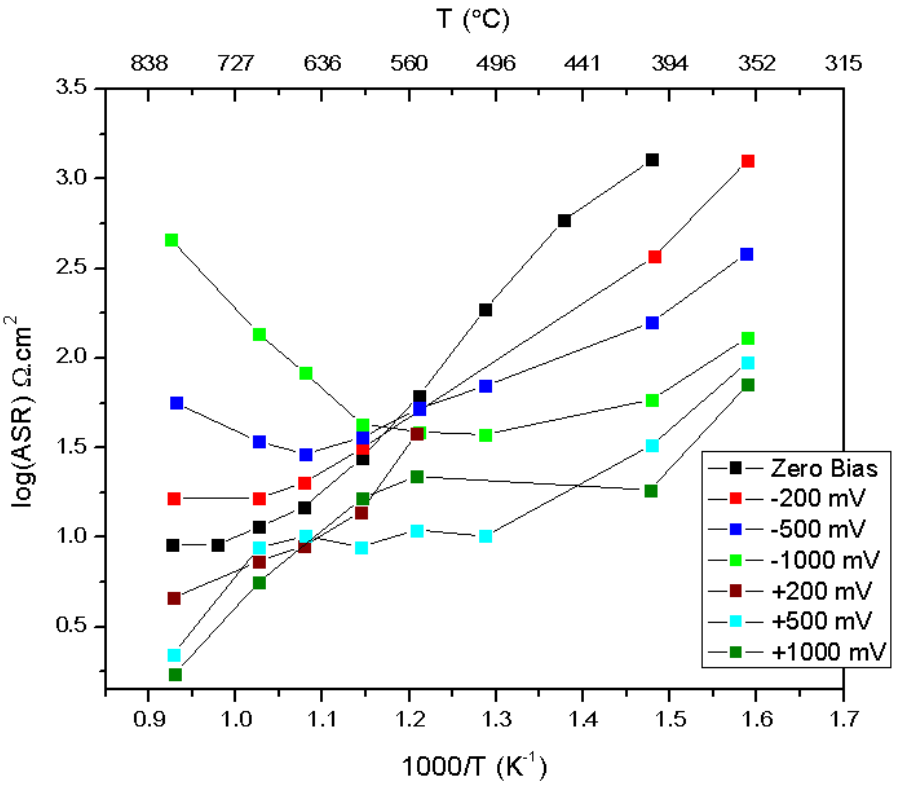

Figure 52. Arrhenius plot of LNO in $pO_2 = 6.5x10^{-3}$ atm. under potential bias.

In the low temperature regime the application of bias in both cathodic and anodic modes reduces ASR, with +1000mV displaying the greatest improvement. In the high temperature regime positive bias reduces LNO electrode resistance however negative bias increases ASR. In low pO_2 at 800°C LNO ASRs were 9.17, 1.74 and 456.9 $\Omega.cm^2$ in OCV, +1000mV bias and -1000mV bias respectively.

Figure 53 shows the electrode impedance response under -1000mV bias in low pO_2 atmosphere as temperature increases. The electrolyte response decreases as expected, shown by a shifting of the high frequency intercept towards lower Z' as temperature increases, however the increase in electrode response is apparent.

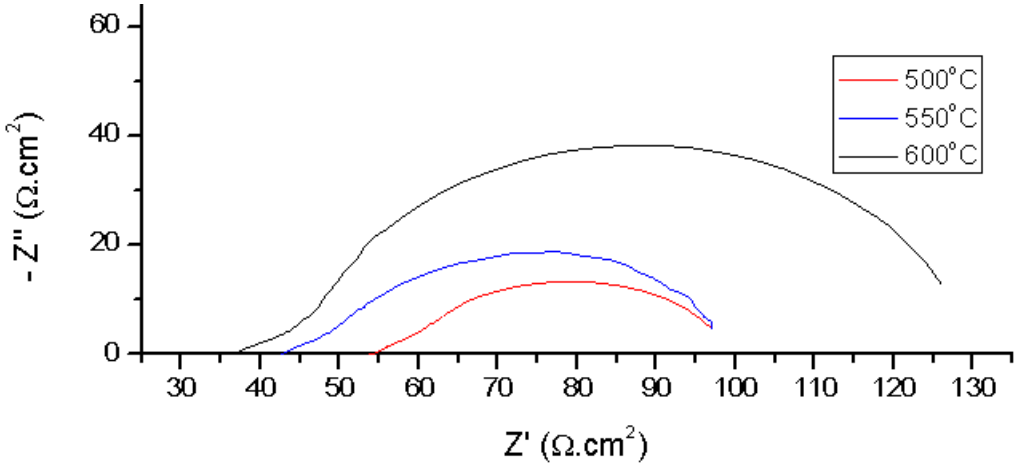

Figure 53. Impedance response of LSGM/LNO three electrode cell in pO_2 = $6.5x10^{-3}$ atm. under -1000mV bias at 500°C (red), 550°C (blue) and 600°C (black)

The arc that increases with temperature shown in Figure 53 is attributed to the merged R_3 and R_4 responses however it was not possible to separate the responses. Fitting the arcs as a single RC element returned capacitance values of the order 10^{-2} F, a value in-between those expected for R_3 and R_4. It is therefore suggested that the response increasing with temperature in low pO_2 atmosphere is either due to charge transfer or gas diffusion to the electrode surface.

Knibbe et al. [15] notice an increase in Ni/YSZ electrode impedance with increasing current density and attributed this effect to the act of operation shifting the fuel composition available for reaction. For low pO_2 at high temperatures mass transport of oxygen may fail to keep up with electrode capability when an external supply of electrons is applied, resulting in increased impedance responses and exacerbated by the poor electronic conductivity of LNO above 600°C. [7] This is not observed in positive bias as in positive mode

oxygen is not being supplied to the electrode from the atmosphere and so mass transport and/or adsorption on the electrode surface is not occurring.

6.5 Impedance Artefacts

Figure 54 and Figure 55 display the impedance responses of the LSGM/LNO system in ambient air at 805°C, open circuit operation is shown in both figures with positive bias shown in Figure 54 and negative bias shown in Figure 55.

As discussed in the previous section the application of bias in either direction, in ambient air, improves electrode performance shown by a decrease of impedance response. The figures below show a deconvolution of the low frequency response, R_5, when negative bias is applied, this separation of R_5 from the other electrode responses is not observed when positive bias is applied.

It is also shown that low frequency inductance is seen in all positively biased impedance arcs but not in negatively biased arcs. However Figure 55 displays R_5 responses that are not complete, it may be the case that low frequency inductance would be achieved in the negatively biased system if the range of frequencies over which the impedance spectroscopy was conducted was increased further.

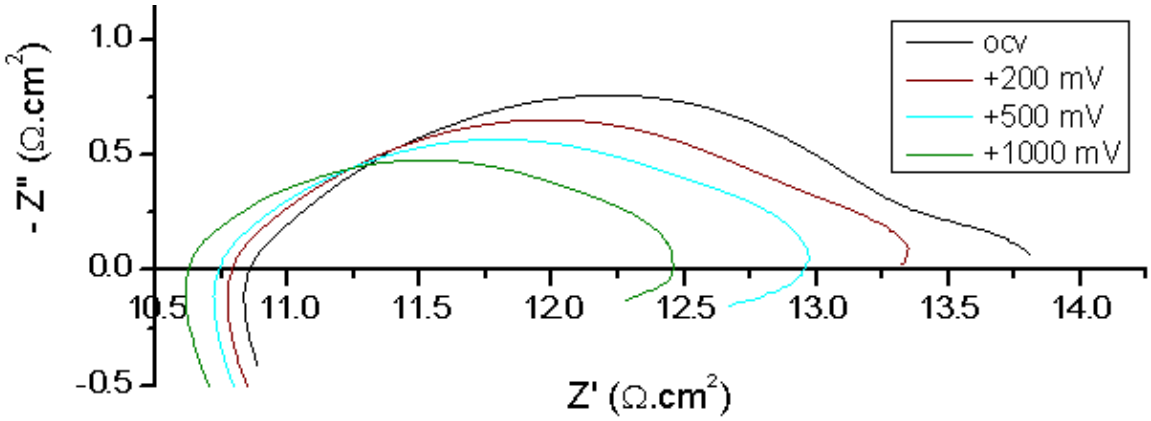

Figure 54. Impedance response of LSGM/LNO three electrode system in ambient air at 805°C at ocv and positive bias.

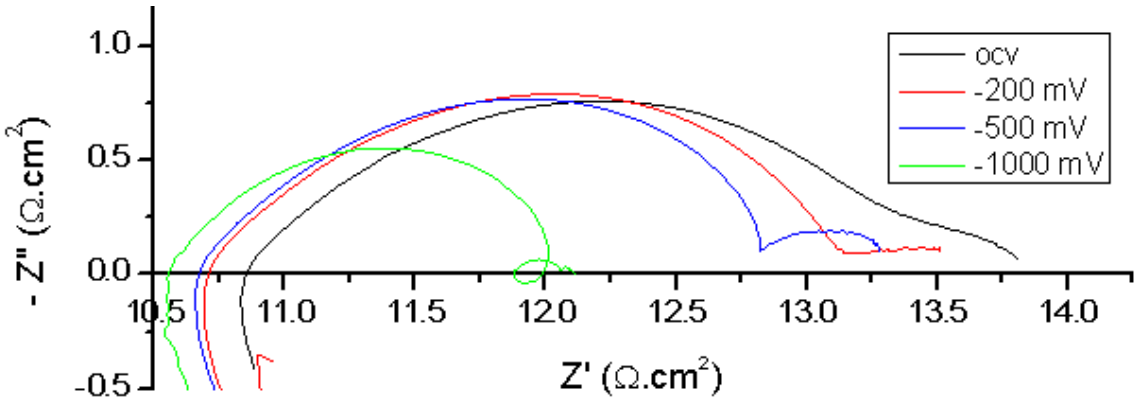

Figure 55. Impedance response of LSGM/LNO three electrode system in ambient air at 805°C at ocv and negative bias.

Liang et al. [91] noted low frequency inductance in palladium-promoted LSM-based cathodes (for SOFC) and attributed this to O_2 reduction or fuel oxidation, but conceded that further work was required in order to understand this response. Other works include a similar explanation for the low frequency inductance feature, namely enhanced adsorption/desorption of oxygen species and electrochemical reactions on the surface of nano-structured electrodes. [92, 93] Laguna-Bercero et al. attribute low frequency inductance to activation of a passive layer at the electrode surface. [44] Low frequency inductance can also be a response of an unstable system or corrosion over the time period of the experiment. Despite theorised explanations such as these, it is clear further experimental research is required in order to determine the physical processes behind the low frequency inductance response.

Figure 55 displays a low frequency inductance response that loops entirely to form a final low frequency impedance arc, presumed to be R_5 but unable to be fitted to satisfactory level of error in the software. Loops between electrode responses such as this are found in the literature [91-93], however such loops between electrolyte and electrode responses (Figure 56) have not been found in the literature by this author.

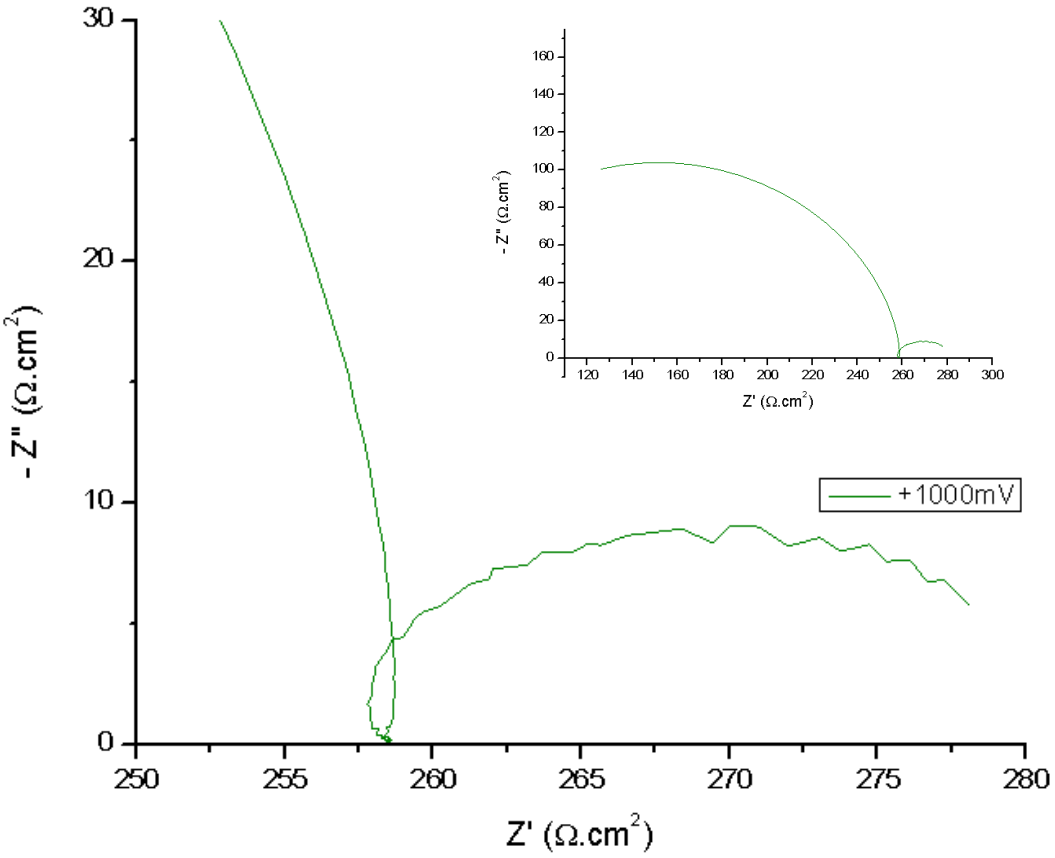

Figure 56. Detail of 'loop' between two impedance responses of the LSGM/LNO three electrode system in ambient air at 399°C under +1000mV bias. Inlay displays the complete response across the frequency range 1 MHz – 0.01 Hz

Figure 56 depicts the impedance response of the LSGM/LNO system in ambient air at 399°C and under +1000mV bias. A loop is discernable between the larger electrolyte arc and smaller electrode response, this loop does not cross the Z' axis and so is not inductance and may be attributed to corrosion, instability of the system or the formation of higher order Ruddlesden Popper phases at the counter electrode catalysed by Pt current collectors. It is also clear that the electrode response is subject to a greater amount of noise than has previously been witnessed under OCV (Figure 35, Figure 41). It is suggested that the application of bias has reduced the electrode response to such a degree as to make it more susceptible to noise effects. The application of bias may also be exacerbating instrument artefacts such as inductance responses to such a degree as to make any results untrustworthy. A robust investigation into the cause of induction loops and other instrumentation artefacts should be undertaken in order to satisfactory determine the

effect of bias and whether such responses can be removed from the data, either by software analysis or by the physical set up of the experimental equipment.

6.6 Chapter Summary

EIS has been used to study LNO electrodes with a LSGM electrolyte under a range of atmospheres and applied bias to mimic aspects of solid oxide electrolysis and fuel cell working conditions.

LNO displays a change in activation energy at ~600^{o}C which has been noted elsewhere in the literature and is attributed to a change in dominant electrode process due to decreasing electronic conductivity.

The performance of LNO is improved by increasing oxygen partial pressure due to the increased availability of oxygen species for reaction. The ASR of LNO was shown to increase in increased H_2O partial pressure with a decreased change in E_a compared to dry air. A possible explanation for the reduction in change of E_a with increased pH_2O is that the presence of water vapour aids charge transfer thereby counterbalancing the reduction in electronic conductivity that LNO suffers above 600^{o}C, however the reader is directed to Chapter 7 in which scanning electron microscopy (SEM) of the LNO surface after use in humid atmosphere shows degradation.

For ambient air and high pO_2 atmosphere, an applied bias of either cathodic or anodic nature increased LNO performance over the total temperature range. It is suggested that this is due to current flow aiding reactions on the electrode surface. For low pO_2 atmosphere a bias of either direction reduces LNO ASR at low temperatures but only positive, anodic bias improves performance at high temperatures. The application of negative, cathodic bias is shown to increase the cathode ASR. This may be due to the electron density supplied to the electrode being too high compared to the low availability of oxygen for reaction. The application of bias has also been shown to introduce or exacerbate existing experimental artefacts in the impedance responses such as low frequency inductance. Some such artefacts have been discussed in the literature however there appears to be a lack of

understanding and it is suggested that investigation of these unwanted responses under bias would allow for more informed study of materials under electrolysis and fuel cell modes of operation.

Literature often states the target of 0.15 Ωcm^2 [94] for electrode material ASR in order for it to be competitive. LNO material in ambient air and low pO_2 and pH_2O displays ASR values at least an order of magnitude higher than this. However, LNO in high pO_2 and OCV displays an ASR of 1.13 Ωcm^2 at 800^oC which is reduced to 0.92 Ωcm^2 and 0.16 Ωcm^2 when + 1000mV and -1000mV are applied respectively. These values could be reduced further with the addition of an electronic current collection layer.

Great care is required when studying EIS responses. As has been shown in this study two or more phenomena may be responsible for the data, yet are not discernable in the impedance plots due to the very similar relaxation frequencies. Along with further studies with a wider range of pO_2 and pH_2O atmospheres it is suggested that the distribution of relaxation times (DRT) analysis be implemented to the data in order to more accurately separate the constituent processes.

In order to mimic working conditions further, two separate atmospheres must be supplied to the anode and cathode electrodes in order to reproduce solid oxide electrolysis and fuel cell operation and thereby account for electrochemical potential across the cell.

Chapter 7 – SEM Analysis

SEM images were taken of LSGM/LNO pellets before and after impedance spectroscopy in various atmospheres. Figure 57 shows SEM images of the LNO surface, a, and the interface between LNO and LSGM, b. This cell was not previously studied with EIS.

a **b**

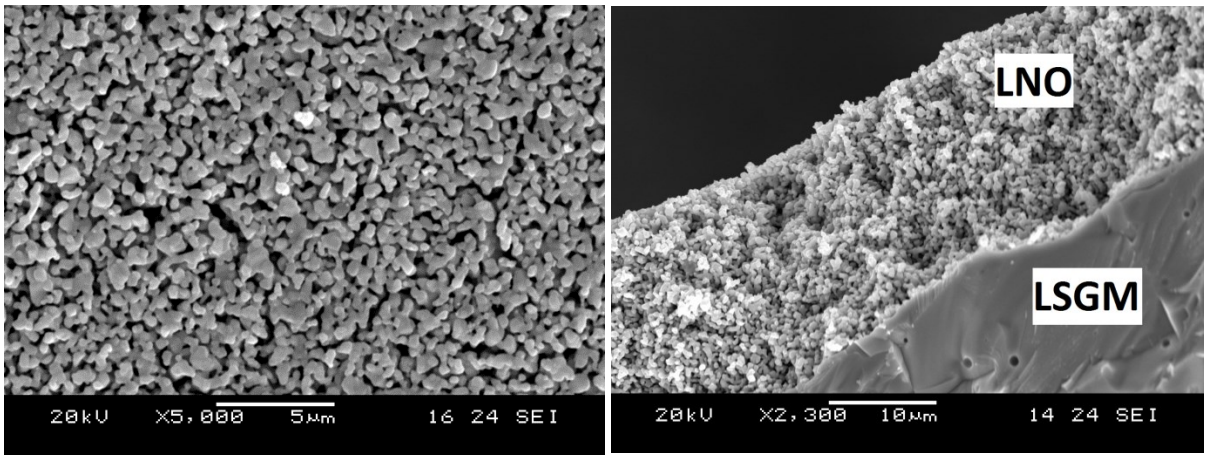

Figure 57. SEM images of LNO electrode on LSGM electrolyte. a: LNO electrode surface. b: LNO/LSGM interface. Note the change of scale.

LNO shows good porosity and adhesion to the LSGM electrolyte. The LSGM shows good density as discussed in Section 3.2.1, with some closed porosity.

After impedance spectroscopy in air, high and low pO_2 and under bias all cells show stability with no change in microstructure save surface damage attributed to Pt mesh current collectors of the impedance set-up which are applied to the electrode surface with pressure. An example SEM of LSGM/LNO cells after impedance in high pO_2 are displayed in Figure 58 and are representative of cells after impedance in the aforementioned conditions.

a.

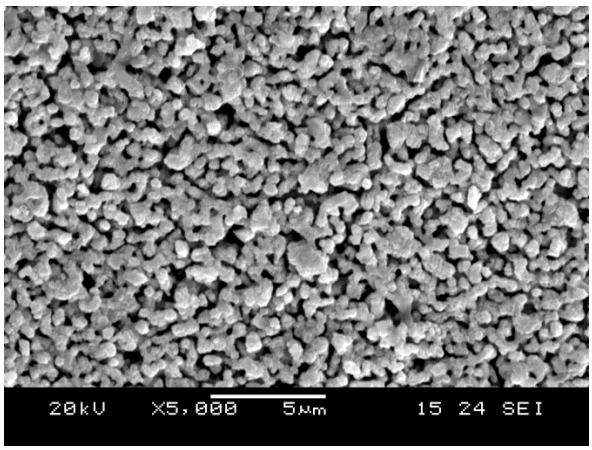

b.

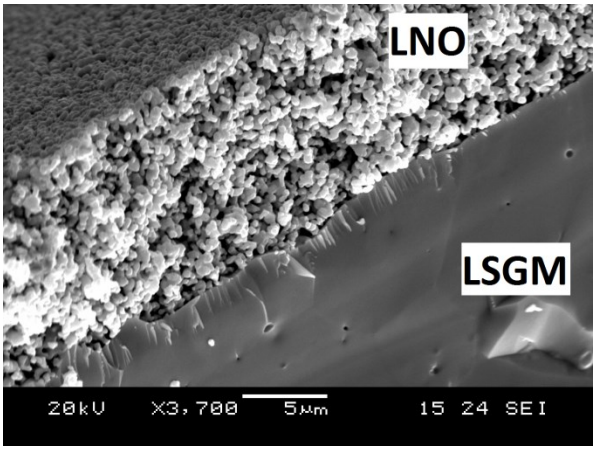

c.

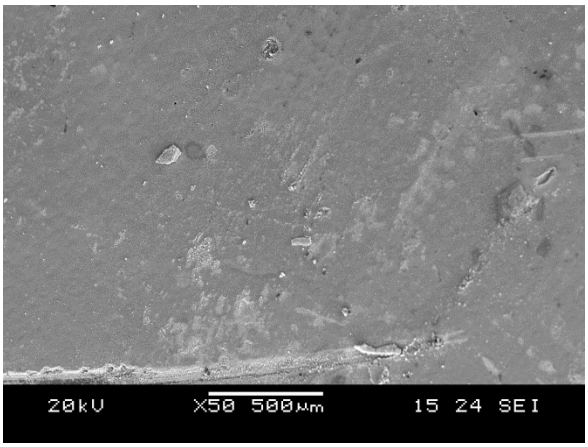

Figure 58. SEM images of LNO electrode on LSGM electrolyte after impedance in pO_2 = 1 atm. a: LNO electrode surface. b: LNO/LSGM interface. c: Wide view of LNO surface displaying surface damage attributed to Pt current collector.

In contrast, SEM images of LSGM/LNO cells after impedance in 3% H_2O atmosphere do show alteration as shown in Figure 59.

a.

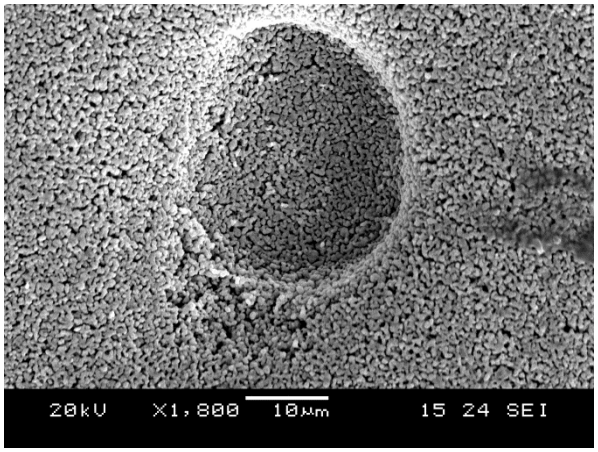

b.

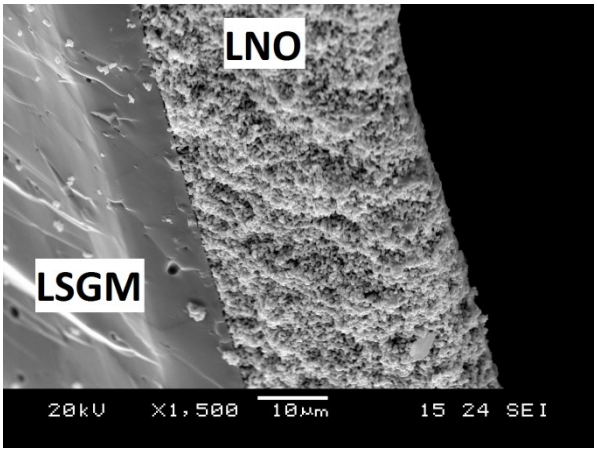

c.

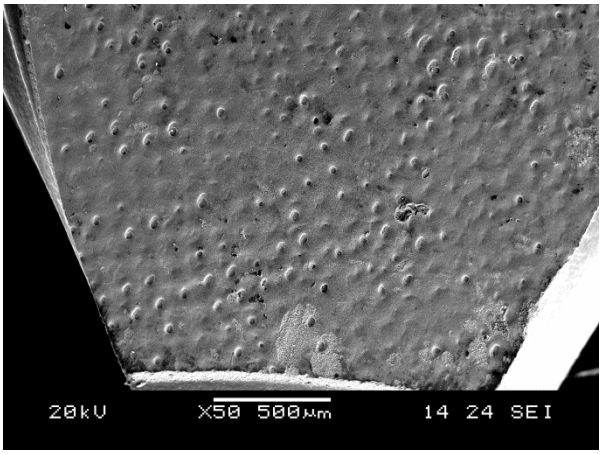

Figure 59. SEM images of LNO electrode on LSGM electrolyte after impedance in 3% H_2O atmosphere. a: LNO electrode surface. b: LNO/LSGM interface. c: Wide view of LNO.

After impedance in a humid atmosphere the LNO surface developed regular surface features as shown in Figure 59 a and c. From Figure 59 c it is noted that the features appear regular and spaced at ~0.125mm. The aperture of the Pt mesh used as a current collector is of the order of 0.125 mm and so it is suggested that the mesh catalysed a degenerative reaction or provided nucleation points at which moisture from the humid atmosphere could concentrate, damaging the electrode. However further study of LNO electrode in humid atmosphere is required in order to satisfactorily determine the process occurring.

Chapter Summary

SEM images are presented of LSGM/LNO cells fresh from fabrication with no pre-testing conditions applied to them. These images show good microstructure, porosity and adhesion of the LNO on the LSGM electrolyte. The LSGM shows good density with some closed porosity that in future works should be minimised.

SEM images of an LSGM/LNO cell after undergoing electrochemical impedance spectroscopy (EIS) is presented as a representative of all cells studied under air and varying pO_2 atmospheres and under all applied biases. LNO displays good adhesion to the electrolyte and shows no alteration in microstructure or porosity. After EIS work some mechanical damage is seen as scratches in the electrode surface attributed to the Pt current collector applied to the electrode with pressure.

SEM images of an LSGM/LNO cell after undergoing electrochemical impedance spectroscopy in humid atmosphere is presented. Despite showing continued adhesion to the LSGM material and un-altered microstructure, this cell displays a regular pattern of damage across the LNO surface. The pattern appears to be of the same order of magnitude as the Pt mesh aperture used as the current collector, it is therefore surmised that the connection of Pt to the LNO surface catalysed a reaction or acted as a nucleation point for water damage when H_2O is introduced into the atmosphere.

Chapter 8 – Conclusions and Further Work

The aim of this study was to investigate the chemical compatibility and electrochemical performance of the electrolyte material $La_{0.8}Sr_{0.2}Ga_{0.8}Mg_{0.2}O_{3-\delta}$ (LSGM) with the electrode material $La_2NiO_{4+\delta}$ (LNO), with a broad aim of addressing this combination as a solid oxide electrolysis cell as well as a solid oxide fuel cell due to the apparent lack of literature in this area.

The materials LSGM and LNO studied in this thesis were commercially acquired from Praxair Speciality Ceramics and CerPoTech respectively. Phase purity of the powders was confirmed by X-ray diffraction although conclusive determination of LNO structure was not possible with this technique. Much literature has focused on the structure of LNO using neutron diffraction and found it to be orthorhombic Fmmm or Bmab at low temperatures transforming to tetragonal I4/mmm or F4/mmm at high temperatures with a complex mix of phases at intermediate temperatures. However it has been found that the structure of LNO is dependant not only on temperature but on the stoichiometry, δ, and local oxygen partial pressure. For this reason a robust study of the structure of LNO in operating temperatures and partial pressures is suggested.

To ensure optimum electrode microstructure, a study of the effect of ball milling time on the LNO powder was conducted. In the literature a typical ball milling time of 24 hours is often stated for LNO and other electrode materials. For the material used in this study it was shown that the acquired commercial powder displayed the smallest particle size and particle size distribution with zero hours of ball milling, all ball milling times subsequently caused agglomeration of the powder. The material, production method and initial particle size distribution will affect the required ball milling time and so such a study should be conducted on all new powders used as electrode material.

Chemical stability between electrolysis and fuel cell constituents is paramount. It has been shown in literature that LNO reacts with common electrolyte materials CGO and YSZ, forming insulating layers at the electrode/electrolyte interface. It has also been suggested that LNO does not react with electrolyte material LSGM in ambient air. This thesis intended to test the stability of these two materials in operating conditions by subjecting a mixture of

the materials to in-situ X-ray diffraction over a range of operating temperatures, pO_2 and pH_2O. It was shown that in temperatures up to 800^oC, pO_2 down to 0.1atm. and pH_2O up to 0.2atm., no secondary phases are detected by XRD. To complete this study the mixture should also be analysed with in-situ XRD in increased pO_2. It is also suggested that in-situ XRD be conducted with increased time in order to determine whether there is degradation of the materials over extended operational periods.

In order to determine the electrochemical performance of LSGM and LNO as compatible electrolyte and electrode materials in a solid oxide cell, LNO was made into an ink and screen printed onto a dense LSGM electrolyte pellet. SEM analysis showed good adhesion of the LNO material on the LSGM. Porosity and microstructure of the LNO was shown to be satisfactory whereas the LSGM displayed some closed porosity that should ideally be reduced. A study of electrolyte preparation should be undertaken in order to optimise LSGM pellet density.

LSGM/LNO system was tested using electrochemical impedance spectroscopy (EIS) in ambient air, a range of pO_2 and pH_2O atmospheres, and under potential bias up to 1000mV in both anodic and cathodic direction, in order to emulate electrolysis and fuel cell operation modes.

In all conditions LNO displayed four impedance responses attributed to oxygen transfer between the electrode/electrolyte interface, charge transfer, mass transport, and oxygen adsorption phenomena. A fault in the analysis technique is the inability to separate responses that have too similar relaxation frequencies. It is recommended that all future impedance data of LNO be reviewed with the distribution of relaxation times (DRT) analysis technique in order to deconvolute the different responses further. With more accurate values for each response it would be possible to determine the change of capacitance and resistance with changing temperature, oxygen partial pressure and bias which can give further evidence as to the process behind each response. A change in activation energy of the LNO material is also seen at approximately 650^oC which is attributed to the change of dominant process to electronic conductivity at high temperature.

With zero bias LNO was shown to respond to changes in atmospheric conditions; across the temperature range 450 – 800^oC, an increase in pO_2 reduces the ASR of the LNO electrode

thought to be the result of improved mass transfer with increasing pO_2. The change in activation energy is also less pronounced in increased pO_2. The addition of 3% H_2O to the atmosphere appears to increase LNO ASR but reduces the change in activation energy, possibly by aiding electronic conductivity. It is theorised that the presence of water may aid surface exchange or may even be incorporated into the structure. Subsequent SEM images of the LNO surface after impedance in humid atmosphere show a degradation pattern thought to be due to the Pt mesh current collector catalysing a degenerative reaction or providing nucleation points for reaction of LNO with H_2O. As mentioned above, in-situ XRD in humid atmosphere up to 20% H_2O showed no reaction phases up to 800^oC however there are noticeable experimental characteristics not accounted for in the XRD setup, for example the XRD is performed on powders on a gold substrate whereas impedance is performed on a solid oxide cell with Pt mesh current collector. Further work would include expansion on the work carried out by Woolley et al. [95] in which an X-ray technique is employed during electrical polarization.

In this study the LSGM/LNO system was tested further by applying anodic and cathodic bias to the cell during EIS, which necessitated the use of a third reference electrode. The electrolyte was seen to be stable in all atmospheres with an applied bias except for in low pO_2 when an applied bias of negative (cathodic) 1000mV decreased conductivity at high temperatures. This is attributed to the act of bias introducing greater 'noise' and instrumental artefacts into the data, reducing the confidence with which we can rely on such data.

In high pO_2 and ambient air LNO responds well to applied bias, reducing ASR across the temperature range. For ambient air it is the magnitude of bias which improves LNO performance whereas in high pO_2 negative potential bias is shown to have a greater impact on the reduction of ASR values compared to positive bias. In low pO_2 atmosphere the application of positive and negative bias improves ASR at temperatures below approximately 600^oC, however above this temperature the application of negative bias greatly increases ASR, and this is also observed in the impedance data by the increase of the electrode response associated with mass transport/charge transfer. It is theorised that the application of bias increases the number of electrons supplied to the cell and thereby increases reaction rate shown as a decrease in ASR. However in low pO_2 the increase in

applied electrons outruns the number of oxygen molecules available for reaction. Under negative bias electrons are being supplied to the working electrode and so an increase in resistance is seen as an increase in the mass transfer response, however in positive bias the electrons are supplied to the counter electrode reducing the mass transport/charge transfer response from the working electrode and so ASR continues to decrease with temperature.

With and without bias low frequency inductance responses were seen on many of the impedance plots. This phenomena has been noted in literature and often attributed to adsorption/desorption of oxygen species and electrochemical reactions on the electrode surface however there seems to be a lack of experimental evidence to verify this. The application of bias in this study increased low frequency inductance, particularly for positive bias. Applied bias also increased the noise to signal ratio and 'loops' between impedance arcs were displayed, this highlights shortcomings with the impedance technique which must be understood in order to have full confidence in the results presented in this thesis.

LNO is a promising material for electrode use in solid oxide electrolysis or fuel cell use and has been shown in this thesis to be a stable electrode with LSGM electrolyte in a range of temperatures and atmospheres. However it is suggested that LNO is not suitable for electrolysis cathode use as the addition of water in the atmosphere causes degradation of the electrode surface. Whether Pt catalyses this effect or if mechanical degradation would occur with any current collector material would be the source of another study. The application of positive and negative bias improves electrode performance in all but negative bias in low pO_2 atmosphere implying that this material is suitable for solid oxide fuel cell cathode use and for solid oxide electrolysis anode use. In order to overcome the poor electronic conductivity, a similar study and the suggestions of further work mentioned in this chapter should be applied to higher order Ruddlesden-Popper materials which may display the benefits of the LNO material with increased electronic performance.

References

1. DECC, *The Carbon Plan: Delivering our low carbon future*. (2011).
2. Srinivasan, S. *Fuel Cells: From Fundamentals to Applications*. (2006), Springer Science+Business Media: USA.
3. Hoogers, G. *Fuel Cell Technology Handbook*. (2002), USA: CRC Press: USA.
4. Larminie, J. and Dicks, A. *Fuel Cell Systems Explained*. (2003), Wiley.
5. Abbas, H.F. and Daud, W.M.A.W. *International Journal of Hydrogen Energy*, (2010). **35**(3): p. 1160-1190.
6. USDoE. *Natural Gas Reforming*, (2011).
7. Ghirardi, M.L., *Indian Journal of Biochemistry & Biophysics*, 2006. **43**(4): p. 201-210.
8. Holladay, J.D., et al., *Catalysis Today.* (2009). **139**(4): p. 244–260.
9. Wachsman, E.D. and K.T. Lee*. Science*, (2011). **334**(6058): p. 935-939.
10. Agency, I.E., *Hydrogen Production and Storage*. (1996).
11. Yu, B., et al. *Science in China Series B-Chemistry*, (2008). **51**(4): p. 289-304.
12. Athanassiou, C., et al., *International Journal of Hydrogen Energy*, (2007). **32**(1): p. 38-54.
13. Chung Chieh. n.d. *CyberspaceChemistry*. [Online]. Available from: http://www.science.uwaterloo.ca/~cchieh/cact/c123/nernsteq.html. [Accessed 13 September 2013]
14. Stuart, P. *The Synthesis and Evaluation of Proton Conducting Electrolytes for High Temperature Steam Electrolysers*, PhD thesis. (2010), Imperial college London. p. 194.
15. Shaaban, A.H. *Pulsed DC and Anode Depolarization in Water Electrolysis for Hydrogen Generation*, H.a.f.c.e.s. agency, Editor. (1994).
16. Kothari, R., D. Buddhi, and R.L. Sawhney. *International Journal of Hydrogen Energy*, (2006). **31**(15): p. 2329-2336.
17. Yildiz, B. and M.S. Kazimi. *International Journal of Hydrogen Energy*, (2006). **31**(1): p. 77-92.
18. Jacobson, A.J. *Chemistry of Materials review*. (2010). **22**(3): p. 660-674.
19. Gellings, P.J. and H.J. Bouwmeester, *Handbook of Solid State Electrochemistry*. (1997): CRC Press.
20. Wang, W.S., et al. *Journal of the Electrochemical Society.* (2006). **153**(11): p. A2066-A2070.
21. Sayers, R., *Electrochemical Performance and Transport Properties of La2NiO4+δ*. PhD thesis. (2010), Imperial College London.
22. Jacobson, A.J. *Chemistry of Materials review*. (2010). **22**(3): p. 660-674.
23. Brett, D.J.L., et al. *Chemical Society Reviews* (2008). **37**(8): p. 1568-1578.
24. Skinner, S.K., J. *Materials Today*. **6**(3): p. 30–37.
25. W. E, L. and R. W. Mark, Editors *Ceramic microstructures: property control by processing*. (1994): Chapman & hall.
26. Irvine, J.T.S., et al. *Faraday Discussions*, (2006). **134**, 41–49
27. Lashtabeg, A. and S.J. Skinner. *Journal of Materials Chemistry*, (2006). **16**(31): p. 3161-3170.
28. Zhu, B. *International Journal of Energy Research*, 2009. **33**(13): p. 1126–1137.
29. Yokokawa, H., et al*. Fuel Cells*, 2001. **1**(2): p. 117–131.
30. Steele, B.C.H. and A. Heinzel. *Nature*. (2001). **414**(6861): p. 345-352.
31. Oncel, C. and M.A. Gulgun. *Developments in Solid Oxide Fuel Cells and Lithium Ion Batteries*, (2005). **161**: p. 61-68.
32. Kim, G., J.M. Vohs, and R.J. Gorte. *Journal of Materials Chemistry*, (2008). **18**(20): p. 2386-2390.
33. Jung, G.B., T.J. Huang, and C.L. Chang*. Journal of Solid State Electrochemistry*, (2002). **6**(4): p/ 225-230.
34. Perez-Coll, D., et al*. Electrochimica Acta*, (2003). **48**(11): p. 1551–1557.
35. Tsoga, A., et al. *Acta Materialia*, (2000). **48**(18-19): p. 4709-4714.
36. Goodenough, J.B. *Annual Review of Materials Research*, (2003). **33**: p. 91-128.
37. Philippeau, B., et al*. Solid State Ionics*, (2013). **249**: p. 17-25.

38. Laguna-Bercero, M.A., R.D. Bayliss, and S.J. Skinner. *Solid State Ionics*, In Press, corrected Proof.
39. Yu, B., et al. *Science in China Series B-Chemistry*, (2008). **51**(4): p. 289-304
40. Ni, M., M.K.H. Leung, and D.Y.C. Leung. *International Journal of Hydrogen Energy*, (2008). **33**(9): p. 2337-2354.
41. Marina, O.A., et al. *Journal of the Electrochemical Society*, (2007). **154**(5): p. B452-B459.
42. Kuharuangrong, S. *Ceramics International*, (2004). **30**(2): p. 273-277.
43. Boehm, E., et al. *Solid State Sciences*, (2003). **5**(7): p. 973-981.
44. Laguna-Bercero, M.A., J.A. Kilner, and S.J. Skinner. *Chemistry of Materials*, (2010). **22**(3): p. 1134-1141.
45. Zhao, H., L.H. Huo, and S. Gao. *Journal of Power Sources*, (2004). **125**(2): p. 149-154.
46. Hart, N.T., et al. *Journal of Materials Science*, (2001). **36**(5): p. 1077-1085.
47. Laguna-Bercero, M.A., S.J. Skinner, and J.A. *Journal of Power Sources*, (2009). **192**(1): p. 126-131.
48. Kao, C.F. and C.L. Jeng. *Ceramics International*, (2000). **26**(3): p. 237-243.
49. Rieu, M., et al. *Journal of the Electrochemical Society*, (2010). **157**(4): p. B477-B480.
50. Ferkhi, M., et al. *Electrochimica Acta*, 2012. **75**: p. 80-87.
51. Sayers, R., et al. *Solid State Ionics*, (2011). **192**(1): p. 531-534.
52. Torres-Garibay, C., D. Kovar, and A. Manthiram. *Journal of Power Sources*, (2009). **187**(2): p. 480-486.
53. Mogensen, M., et al. *The Electrochemical Society.* (2008). **6**(13)
54. Jiang, S.P. *Solid State Ionics*,(2002). **146**(1-2): p. 1-22.
55. Huang, D.P., et al. *Materials Letters*, (2006). **60**(15): p. 1892-1895.
56. Shaula, A.L., et al. *Solid State Ionics*, (2009). **180**(11-13): p. 812-816.
57. Yaremchenko, A.A., et al. *Journal of Materials Chemistry*, (2003). **13**(5): p. 1136-1144.
58. Munnings, C.N., et al. *Solid State Ionics*, (2005). **176**(23-24): p. 1895-1901.
59. Aguadero, A., et al. *Journal of Materials Chemistry*, (2006). **16**(33): p. 3402-3408.
60. Burriel, M., et al. *Energy Environ. Sci*, (2014). **7**(1): p. 311-316.
61. Aguadero, A., et al. *Journal of Fuel Cell Science and Technology*, (2007). **4**(3): p. 294-298.
62. Amow, G., I.J. Davidson, and S.J. Skinner. *Solid State Ionics*, (2006). **177**(13-14): p. 1205-1210.
63. Aguadero, A., et al. *Journal of Power Sources*, (2005). **151**: p. 52-56.
64. Perez-Coll, D., et al. *Journal of Power Sources*, (2008). **178**(1): p. 151-162.
65. Sayers, R., et al. *Fuel Cells*, (2008). **8**(5): p. 338-343.
66. Laberty, C., et al. *Electrochemical and Solid State Letters*, (2007). **10**(10): p. B170-B174.
67. Huang, K., J. Wan, and J.B. Goodenough. *Journal of Materials Science*, (2001). **36**(5): p. 1093-1098.
68. Ralph, J.M., A.C. Schoeler, and M. Krumpelt. *Journal of Materials Science*, (2001). **36**(5): p. 1161-1172.
69. Steele, B.C.H. *Journal of Materials Science*, (2001). **36**(5): p. 1053-1068.
70. Aguadero, A., et al. *Journal of Materials Science*, (2012). **47**(9): p. 3925-3948.
71. Rodriguezcarvajal, J. *Physica B,* 1993. **192**(1-2).
72. Irvine, J.T. *St Andrews presentation: Impedance Spectroscopy*. *St Andrews EIS*. 2010. St Andrews.
73. J. T. S. Irvine, D.C.S., and A. R. West. *Advanced Materials* (1990). **2**(3): p. 132-138.
74. Zhao, K., et al. *Ionics.* (2012). **18**(1-2): p 75.
75. Barsoukov, E. and R.M. J, *Impedance Spectroscopy (Second Edition)*. 2005: John Wiley & Sons, Inc.
76. West, A.R., *Solid State Chemistry and its Applications*. John Wiley & Sons Ltd.
77. Offer, G.J., et al. *Electrochimica Acta*, (2008). **53**(26): p. 7614-7621.
78. Rutman, J. and I. Riess. *Electrochimica Acta*, (2007). **52**(20): p. 6073-6083.
79. Adler, S.B., et al. *Solid State Ionics*, (2000). **134**(1-2): p. 35-42.

80. Lerch, M., H. Boysen, and T. Hansen. *Journal of Physics and Chemistry of Solids*, (2001). **62**(3): p. 445-455.
81. Slater, P.R., et al. *Journal of Solid State Chemistry*, (1998). **139**(1): p. 135-143.
82. Jones, P.G., et al. *Acta Crystallographica Section B-Structural Science*, (1979). **35**(JUN): p. 1435-1437.
83. Skinner, S.J. *Solid State Sciences*, (2003). **5**(3): p. 419-426.
84. Jorgensen, J.D., et al. *Physical Review B*, (1989). **40**(4): p. 2187-2199.
85. Singh, A.K., et al. *Building and Environment*, (2002). **37**(4): p. 415-419.
86. Stuart, P. *The Synthesis and Evaluation of Proton Conducting Electrolytes for High Temperature Steam Electrolysers*, PhD thesis. (2010), Imperial college London. p. 194.
87. Jorgensen, M.J. and M. Mogensen. *Journal of the Electrochemical Society*, (2001). **148**(5): p. A433-A442.
88. Escudero, M.J., et al. *Journal of Electroanalytical Chemistry*, (2007). **611**(1-2): p. 107-116.
89. Al Daroukh, M., et al. *Solid State Ionics*, (2003). **158**(1-2): p. 141-150.
90. Chen, X.J., K.A. Khor, and S.H. Chan. *Solid State Ionics*, (2004). **167**(3-4): p. 379-387.
91. Liang, F., et al. *Electrochemical and Solid State Letters*, (2008). **11**(12): p. B213-B216.
92. Liu, Y., et al. *International Journal of Hydrogen Energy*, (2012). **37**(5): p. 4388-4393.
93. Chen, J., et al. *Journal of Power Sources*, (2008). **183**(2): p. 586-589.
94. Brandon, N.P., S. Skinner, and B.C.H. Steele. *Annual Review of Materials Research*, (2003). **33**: p. 183-213.
95. Woolley, R., M. Ryan, and S. Skinner. *Fuel Cells*, (2013). **13**(6): p. 1080-1087.